CIRCUITS AND SYSTEMS FOR LATERAL FLOW IMMUNOASSAY BIOSENSORS AT THE POINT-OF-CARE

Evdokia Pilavaki

A thesis submitted to

University College London for the degree of

DOCTOR OF PHILOSOPHY

Supervised by

Professor Andreas Demosthenous

Professor Rachel McKendry

Department of Electronic and Electrical Engineering

University College London

DECLARATION

I, Evdokia Pilavaki confirm that the work presented in this thesis is my own. Where information has been derived from other sources, I confirm that this has been indicated in the thesis.

ACKNOWLEDGEMENT

As this PhD journey comes to an end I would like to thank all the people that helped and supported me to make this thesis possible.

First, I would like express my deepest gratitude to my PhD supervisor Prof. Andreas Demosthenous who has provided me with the opportunity to pursue PhD studies here in UCL. His help, support and suggestions were extremely valuable during the course of this journey. Under his guidance, I have not only improved myself as an engineer but also as a researcher.

Next, I would like to thank my second supervisor Prof. Rachel McKendry who has provided me with valuable insight, help and support especially in the biological side of my research. Her positive and friendly attitude has made her a role model for me.

My special thanks goes to Mr Peter Langlois, who has generously offered me with valuable technical guidance in the field of electronics, but also helped in proof reading my papers and my thesis.

I would also like to thank all my colleagues in the office who make a nice friendly atmosphere; it was a great pleasure working with all of you. Special thanks to Vasileios Kitsos, Matthew Schormans, Wu Yu, Virgilio Valente, Dai Jiang, Eleanor Grey, Candice Kean, Claudio Parolo, Nicoletta Nicolaou and Mark Portnoi for all the fruitful discussions we had and your valuable help.

UCL has been a great place to pursue my PhD studies. The staff, the facilities, and the financial support they gave me through my UCL studentship made this a pleasant journey.

My final and ultimate gratitude goes to my family and my partner who believed, listened and supported me, even during the hardest times. Thank you.

ABSTRACT

Lateral Flow Immunoassays (LFIAs) are biosensors, which among others are used for the detection of infectious diseases. Due to their numerous advantages, they are particularly suitable for point of care testing, especially in developing countries where there is lack of medical healthcare centers and trained personnel. When the testing sample is positive, the LFIAs generate a color test line to indicate the presence of analyte. The intensity of the test line relates to the concentration of analyte. Even though the color test line can be visually observed for the accurate quantification of the results in LFIAs an external electronic reader is required. Existing readers are not fully optimized for point-of-care (POC) testing and therefore have significant limitations.

This thesis presents the development of three readout systems that quantify the results of LFIAs. The first system was implemented as a proof of concept of the proposed method, which is based on the scanning approach without using any moving components or any extra optical accessories. Instead, the test line and the area around it, are scanned using an array of photodiodes (1 × 128). The small size of the pixels gives the system sufficient spatial resolution, to avoid errors due to positioning displacement of the strip. The system was tested with influenza A nucleoprotein and the results demonstrate its quantification capabilities.

The second generation system is an optimized version of the proof of concept system. Optimization was performed in terms of matching the photodetectors wavelength with the maximum absorption wavelength of the gold nanoparticles presented in the tested LFIA. Ray trace simulations defined the optimum position of all the components in order to achieve uniform light distribution across the LFIA with the minimum number of light sources. An experimental model of the optical profile of the surface of LFIA was also generated for accurate simulations. Tests of the developed system with LFIAs showed its ability to quantify the results while having reduced power consumption and better limit of detection compared to the first system.

Finally, a third generation system was realized which demonstrated the capability of having a miniaturized reader. The photodetector of the previous systems was

replaced with a CMOS Image Sensor (CIS), specifically designed for this application. The pixel design was optimized for very low power consumption via biasing the transistors in subthreshold and by reusing the same amplifier for both photocurrent to voltage conversion and noise cancellation. With uniform light distribution at 525 nm and 76 frames/s the chip has 1.9 mV_{rms} total output referred noise and a total power consumption of 21 μW. In tests with lateral flow immunoassay, this system detected concentrations of influenza A nucleoprotein from 0.5 ng/mL to 200 ng/mL.

IMPACT STATEMENT

In developing countries and remote locations where medical health centres are limited and electricity is not always available, immediate diagnosis of infectious diseases is not possible. This results in the uncontrollable spread of diseases with high mortality rates and severe socioeconomic impact. LFIA biosensors can be used for the detection of infectious diseases in developing countries due to their numerous advantages. However, in order to quantify the results in these biosensors an external electronic reader is required. In this thesis, readers have been developed for the quantification of the results in LFIA adopting a new method and techniques, which provided them with the following attributes: low cost, low power, high robustness, high reproducibility and low positioning error. All these qualities make the proposed readers suitable for diagnosis at the point-of-care.

The readers together with LFIAs can provide an immediate solution to the problem of infectious diseases in developing countries. Quick diagnosis allows for early treatment and avoids the need for samples to be sent to a laboratory for diagnosis, with the corresponding delay and anxiety in the patient and possible spread of the disease. Consequently, the diagnosis, treatment and management of diseases can be performed in a more economical way. Whereas with the quantification of the results in the sample the appropriate medication can be prescribed and the patient's health can be monitored.

The realized method includes scanning of the area of interest without using any mechanical components or any optical accessories and can be used in other applications where compact robust systems are required. The adopted methodology, which included the optical characterization of the surface of LFIAs and ray trace simulations, demonstrated that optical systems can be optimized using this method and therefore can be used in future reader designs. In addition, the new compact circuit design of the CIS which consumes very low power and performs noise cancellation reusing the same amplifier can be employed in future CIS designs.

LIST OF CONTENTS

LIST OF FIGURES

LIST OF TABLES

ABBREVIATIONS

3T-APS	3-transistor active pixel sensor
4PL	Four parameter logistic
4T-APS	4-transistor active pixel sensor
ABS	Acrylonitrile Butadiene Styrene
ADC	Analog-to-digital converter
AMS	Austriamicrosystems
ASIC	Application specific integrated circuit
ASSURED	Affordable, Sensitive, Specific, User-friendly, Rapid and Robust, Equipment-free and Deliverable
AuNPs	Gold nanoparticles
BRDF	Bidirectional reflectance distribution function
BSDF	Bidirectional scattering distribution function
BTDF	Bidirectional transmittance distribution function
C. difficile	Clostridium difficile
CCD	Charge coupled device
CDS	Correlated double sampling
CIS	CMOS Image Sensor
CMOS	Complementary Metal-Oxide Semiconductor
CPLD	Complex programmable logic device
CTIA	Capacitive transimpedance amplifier
DAQ	Data acquisition
DDS	Delta difference sampling

DNA	Deoxyribonucleic acid
DSNU	Dark signal nonuniformity
ELISA	Enzyme-linked immunosorbent assay
FFs	Flip-Flops
FPN	Fixed pattern noise
HA	Hemagglutinin
IC	Integrated circuit
IgA	Immunoglobulin A
IgG	Immunoglobulin G
IgM	Immunoglobulin M
LEDs	Light emitting diodes
LFIAs	Lateral Flow Immunoassays
MOS	Metal-oxide semiconductor
MOSFETs	Metal-oxide-silicon field-effect transistors
NA	Neuraminidase
NEPs	Nuclear export proteins
NMOS	N-type metal-oxide semiconductor
PBS	Phosphate-buffered saline
PCB	Printed circuit board
PMOS	P-type metal-oxide semiconductor
POC	Point-of-care
PRNU	Photo response nonuniformity
QE	Quantum Efficiency
RNA	Ribonucleic acid
S-layer	Surface layer

SlpA	Surface-layer protein A
SNR	Signal-to-noise ratio
SSE	Error sum of square
SST	Total sum of square error
WHO	World Health Organization

1

INTRODUCTION

Infection is caused when microorganisms such as virus, bacteria, fungi, and parasites enter the host's tissue and reproduce [1]. These microorganisms can be transmitted via direct contact, body fluid transfer, contaminated food / water or animal and insects bites. Infectious diseases are caused when these microorganism produce damage to the host via colonization, steal of nutrient and produce toxins or other dangerous agents [2], [3], [4]. The likelihood of the host to obtain an infectious disease depends on different parameters such as age, vaccination history, pregnancy and previous infections. Treatment of infectious diseases usually includes the use of antimicrobial drugs. However, their use carry some risks for patients such as allergic reaction, toxicity and disturbance of the normal flora that could result in the microorganism to develop resistance to the drug [5].

Infectious diseases have caused death to an uncountable number of people throughout the years. Many times spreading from a single host to worldwide scale, contributing to the extinction of civilizations, and having major socioeconomic impact. In 430 BC the relocation of Greeks into Athens due to the war with Sparta initiated an epidemic that killed up to half of its population [6]. In 166 AD, Roman soldiers infected with plague, returned from war spreading the disease that killed around five million people across Europe [3]. In 1345 - 1347 the Black Death spread across Europe due to merchant ships killing 3 out of 10 Europeans with total 40 million deaths worldwide. In 1520 smallpox killed more than one quarter of the population of Aztec leading to their easy defeat against the Spanish [6]. These are some examples

showing the tremendous impact of infectious diseases across the globe during the human history.

1.1 DIAGNOSTIC SYSTEMS

The development of the microscope from Anton van Leeuwenhoek set the foundations for the understanding of infectious diseases. Later in 1878 Robert Koch showed the link between infectious diseases and microorganism, followed by several scientists that identified the origin of the different infectious diseases [6]. Treatments for various diseases and vaccines begun to develop leading in the increase of life expectancy and decrease in mortality rate due to infectious diseases.

The detection of infectious diseases usually has the following procedure. After the doctor examines the patient and concludes that it has an infection, body fluid samples are taken and sent for laboratory tests. The samples are usually blood, sputum, urine, stool, tissue or mucus. Then after hours or days depending on the microorganism and the detection method being used the results are available and the treatment can begin [7].

Different laboratory methods are used for different types of microorganism. Among the most common is the use of microscope either for direct observation of the sample or after using a staining method, like Gram's stain method which is used for the identification of bacterial. Based on the color result seen using a microscope, the presence or not of specific bacteria can be identified [5]. When culture of the sample is required the sample is deposited in a dish and using different nutrients the suspected microorganism is helped to grow and therefore it is easier to be detected [8]. Mass spectrometry is a method used for the identification of the spectrum of ionized molecules from the sample. The generated ions are directed onto a magnetic or electric field where they split up in order to be identified based on their mass to charge ratio (m/z) by the mass spectrometer [9]. Nucleic acid amplification method is used to identify the genetic material of specific microorganism that cannot be identified by any other method. The genetic material can be deoxyribonucleic acid DNA or ribonucleic acid (RNA) [7]. Immunologic tests are used for the detection of antibodies

or antigens in the sample, which indicates the presence of microorganism, such a system is the ELISA. All the above traditional lab-based methods are usually performed with diagnostic systems that are bulky, expensive, fragile and require fully trained personnel to operate them. Table 1.1 summarizes the time required for various diagnostic methods used in laboratory settings to identify different microorganisms [8].

Diagnostic Method	Microorganism identification
Microscopy	Minutes
Gram stain	Minutes
Culture	Days to weeks
Mass spectrometry	Minutes to hours
Nucleic acid	Hours
Immunologic	Hours to a day

Table 1.1. Diagnostic methods for the detections of microorganisms and their required time to produce results.

1.2 LIMITATIONS OF DIAGNOSTIC SYSTEMS

Even though significant advances have been made in the detection, treatment and prevention of infectious diseases, most of the time these inventions are unavailable or unsuitable for the population of low income countries. For example, in 2010 worldwide 15 million deaths were attributed to infectious diseases (including maternal and nutritional disorders), while in low income countries the same year infectious diseases were the leading cause of death [10]. The main factors contributing to such a high mortality rate especially in low income countries are the following:

a. Lack of medically trained personnel.
b. Limited number of medical centres which, most of the time, are not fully equipped.
c. Time consuming diagnostic methods and procedures.
d. Essential technology does not exist or when it exists is very expensive and not appropriately modified for low income countries [11].

As a result, most of the time the infectious diseases remain undiagnosed or diagnosed in late stages, where the effectiveness of the treatment is limited. Consequently, not only the carriers of the infections are in danger but also anyone in contact with them. Also, the modern means of transportation connecting people around the globe can contribute to uncontrollable spread of an infection from local to global scale with severe socio-economic impact. Still in 2016 some infectious diseases were between the top 10 causes of death globally as shown in Figure 1.1 (the data were collected from [12]), and even though significant advancements in medicine and technology are continuously emerging, the predictions for the future remain disappointing. According to the World Health Organization (WHO) by 2050, 13 million people are expected to die globally from infectious diseases [10]. Therefore, there is a major need for diagnostics systems that will identify and monitor infectious diseases at the POC and that will be appropriately designed and developed to accommodate the needs of low income countries.

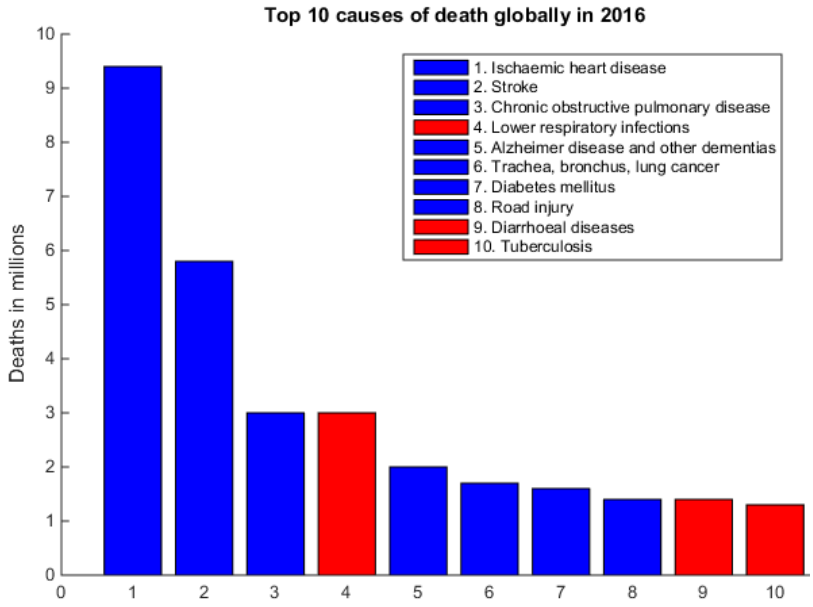

Figure 1.1 Ten top causes of death globally for the years 2016, (the data were collected from [12]). The red bars indicates the infectious diseases.

1.3 PROPOSED DIAGNOSTIC SYSTEMS

Portable POC biosensors are a useful alternative to laboratory-based diagnostic systems because they can provide quick diagnosis near the patient using small sample volume [13]. A biosensor is a device that detects the analyte (antigen, virus, toxin, DNA/RNA) of interest based on a selective binding event or a catalytic event and converts it into a measurable signal [14]. The biological sensing element (bioreceptor) existing in the biosensor can be antibody, enzyme, protein, microorganism etc. The outcome of the biological response is a measurable signal such as optical, electrochemical, and physical that is measured and transformed into electrical signal using a reader. The first part of the reader is a sensing element such as an electrode, photodetector and thermistor. The resulting measurable signal is then processed by the electronic circuit system in the reader and the result is displayed as quantitative or semiquantitative information of the concentration of the analyte of interest [15], [16]. Figure 1.2 shows the principle of operation of the biosensor and reader device.

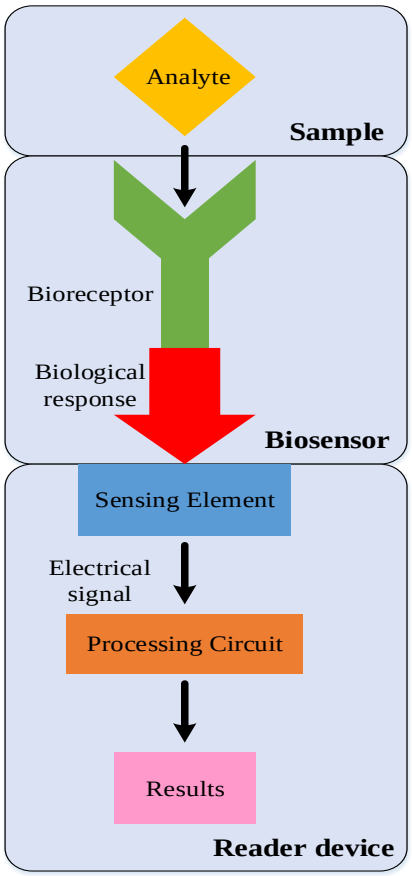

Figure 1.2 Diagram of a diagnostic system based on the use of biosensor and reader device.

This thesis proposes the development of an optical reader device that interfaces with LFIA biosensors for the quantification of analyte in the sample. Even though significant advancements have been made in the biosensor side of operation, the readers which have been developed for optical biosensors, are most of the time not tailored to the requirements of a POC diagnostic system. Therefore, they have one or more of the following drawbacks: high cost, high power consumption, low robustness, low reproducibility and susceptibility to positioning errors.

All the aforementioned issues are addressed in this thesis by developing a reader that is based on the scanning method without using any moving parts and by utilizing as sensing element an array of photodiodes that has appropriate size to match the biological response of the biosensor. The acquired signals are processed using the electronic circuit built in the device and the quantification of the analyte is performed.

The first generation system was developed using discrete components and was used as a proof of concept, to demonstrate the advantages of the proposed method. Based on the promising results that the system showed when interfaced with biosensors, a new optimized system was developed. The objective of the second generation system was to improve the performance of the proof of concept system by optimizing it, while still using the same scanning method. The optimization performed by first characterizing the surface of the biosensor in terms of light distribution and then modelling and simulating all the critical components of the reader in a ray trace simulation program (OpticStudio software, Zemax LLC). The aim was to define the optimum position of the components in order to increase sensitivity in terms of limit of detection and variation of the results and reduce the power consumption. Based on the simulation results a system was developed using discrete components. The system was tested with biosensors with two different types of analyte to show the versatility of the reader. In addition, the results demonstrated improvement in limit of detection and power consumption compared to the first generation system.

Further to the above systems, an application specific integrated circuit (ASIC) CIS was designed fabricated and tested using on Austriamicrosystems (AMS) 0.35 μm complementary metal-oxide semiconductor (CMOS) technology. The purpose was to further miniaturize the reader by replacing the discrete component array of photodiodes with the developed chip. The design is based on a new compact pixel

architecture that has very low power consumption and low noise. Tests of the chip with biosensors showed its quantification capabilities. This work addresses the need of a reader for LFIA biosensors that will be used at the POC in a holistic approach, while at the same time it tackles the performance issues of other readers. The development of an ASIC CIS specifically designed for this application is performed for the first time and can be used as the basis for future CIS designs.

1.4 ORIGINAL CONTRIBUTIONS

The work reported in this thesis has provided the following contributions in the field of readers for LFIA biosensors:

1. Investigation of the required properties that a system for LFIA biosensors should acquire in order to be considered suitable for POC diagnostics.
2. Introduction of a new method for quantifying the results in LFIAs, which is realized by scanning the test line and some area around it without using any moving parts and any optical accessories making the system robust and easy to carry around in the field.
3. Examination of the optical performance of the proposed system using ray trace simulations, in order to define the optimum setup. The results can be used as a benchmark for future systems implemented using the same method.
4. Novel circuit designs for the ASIC implementation of CMOS image sensor that enable photocurrent to voltage integration and noise cancellation reusing the same amplifier and therefore reducing the power consumption.
5. Design, implementation and test of a CMOS image sensor for LFIA readout systems. According to the author's best knowledge, this is the first ever reported CIS specifically designed for this application.

This project was associated with the EPSRC Interdisciplinary Research Centre in Early Warning Sensing Systems for Infectious Diseases (i-sense), which aims in the development of diagnostic systems for the detection of infectious diseases at the point of care. The main disease under investigation in this project are: influenza, HIV and bacterial infection.

1.5 AUTHOR'S PUBLICATIONS AND AWARDS

The work presented in this thesis has led to the following publications and awards:

JOURNALS

E. Pilavaki, V. Valente, A. Demosthenous, **CMOS Image Sensor for Lateral Flow Immunoassay Readers**, *IEEE Transaction on Circuit and Systems II: Express Briefs*, 2018, doi: *10.1109/TCSII.2018.2855054.*

E. Pilavaki, A. Demosthenous, **Optimized Lateral Flow Immunoassay Reader for the Detection of Infectious Diseases in Developing Countries**, *Sensors Journal*, Nov. 2017, doi: *10.3390/s17112673*.

CONFERENCES

E. Pilavaki, V. Valente, W. Serdijn, A. Demosthenous, **Compact Pixel Architecture for CMOS Lateral Flow Immunoassay Readout Systems, IEEE** *Conference on Ph.D. Research in Microelectronics and Electronics (PRIME)*, 2017.

E. Pilavaki, C. Parolo, R. McKendry, A. Demosthenous, **Wireless Paper-Based Biosensor Reader for the Detection of Infectious Diseases at the Point of Care**, *IEEE Sensors Conference*, 2016.

E. Pilavaki, C. Parolo, R. McKendry, A. Demosthenous, **Wireless Optical Sensing Device for the Detection of Infectious Diseases at the Point of Care**, *Proceedings of the IEEE Engineering in Medicine and Biology Society (EMBC)*, 2015.

AWARD

UCL Electronic and Electrical Engineering Research Student Cisco prize, 2016.

1.6 THESIS OVERVIEW

This thesis is organized in six chapters.

Chapter 1 provides a brief introduction to infectious diseases and how important their monitoring and detection is, using biosensors that interface with POC readers. A summary of contributions that this work archived in relation to systems for LFIAs biosensors is presented.

Chapter 2 provides an introduction to the biological aspect of influenza virus and the importance to acquire diagnostic systems for the detection of influenza at the POC. The chapter explains the chemical structure of LFIA and its operation. An overview of the major methods used in reader systems is covered, as well as a literature review of existing readers with emphasis on the important characteristics required for POC diagnostic devices. The chapter concludes by identifying the gap in the readers market; a gap that was intended to be fulfilled with the work presented in this thesis.

Chapter 3 reports the development of the first generation proof of concept reader for the quantification of analyte in LFIAs based on the proposed method. The test results demonstrate the suitability of this system as POC reader. The chapter continues with the description of the second generation optimized system, which consists of the optimized version of the first generation system. The optimization method is performed by modeling the optical performance of each critical component of the system and by defining the best position of these components in order to achieve uniform light distribution across the LFIA and minimum power consumption. The model of LFIA is based on experimental results from Imaging Sphere. Using discrete

components, the simulated model was realized and tested with LFIAs in various concentrations of Influenza A nucleoprotein and in Surface-layer protein A.

Chapter 4 describes the design and implementation of a CIS, using 0.35 μm CMOS technology. The CIS has 4 x 64 pixels and is designed specifically to be used in readers for LFIAs. A new compact pixels architecture is proposed which reduces the power consumption by using only one amplifier for both current to voltage conversion and noise cancellation operations. In addition, the circuits for current biasing and pixel addressing of the CIS are presented.

Chapter 5 presents experimental tests of the fabricated CIS for the characterization of its electrical performance. Further experimental tests are performed in a reader setup, to demonstrate the capability of the CIS to quantify the concentration of analyte in LFIAs.

Chapter 6 provides an overview of the work presented in this thesis and summarises important results demonstrating the contribution of the work presented. Possible future research directions for the enhancement of the systems are also being discussed.

2

FUNDAMENTALS OF LATERAL FLOW IMMUNOASSAYS

Infectious diseases like influenza affect a great portion of the global population every year and can cause fatal results especially to those who receive late diagnosis and treatment. This is mainly the case for the population of the developing countries. Therefore, diagnostics that can detect infectious diseases at the POC are of utmost importance. Due to their numerous advantages, lateral flow immunoassays are ideal biosensors for POC diagnosis. However, in order to quantify their results an external electronic device needs to interface with them. Numerous devices have been proposed for this purpose using different methods.

This chapter introduces the influenza virus as well as providing a summary of the available diagnostic methods for influenza. It describes the operation of lateral flow immunoassays and provides a review of the most common methods for quantifying the concentration in lateral flow immunoassays. Furthermore, it presents an analysis and comparison between important characteristics of the available systems. Finally, this chapter identifies and discusses the existing gap in the readers market in order to highlight the importance and necessity of this research work.

2.1 INFLUENZA

Influenza viruses are usually responsible for many respiratory infections in humans and often cause seasonal epidemics or occasionally pandemics [17]. The main means of transmission of influenza virus is through the air, where infected droplets enter the mucosae and replicate. The most common clinical symptoms of influenza infection in humans such as temperature increase, headache, dry cough and fatigue appear a few days after the virus enters the human body. Consequently, the carriers can transmit the infection onward without being aware that they are infected. [18]. Children and old people infected with influenza virus are more susceptible to complications that can lead to fatal outcomes.

Historically, influenza has been reported since ancient times, killing millions of people worldwide. Among the different influenza viruses only influenza A leads to pandemics and is capable of infecting humans and other warm-blooded animals such as birds and pigs. Influenza B viruses can only infect humans and seals and influenza C can only infect humans and pigs [19]. From 1889 until today five pandemics were caused by influenza virus, as shown in Figure 2.1. In Russia in 1889 an influenza pandemic was documented which spread in waves globally. It is believed that it was H2 or H3 subtype of influenza A. Later in 1918 the worst ever documented influenza pandemic, known as Spanish flu of H1N1 subtype occurred, killing globally around 50 million of people. In contrast to other pandemics, the age group that was affected the most was between the ages of 20 to 40 years, which is unusual for influenza infection. The virus continued to circulate as seasonal flu until 1957 when it was replaced by another pandemic strain (Asian flu) which began in Hong Kong and China, and then spread worldwide. The virus was identified as a new H2N2 subtype. Deaths were recorded mainly in children and elderly people as expected (since they are the most vulnerable group). Later, in 1968 a pandemic outbreak of H3N2 subtype started from Hong Kong and spread worldwide. In 2009, the H1N1 subtype re-emerged in Mexico and spread globally with moderate severity [20]. This virus started from the swine. The regularity of all these pandemics, the constant change of virus subtype and the fact that less than 10 years ago there was an influenza pandemic shows us how vulnerable and unprepared we are for such outbreaks.

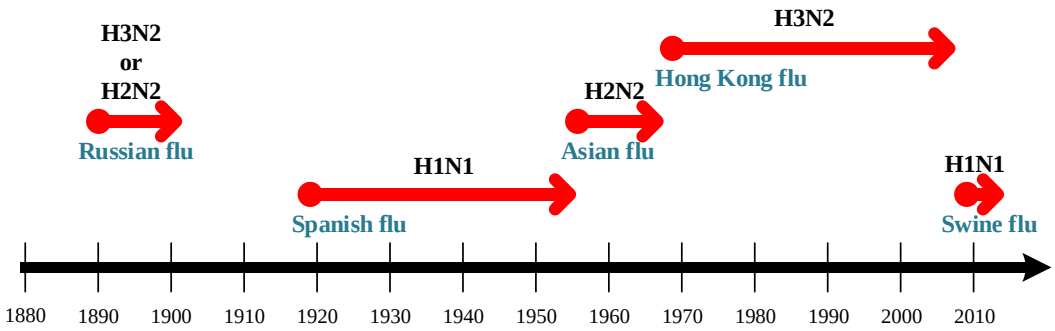

Figure 2.1 Timeline of Influenza pandemics since 1889.

Influenza virus is part of the *Orthomyxoviridae* family, which comprises enveloped viruses with a genome of segmented negative-stranded RNA [20]. Influenza virion (virus particle) broadly consists of the envelope and the core [21]. Influenza A virions are spherical shape with dimensions around 100 nm, or pleomorphic. The envelope consists of a lipid bilayer with glycoproteins HA (hemagglutinin) and NA (neuraminidase). It has also M2 (ion channel) and M1 (matrix protein). HA and NA look like spikes in the lipid membrane. Influenza A has 18 HA and 11 NA so far discovered which in combination can generate the different subtype of Influenza [18]. For example, influenza A subtype H3N2 has type 3 hemagglutinin (H) protein and type 2 neuraminidase (N) protein. Antibodies generated from the immune response of the host target these spikes to neutralize the virus. HA is responsible for the connection of the virion to the host cells and subsequently the penetration and infection of the cell. NA is responsible for the spread of virus to other cells. M1 protein is below the lipid bilayer generating a bridge between the core and the envelope. Inside the core there are 8 segments of RNA (influenza B has also 8 segments of RNA, and influenza C has 7 segments of RNA) linked with proteins PB1, PB2, PA and NP. Also in the core of the virion there are the nuclear export proteins (NEPs) [21].

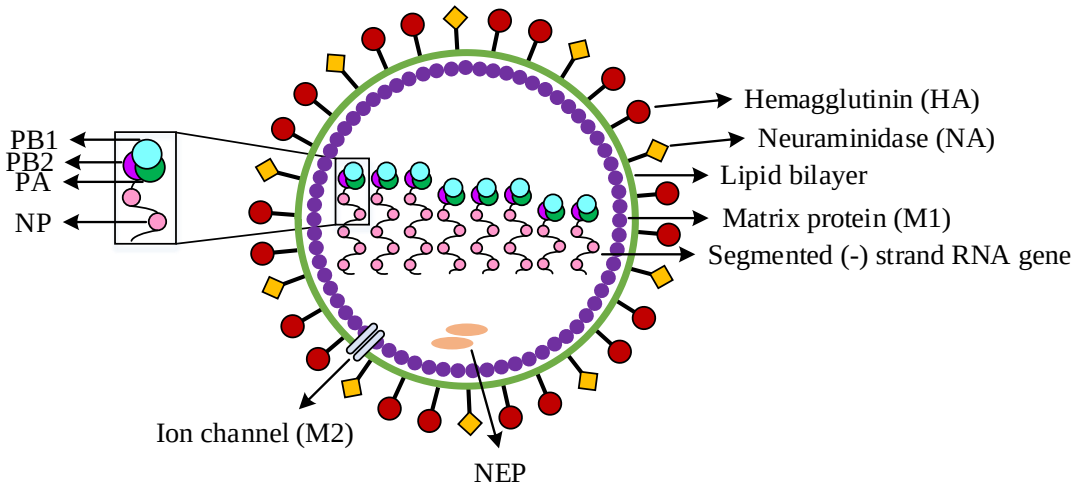

Figure 2.2 Structure of influenza virus.

When the host is infected with influenza virus it triggers a complex process of cellular and chemical responses aiming the neutralization of the virus. Among the main actions induced is the generation of antibodies, immunoglobulin A (IgA), immunoglobulin M (IgM) and immunoglobulin G (IgG). Mucosal IgA antibodies are produced immediately after the infection from mucosal epithelial cells. They constitute the first line of immune-defence against the viruses of the upper respiratory track. IgG antibodies transude to mucus of the lower respiratory track providing protection. IgM antibodies are produced soon after the infection and are used for the neutralization of the virus and their presence is a characteristic of recent virus infection [22].

Particularly important are the antibodies specific to HA and NA glycoproteins. The HA specific antibodies bind to the HA of the virion and in this way obstructing the connection of the HA to the receptors of epithelia cell. The NA specific antibodies connect with the NA glycoprotein blocking the spread of the infection.

Even though vaccination is used to stimulate the generation of antibodies specific to seasonal influenza viruses, immunity will be achieved only for a narrow range of subtypes. [23]. This is because influenza virus has high mutational rate and therefore antibodies of a specific subtype influenza virus cannot effectively bind to all subtypes [20].

2.1.1 DIAGNOSTIC METHODS FOR THE DETECTION OF INFLUENZA

When a patient has clinical symptoms similar to influenza, a sample should be collected and examined using one of the available methods. The majority of the detection methods are laboratory based and require sample from the nose or pharynx, which need to be tested within a certain amount of time after collection.

The viral culture diagnostic method is considered the traditional gold standard method and can be performed only in specialized laboratories. It involves the inoculation of mammalian cells with the tested sample and monitoring of cells over the course of many days. The culture is finally tested by adding antibody staining, as shown in Figure 2.3 (a). The viral culture process can be accelerated and provide results within 1-2 days if first the viral antigen is detected before the cytopathic effect. However this process is less sensitive than traditional viral culture [18].

The antigen detection method can be performed using a direct fluorescent assay or the enzyme-linked immunosorbent assay (ELISA). The direct fluorescent assay involves the staining of the sample cells with influenza specific antibodies coupled to fluorophores and examining their response using a fluorescent microscope [19], [24]. In the ELISA test an antibody that binds to the antigen of interest is immobilized in the well. If the sample contains the viral antigen it will bind with the antibody in the well, and this binding is detected via the help of enzyme called horseradish a second antibody labelled with a peroxidase, which generates a color signal measurable with a spectrophotometer [2]. This test requires more than a day to generate results. Figure 2.3 (b) illustrates the ELISA process. The rapid antigen detection method uses labelled antibodies with gold nanoparticles or fluorescence dyes that bind to the viral antigen of the sample and generate a color signal within minutes.

A nucleic acid amplification method involves the extraction and purification of the genetic material from the sample, the amplification by polymerase chain reaction (PCR) product which is coupled to fluorescent label. This method known as quantitative PCR has high sensitivity but it was confined to use in large laboratories. New rapid PCR methods have been introduced which combine together the amplification and detection stages and can reduce the detection time to around 5 hours [24]. Figure 2.3 (c) shows the nucleic acid amplification methods.

Serological methods are used to detect the presence of antibody in the sample, which can be a result of viral infection. Because antibodies can be found in samples for decades after a viral infection, diagnosis by serology requires two samples. One at start of the disease and one after 10 to 14 days. An increase in antibody level will verify the diseases. [18]. This method is mainly used for epidemiological studies. Figure 2.3 (d) demonstrates the serological test. Table 2.1 summarizes the main diagnostic methods for detecting influenza virus infection.

Method	Description	Comments
Viral culture	• Culture the sample in mammalian cells, look for cytopathic effect.	• It is considered as a gold standard [19]. • Specialized laboratories required, and results are available after approximately 10 days.
Antigen Detection using direct fluorescent assay tests	• Identify the presence of antigen	• Relatively good results if high concentrations of viral antigen are present in the sample. • Results available after 1-2 hours.
Rapid antigen detection using lateral flow tests	• Employ antibodies that target the viral antigen.	• Results available in 10 - 20 minutes. • Less sensitive than laboratory-based methods.
Nucleic acid amplification-based test	• Detection of genetic material (DNA/RNA) of virus [19].	• Results available in approximately 5 hours. • High sensitivity.
Serology	• Two serum samples are collected and compared (at the start of the disease and after 10 to 14 days). This is because antibodies may be present due to prior infection [18].	• Suitable for epidemiological studies (e.g. vaccination effectiveness). • Not ideal method for diagnostic purposes.

Table 2.1. Summary of main laboratory-based diagnostic methods for the detection of Influenza virus infection.

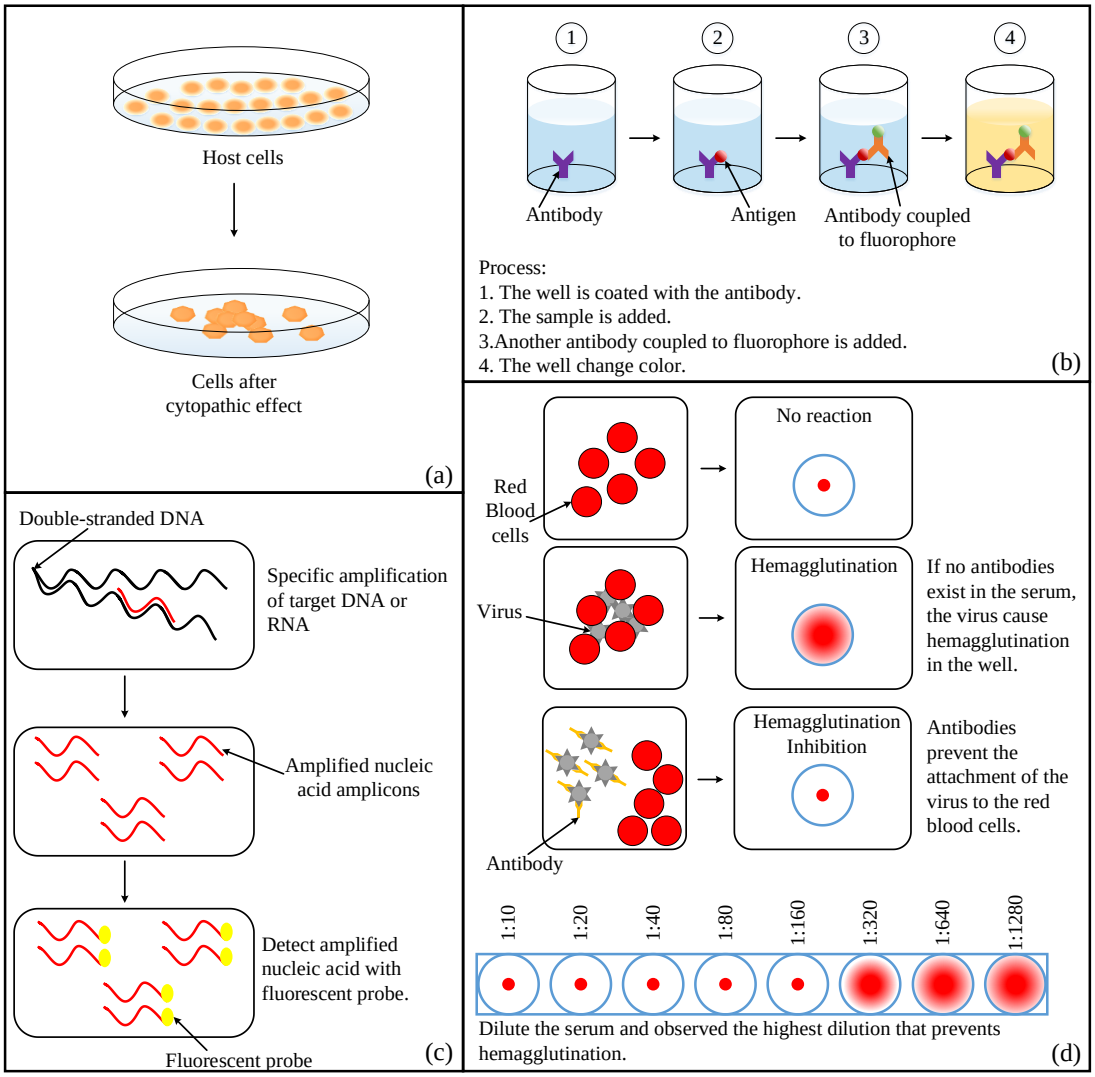

Figure 2.3 Schematic representation of different diagnostic methods (a) viral culture, (b) antigen detection in ELISA test, (c) nucleic acid amplification test, (d) serology test (redraw from [25]).

All the methods presented in Table 2.1 are widely used for diagnostic purposes in developed countries. However, for diagnosis at the POC and for patient management methods that produce results in the minimum possible time are preferred especially in developing countries. For that reason, the quickest method is considered the rapid antigen detection method, which is employed in many biosensors.

2.2 LATERAL FLOW IMMUNOASSAYS

POC diagnostic tests for the detection of infectious diseases are extremely important, especially for developing countries and isolated locations where conventional diagnostic systems are unsuitable or unavailable. According to the World Health Organization (WHO) diagnostic tests that are designed for use in developing countries should meet the ASSURED criteria: Affordable, Sensitive, Specific, User-friendly, Rapid and Robust, Equipment-free and Deliverable [26][27].

Many POC diagnostic tests are based on paper-based lateral flow assays and are used for the detection of either microbial particles or antibodies [28], [29]. The lateral flow assay (LFA) is a common type of paper-based biosensor that fulfils all the ASSURED criteria. Furthermore due to inherent advantages such as being lightweight, low cost, disposable, easily reproducible and requiring small sample volumes they are considered ideal for use in developing countries [30]. The most successful commercialized diagnostic of this type is the pregnancy tests [31].

LFAs are usually strip shaped prefabricated biosensors made of several pads of paper-like materials that overlap one another. When a fluid sample is applied at the end of the strip, it will flow due to capillary forces along its entire length activating the prestored lyophilised reagents. When antibodies are used as the identification element, the LFA is called lateral flow immunoassay (LFIA) [32], [33]. Various fluid samples can be tested using LFAs such as urine, sweat, saliva and nasal swab [34].

The POC diagnostics that are based on immunoassay methods are exploiting specific antibody-antigen interactions. When the host is infected with a virus antibodies are generated by the immune system which binds to viral antigens in order to neutralize them. In LFIAs during the fabrication process, antibodies are placed on the strip, which will react with antigen in the sample if it is infected. The sensitivity and specificity of an assay is defined by the type of antibody and its affinity (the strength of antibody-antigen binding) and avidity (stability of the binding) [35]. Antibodies are conventionally depicted as Y-shaped molecules. The epitope is part of the antigen that binds to antibody. The paratope is part of the antibody that binds to the antigen Figure 2.4 shows the specific antibody-antigen interaction of a viral analyte.

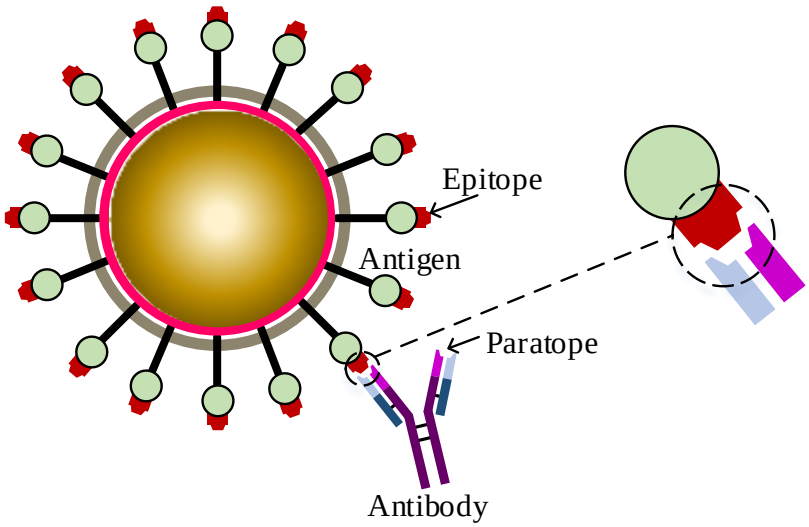

Figure 2.4 Antibody-Antigen binding interaction.

The LFIA consists of 4 pads: the sample pad, the conjugation pad, the detection pad and the absorbent pad, all mounted on a backing card, as shown in Figure 2.5(a). Initially the sample is added to the sample pad. This pad is made of cellulose and it has two main functions: 1) to sequester impurities in the sample and 2) to store dried assay agents ensuring the correct conditions for the test [31], [30]. Then the sample moves to the conjugate pad. This pad is made of glass fibers and it has immobilized conjugated labels [36]. The labels are made of particles usually gold nanoparticle or latex microparticles conjugated to specific antibodies. When the sample reaches the conjugation pad, the labels bind specifically to the analyte of interest generating an immune-complex, as shown in Figure 2.5(b). After, the immune-complex will flow to the detection pad [30]. This pad is made of nitrocellulose, where other antibodies specific to the analyte have been immobilized, in the shape of a line. If the analyte of interest is present in the immune-complex, it becomes "sandwiched" between the antibodies of the detection pad and the antibodies of the label, as illustrated schematically in Figure 2.5(c). The accumulation of the labels on the detection line generates a colored (test) line that is visible with naked eye [32]. The color intensity is proportional to the amount of analyte present in the sample. The unbound fraction of the sample continues to flow along the strip and binds to the antibodies in the control line, producing another colored (control) line. The control line antibodies bind specifically to the antibodies of the label, therefore the control line should be generated regardless of the test line results to verify the proper operation of the assay [27], [36],

as shown in Figure 2.5 (d). The rest of the sample is absorbed in the absorbent pad which is made of cellulose filters [37], [36]. The outcome of this process is usually quantitative or semi-quantitative and can be interpreted using the colorimetric method, which is realized by either visual inspection of the LFIA or by using a reader device [32]. Colorimetry is a method that is used to define the concentration of analyte by measuring the color intensity generated in the biosensor [38].

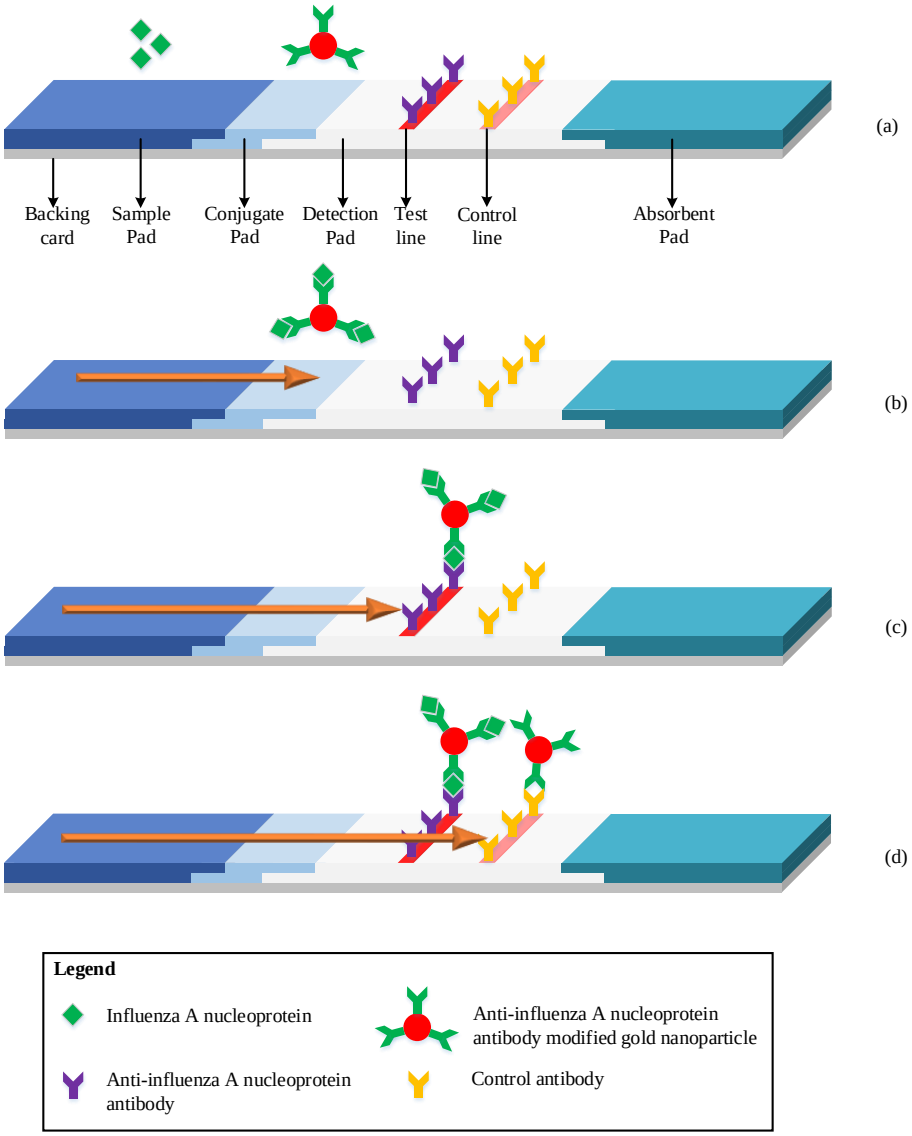

Figure 2.5 Schematic illustration of the operation of LFIA for the detection of Influenza A nucleoprotein (a) details of the different parts of the LFIA, (b) binding event in conjugation pad, (c) generation of test line, (d) generation of control line.

In high weight analytes with multiple antigenic sites, the sandwich format is used in the LFA platforms. This is the case for many viral infectious analytes. In this

format the main antibody is immobilized against the antigen in the test line, while a different antibody which binds to different epitope of the same antigen is conjugated to a nanoparticle [39]. In positive samples the sandwich is generated at the test line as described in the previous paragraph and shown in Figure 2.6.

In low weight analytes with single antigenic site, meaning that the analyte cannot bind with two antibodies simultaneously, the competitive format is used in the LFA platforms. Such an example is in the LFAs designed for the detection of the drug of abuse [40]. In this format the analyte block the antibody of the test line stopping the conjugated particle to bind with this antibody and thus generate a color test line [34]. The positive results is shown with the absence of the test line while the control line is always visible regardless of the result [36]. Figure 2.6 shows the two formats when the analyte of interest is present or not in the sample [41].

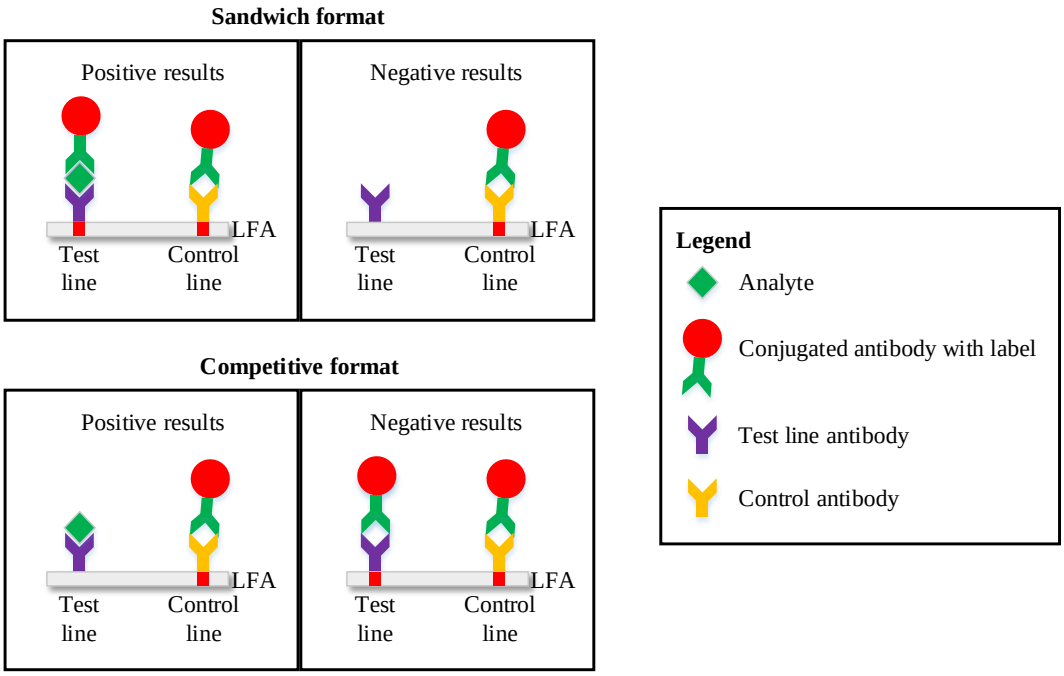

Figure 2.6 Schematic representation of the sandwich and competitive format in LFAs for positive and negative results.

2.2.1 GOLD NANOPARTICLES

There are many different types of labels used in LFAs but commonly used are the colloidal gold nanoparticles. This is because colloidal gold has numerous advantages

such as low cost, it is easy to use in the lab, it can be found in unconjugated forms and is very stable both in dry and liquid form. Furthermore colloidal gold can generate an intense color which is easily observed by the naked eye [36].

Gold nanoparticles (AuNPs) are widely used in colorimetric biosensors. This is due to a very important optical property called surface plasmon resonance (SPR). This property is evident when an external electromagnetic wave such as light interacts with the electrons at the surface of AuNPs generating their collective oscillation that is in resonance with the frequency of the impinging electromagnetic wave [42], [43], [44]. The SPR depends on the size, shape particle distance and dielectric surrounding [45]. In LFIAs when light impinges in the AuNPs the surface electrons experience collective oscillation by absorbing light in one area of the optical spectrum and reflecting light in a different area of the optical spectrum. The generation of visible color test and control line is due to the high density of AuNPs in very small area [46].

2.3 POC DIAGNOSTIC SYSTEMS FOR INFECTIOUS DISEASES

The simplest methods to read the results is to observe with the naked eye the changes in color intensity of the test line in LFIAs. However when quantitative analysis is required this method is not sufficient and an external electronic system is necessary to interface with the LFIAs. The basic system consist of a light source to emit light at the LFIA, a light detector and a processing system to process the results (details of these components are provided in Chapter 3).

The POC system should have characteristics that will complement those of the LFIA such as low cost, low power, being hand-held, robust and easy to operate [47]. Furthermore, significant attention should be given to factors that could degrade its performance, such as positioning error and light homogeneity. The test line position is not always constant but can shift either during the fabrication process or because the backing strip size varies or even because the strip is shifted during insertion into the system. A system that does not take into account the possible shift of the test line is susceptible to positioning errors. Even a 4% shift can result in up to 50% reduction in

measured signal [36]. The light distribution across the area of interest in the LFIA should be homogeneous, so that the sensor can accurately read the results.

In the literature several systems have been proposed to be used as POC readers for LFIAs. The main categories among them are the smartphone readers, spot detectors, scanners and telemedicine readers as shown in Figure 2.7

- **Smartphone camera-image analysis**

The most common reader is based on image analysis. A photograph of the test strip is taken – usually using the camera of a mobile phone and the image is processed using the mobile phone's resources, as shown in Figure 2.7 (a). If the photograph is taken using a standalone camera the image is sent to a computer for processing using image analysis programs. Even though these types of readers have fast implementation and a high quality image can be captured, they are affected by ambient light, focal distance, shading, and tilt [47], [30], [32]. Image processing techniques can be used to decrease the effect of these parameters but require extended processing power and consume considerable amounts of energy. Another solution widely applied is the development of custom enclosure around the LFIA and the camera of the mobile as shown in Figure 2.7 (b). However, in these cases, the systems usually becomes more complicated and additional optical components are needed, like lenses and light emitting diodes (LEDs). This is because the flashlight of the mobile phone is not optimized for a suitable wavelength for the tested LFIA, and its light intensity typically needs regulation. Furthermore, the existing lens in the mobile phone camera usually needs to be tenths of centimetres away from the reading object in order to focus correctly and thus by using an additional lens the focus distance can be reduced. With all the extra optical components that must be added, the main advantage of fast implementation is lost. Also, the mobile phone-based camera readers have reproducibility issues because different models of mobile phones have a wide range of cameras with varying resolution and diverse lenses which can give divergent results. Again, with intensive image processing analysis the reproducibility issues can be reduced. In addition, mobile phones have standardization and regulatory issues when used for biomedical sensing applications [48].

- **Telemedicine**

In telemedicine method, a photograph of the LFA is taken and it is sent off-site either via SMS or e-mail to a healthcare centre for analysis, as shown in Figure 2.7 (c). Afterwards, the results are send back via the same method. If the photograph of the LFA is taken using a mobile phone, the aforementioned errors regarding the image quality will also apply in this method. In addition, a stable mobile phone signal is required for effective transmission and reception of the data.

- **Single photodiode system**

The other major type of readout device is based on discrete optical components like lenses, fibres, optical splitters to direct the light into single photodetector, placed in position where the reflected light from the test line is expected to impinge [49], [32], as shown in Figure 2.7 (d). Even though these systems are simple and have low cost, they are susceptible to positioning errors that can be created due to possible shift of the test line with respect to the position of the photodiodes.

- **Scanner**

The scanners are systems that use a mechanical motor to move the strip across photodetector and therefore measure the reflected light from the entire strip [50], as shown in Figure 2.7 (e). While these systems are not prone to positioning errors, the extra moving parts makes the device bulkier, heavier, and fragile [32]. Therefore they are not suitable to be carried around as POC readers.

- **Light transmittance**

In the light transmittance method, the strip is initially pre-processed (usually by wetting it) in order to make it translucent, as shown in Figure 2.7 (f). Then a system of discrete components measures the absorbance of the light as it passes through the test line. This method becomes more complicated with the required extra steps needed to modify the paper and a careful seal between the electronics and the wetted strips is required. Also the light transmission is very dependent on the width of the strips.

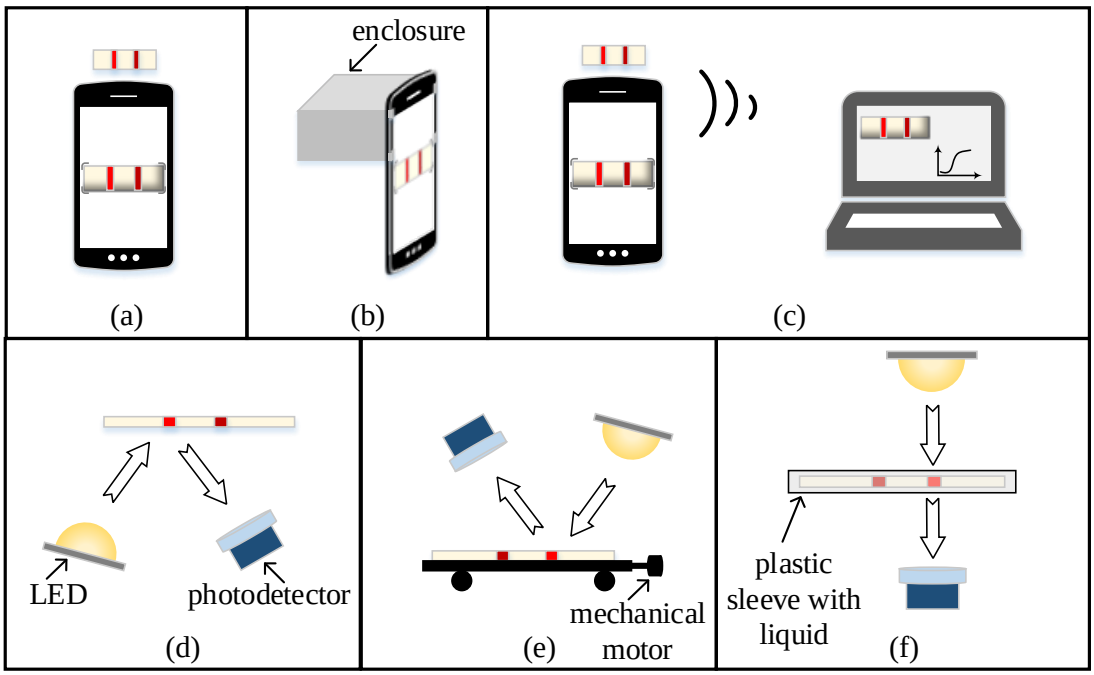

Figure 2.7 Schematic representation of the different readout methods (a) Image analysis of a picture from a smartphone camera (b) Image analysis of a picture when an enclosure is used between the camera and the LFA, (c) telemedicine, (d) reflection light measurement using single photodetector, (e) scanner and (f) light transmittance.

Method	Advantages	Disadvantages
Smartphone camera-image analysis	• Easy and fast implementation.	• Lighting conditions, focal distance shading and tilt affect the results. • Problem with reproducibility of the results with different mobile phone cameras. • High power consumption. • Standardization and regulatory issues.
Smartphone camera-image analysis, with enclosure	• Medium time for implementation. • High sensitivity.	• Problem with reproducibility of the results with different mobile phone cameras. • High power consumption. • Standardization and regulatory issues.

Telemedicine	• Easy and fast implementation. • High sensitivity.	• Depend on network reception. • If a smartphone camera is used to take the picture, all the drawbacks of smartphone camera method will be also applicable in this system.
Single photodiode system	• Low complexity. • Low cost. • Low power consumption.	• Results susceptible to positioning errors. • Fragile system (if optical accessories are used).
Scanner	• High sensitivity. • Medium complexity.	• Bulky and fragile system.
Light transmittance	• Detection of low concentrations. • Medium complexity	• Pre-processing of the LFA is required. • Results are susceptible to strip width.

Table 2.2. Summary of methods used for colorimetric detection of LFAs.

2.3.1 READERS COMPARISON

An overview was performed for different systems, which were proposed in previous studies to quantify the analyte in LFAs. In addition, these systems were compared for the most important characteristics that the POC readers must display, as shown in Table 2.3. Each characteristic has a mark between high, medium and low.

In [51], a system to quantify the results in LFAs is presented. The system consists of a smartphone to take a picture of the test strip and a box with a lighting system to keep the mobile phone and the LFA at a constant distance and to provide ambient light shield. The captured image is then processed using machine learning techniques and the output of the trained system quantifies the result in one of the 6 predefined categories (semi-quantification). Due to the use of the machine learning algorithm this system is considered to have high complexity, high power consumption, and medium cost mainly due to the mobile phone price tag. It is robust and it is not affected by ambient light and positioning errors because of the use of the enclosure. Even though

the system was tested with 3 different iPhone models, it still has reproducibility issues between other brands and models of mobile phones.

A mobile phone-based reader for LFIAs is presented in [52]. It uses an attachment to the mobile phone to keep the light conditions in the strip constant. That attachment has LEDs, batteries and a lens for the capture of image under controlled lighting conditions. The image was processed on the mobile phone using a custom application. This system has medium complexity due to the hardware and software developments. Due to the use of an extra lens, the system becomes more fragile. Also, in order for this system to be compatible with different mobile phones, alterations are required in the attachment and application.

A system based on single photodiodes is presented in [49]. The light of an LED source is split using an optical splitter evenly in the 10 test lines of a multiplexed LFA. The reflected light from the test lines is measured using 10 single silicon photodetectors positioned in the area where most of the reflected light is expected to impact. This system has low cost, low power consumption and demonstrates the ability to measure multiple analytes at the same time using a system with few components. However, this design is highly affected by positioning error due to the possible shifting of the test lines compared to photodetectors.

Another system based on single photodiodes was presented in [53]. As before, an LED was used to shine light onto the strip and the intensity of the reflected light to the test and control lines was measured using two photodiodes. This system was able to provide semi-quantitative results but it demonstrated high variability in the measurements of different test strips. This was due to variations in the LFAs in the gold/antibody conjugation, dimensions of the paper strip and positioning errors. In addition, the use of test and control lines in the quantification measurements might have influenced the variation in the results. The system has low power consumption, easy implementation and low cost.

A system based on a scanning method was introduced in [50]. It used a laser diode to shine light onto the LFA. Lenses were used to focus the light on a square area of interest and to collect the reflected light and direct it to a photodetector. A motor was employed to shift the platform holding the LFA. The collected data were analysed in a computer using customized software. This system can overcome reproducibility

issues and positioning errors because it scans the entire LFA area. However, it is not suitable for POC measurements because it uses many fragile components such as lenses and mechanical parts. Also it has high power consumption due to the use of moving parts.

The light transmittance method was employed as a quantification method in [54]. Initially the strips is wetted by placing it in a plastic sleeve containing a liquid. Then both strip and sleeve positioned in the device. The wetted strip becomes almost transparent, therefore when the LED shone light on top of a specific area of the strip, a photodetector positioned at the back of the strip measured the transmitted light. Even though this system has the potential to measure very low concentrations it is affected by the LFA paper type and width. Also, it is not user-friendly as it requires extra processing steps before the measurements are available. Furthermore, it can be affected by positioning errors given that a single photodetector is used below the area of interest for measurements.

The majority of the commercially available LFA systems are specifically designed to be used in labs and healthcare centres. Therefore, they are not necessarily optimized to have the important specifications required from POC systems such as low power consumption, low cost and high robustness. For example the Alere Reader [55], requires a plug-in power supply to operate. On the other hand, the few systems that are handheld and can be used as POC systems come with a hefty price tag. An example is the reader from BioAssay Works [56], which is handheld and battery powered, but costs more than $2700. In addition, another problem with the commercially available systems is that they are designed to be used mainly with LFA strips offered from the same company and therefore demonstrate compatibility issues.

Reference	Method	Cost	Power consumption	Robustness	Reproducibility	Positioning error
[51]	Smartphone camera-Image analysis, with enclosure	Medium	High	High	Medium	Low
[52]	Smartphone camera-Image analysis, with enclosure	Medium	High	High	Low	Low
[49]	Single photodiode system	Low	Low	Medium	High	High
[53]	Single photodiode system	Low	Low	High	Medium	High
[50]	Scanner	Medium	High	Low	High	Low
[54]	Light transmittance	Low	Low	Medium	Medium	High

Table 2.3. Comparison between different systems proposed in the literature as POC readers for LFAs.

2.3.2 GAP IN READERS MARKET

Even though there are many systems that have been proposed to be used as POC readers for LFAs, still none of them can perform quantification measurements, while combining the specification of low cost, low power, high robustness, high reproducibility and low positioning error. On the other hand the commercially available readers are not suitable for use in developing countries either because they are not designed for out of lab measurements in field settings or because they are very expensive. Consequently, there is immediate demand for systems that can quantify the results of LFAs and that will have all the aforementioned specifications.

2.4 DISCUSSION

Influenza virus does not just cause seasonal epidemics, but has caused some of the deadliest pandemics. Therefore, the detection of influenza virus along with other infectious diseases is very important in order to facilitate treatment for the patient and public health precautions for the community. Paper-based biosensors, and more particularly lateral flow immunoassay biosensors, are suited for use in developing countries and resource limited settings. This is because of their many advantages such as low cost, requirement for small fluid sample, they can be stored for long periods of time and can be easily carried around. When the sample flows along the LFIA strip a color change at the test line indicates the presence of the analyte of interest. The intensity of the color change is related to the concentration of analyte of interest, whereas the color change can be quantified using an external electronic device. The device, however, should not compromise the advantages that the LFIA has but instead should be able to show similar specifications. From the review performed on the different proposed systems it is noticeable that none of them can combine all necessary requirements for POC system. As a result, there is demand for diagnostic devices that can combine all the important specifications of a POC system.

2.5 CONCLUSION

From the analysis of this chapter the following conclusions can be drawn:

- Influenza virus has many subtypes and can be transmitted from animal to human therefore, it is difficult for the population to acquire immunity to all variants of the virus.
- Diagnostic systems that operate as readers for biosensors that will be used in developing countries should comply with the ASSURED requirements.
- Lateral flow immunoassays are biosensors with properties that makes them ideal to be used in developing countries and remote resource-limited settings.
- The POC systems that are designed to interface with LFIAs to offer quantification capabilities should have the following specifications: low cost, low power, high robustness, high reproducibility and low positioning error. Even though there are several diagnostic systems proposed in the literature, little effort has been given to combine all these specifications together.

3

NOVEL LFIA READER SYSTEMS

Various systems that interface with LFIAs in order to provide quantification results have been proposed. However, the majority of these systems are not specifically designed to be used as POC systems for developing countries and thus, lack important characteristics.

Chapter 3 outlines the design, implementation and testing of two systems that were developed as readers for LFIAs. The first system is a proof of concept that demonstrates the capabilities of the proposed reading method. System performance is verified by testing the device with LFIAs with Influenza A nucleoprotein in various concentrations. Next, a second generation system is presented which consists of the optimized version of the proof of concept system. Optimization of the system was performed by defining the surface profile of the LFIA using a ray trace simulation program. Based on the simulation results a device was developed using discrete components. Verification of its performance was achieved by testing it with Influenza A nucleoproteins FLIAs and Surface-layer protein A LFIAs.

3.1 INTRODUCTION TO PRINCIPLE OF OPERATION

The proposed system is a reader device for the quantification of the analyte in LFIAs. The aim was to design a system that could be used at the POC, especially in developing countries, while realizing all the specifications required from such systems as demonstrated in chapter 2, i.e. low cost, low power consumption, high robustness, high reproducibility and low positioning error.

The developed system is based on the colorimetric method. LEDs were used as light sources to shine uniform light on the detection pad of the LFIA and the reflected light from the LFIA was measured by an array of photodiodes. The intensity of the reflected light at test and control lines is less than the intensity of the reflected light from the rest of the strip. This is because the gold nanoparticles that are present in the two bands absorb a portion of the light at certain wavelengths, while the rest of the strip, which is white color, reflects all the wavelengths. At the same time, the density of gold nanoparticles in the test and control lines is proportional to the absorption of the light resulting in the quantification capabilities of the LFIA [36]. Figure 3.1 shows the principle of operation of the proposed system.

By utilizing an array of photodiodes as the reading element, the scan of the entire area of interest is achieved without the use of any moving parts and without losing any useful information due to strip displacement. Furthermore, by placing the strip and the array of photodiodes at close proximity (few millimetres), no lens is required, therefore achieving a compact robust design. Also, in comparison with the mobile phone camera systems, the proposed system is simpler and uses sufficient but smaller number of pixels to read the strip, thus achieving reduced power consumption. Additionally, the reader can operate for a variety of LFIAs tests and control line widths and positions in comparison to single photodiode systems [32]. Finally using a custom enclosure, problems related to ambient light, focal plane or tilt can be eliminated.

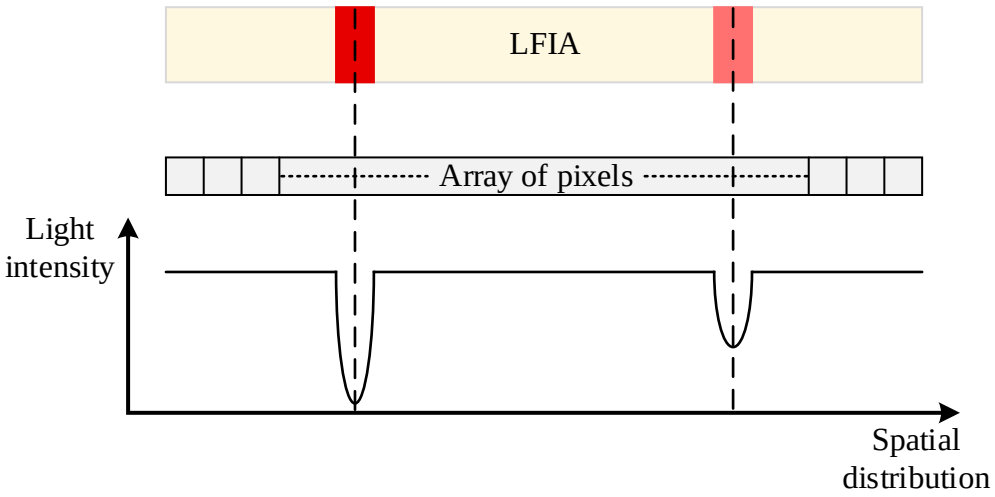

Figure 3.1 Schematic representation of the principle of operation of proposed system. The reflected light at the test and control lines is lower compared to the rest of strip.

3.2 First generation Reader

A first generation proof of concept system was implemented using discrete components. As a photodetector an array of photodiodes with suitable size to match the tested LFIA was chosen. The dimensions of the LFIA test strips are shown in Figure 3.2.The typical size of the test and control lines is between 0.8 mm to 1 mm and distance between the two lines is around 4 mm. The detection pad is approximately 20 mm and the whole strip used is 6 mm. The depicted array of photodiodes has 128 pixels with approximate pixel size of 63.5 µm × 63.5 µm, and overall photosensitive area size around 8 mm, which is sufficient to detect the test and control lines and some area around them. This large photosensitive area minimises possible positioning errors due to shift of the LFIA.

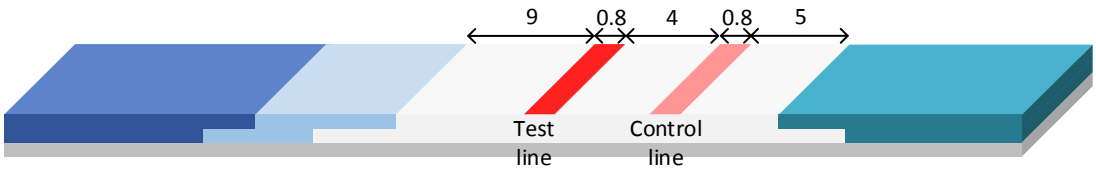

Figure 3.2 Discerption of the dimensions of the tested LFIA. All values are in millimetres.

Eight small white color LEDs (from Panasonic) were used as light source. These were placed in the same printed circuit board (PCB) as the linear sensor array (TSL1401CL, ams AG), with four on each side in order to achieve uniform lighting conditions in the detection pad. Figure 3.3 shows a schematic diagram of the proof of concept system setup. The light from the biosensors is reflected onto the 128 pixels of the linear sensor array and each pixel produces a photocurrent that is integrated within the pixel and clocked out sequentially at a rate of one pixel per clock period. The clock frequency is 7 kHz, which is among the lowest frequencies that the linear sensor array can operate on. This was chosen in order to allow maximum light collection from the photodiodes. A microcontroller (Atmel, Arduino Uno) was used to generate all the digital signals, while its 10-bit ADC was used for the digitization of the output voltage of each pixel. Further processing of the signal and the calculation of the concentration of analyte in the sample was also performed in the microcontroller. The digitized output data were then transmitted wirelessly via Bluetooth to an open source application of a smartphone [30].

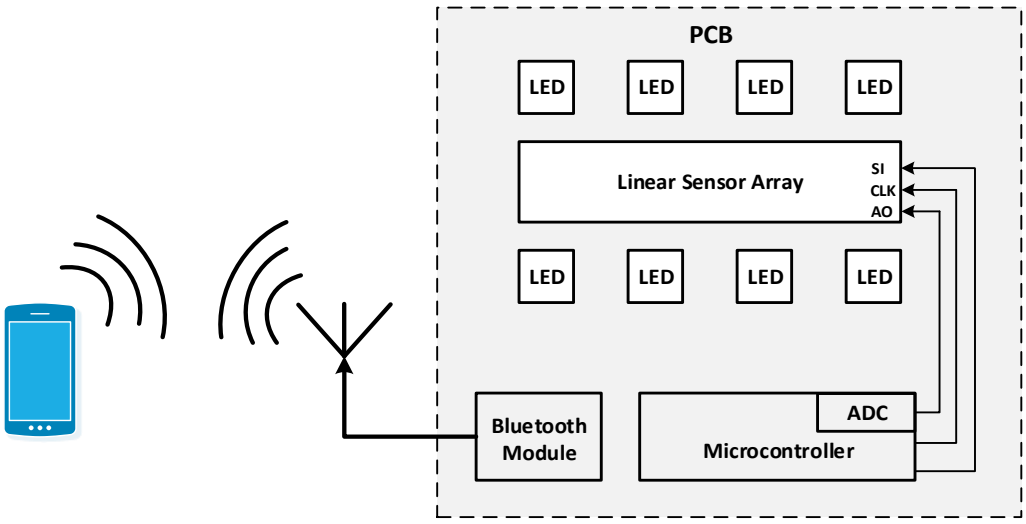

Figure 3.3 Schematic diagram of the first generation proof of concept reader.

Additional components were used for the correct operation of the system such as oscillator and decoupling capacitors. The system was power by a 9V battery and was enclosed in a small black box (such that the performance of the device was not affected by the ambient light) with dimensions 110 × 82 × 40 mm, which was appropriately modified. The strip was inserted into the box via a slot, which helped to align the strip horizontally with the detection pad exactly on top of the array of photodiodes facing

one another. Figure 3.4 shows photographs of the first generation proof of concept system.

Figure 3.4 Photographs of the proof of concept system.

3.3 TEST AND RESULTS

The performance of the device was validated using commercially available strips (BD Directigen) in a variety of concentrations (0-500ng/mL) of Influenza A nucleoprotein, as shown in Figure 3.5. Each sample was prepared using 300µL recombinant nucleoprotein antigen (ORLA 108) diluted in phosphate-buffered saline (PBS) and then added to a tube containing 100µL detergent. After the tube was slightly vortexed, 3 drops of this solution were added in the sample pad of the test strip.

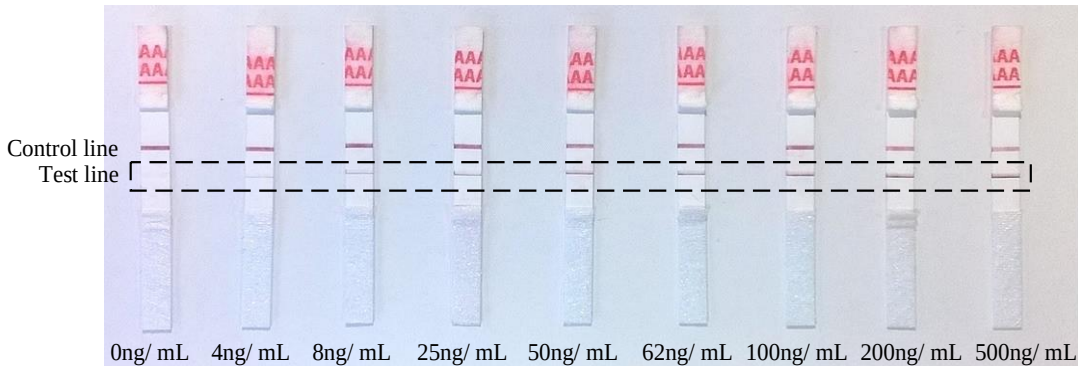

Figure 3.5 Photographs of LFIAs in various concentrations of Influenza A nucleoprotein.

As shown in Figure 3.6, the output signal from each pixel for each different strip follows the expected trend. Initially, the color of the biosensor is white, and then the first color line that represents the test line appears. A sharp decrease in the reflected light intensity is observed. A neutral white color area then follows before the next color line that represents the control line appears. In the space between the two color lines, the reflected intensity increases before it lowers again as a result of the second color line. Near the end of the strip, a small fluctuation of the output signal from the pixels is noticeable. This is due to sudden light reduction and the wide angle that is created resulting in an image distortion. There is a slight shift in the position of the minimum value for the different strips. However, such variations do not affect the performance of the system as scanning is performed in the entire detection pad and the detection of the minimum value is performed automatically [30].

The microcontroller was programmed to automatically detect the signal from the test and control lines. This is achieved by detecting the minimum value between the first 50 pixels of each strip and then the average value of this minimum and the minima of the ±4 adjacent pixels is calculated. The calculated value corresponds to the signal of the test line (S_T). The overall average value of 9 pixels was used because it is the number of pixels that approximately collect most of the reflected light from the test line. The same procedure was performed for the calculation of the signal of the control line (S_C), but the minimum value of pixels 90 to 120 was used instead [32].

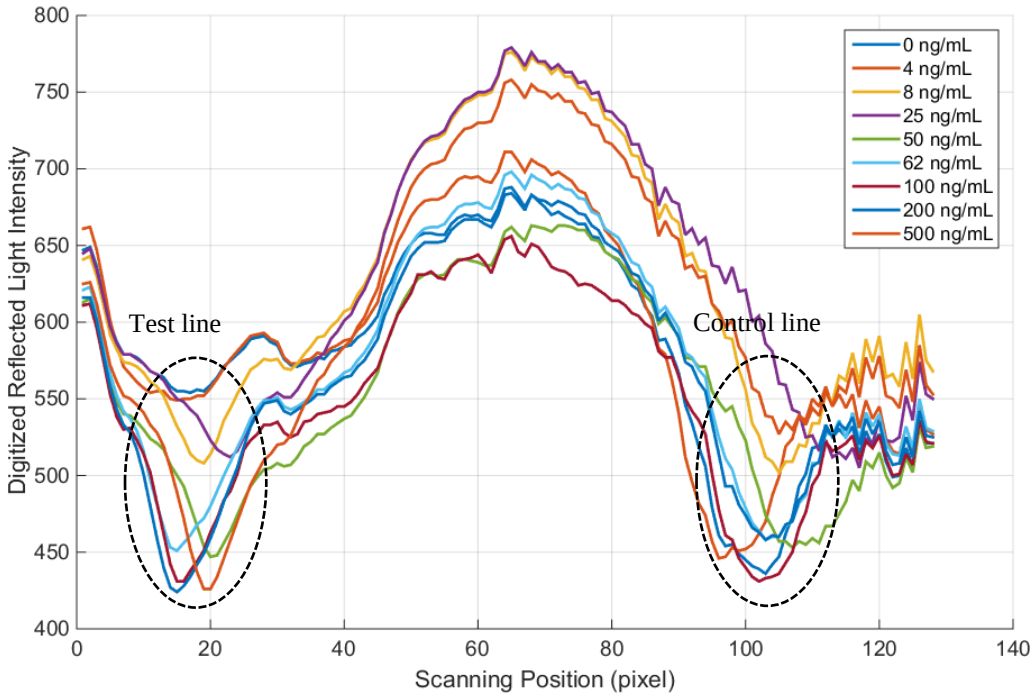

Figure 3.6 Intensity values measured from each pixel, for different concentrations of Influenza A nucleoprotein.

The signal S_T from each strip was calculated 10 times. Then the average S_T signal was used for the generation of the calibration curve, as shown in Figure 3.7. The standard deviation from the 10 measurements is added in the calibration curve and is indicated with an error bar. To generate the calibration curve between the concentration of analyte and the signal from the device (S_T) the four parameter logistic (4PL) model was employed. This model is commonly used in bioassays for the fitting of analyte concentration and measured signal following a sigmoidal shape on a semi-log axes [57], [58], [50]. The 4PL model is described in Equation 3.1.

$$y = d + \frac{a - d}{1 + \left(\frac{x}{c}\right)^b} \tag{3.1}$$

where y is the measured signal S_T; x, is the concentration of analyte; a is the response in minimum concentration; d is the response in maximum concentration; c is the concentration of analyte for the point halfway between a and d; and b the slope parameter. Based on the measured values, MATLAB (MathWorks, Massachusetts,

USA) was used to compute the unknown parameters of Equation 3.1. The quality of data fit was determined by the coefficient of determination R^2:

$$R^2 = 1 - \frac{SSE}{SST} \tag{3.2}$$

where *SSE* is the error sum of square and is calculated as $SSE = \sum_{i=1}^{n}(y_i - \hat{y}_i)^2$, *SST* is the total sum of square error of the baseline in average response and is calculated as $SST = \sum_{i=1}^{n}(y_i - \bar{y}_i)^2$, *n* is the number of data, *y* is the measured data $\hat{y}$ is the fitted data and $\bar{y}$ is the data in regards to the baseline in average response [59]. The coefficient of determination is bound between 0 and 1, $0 \leq R^2 \leq 1$, with 0 meaning weak data fit and 1 meaning perfect data fit. The fitted curve is shown in Figure 3.7. The calculated parameters are $a = 411.6$, $b = -0.92$, $c = 34.27$, and $d = 533.3$, with coefficient of determination $R^2 = 0.946$. The limit of detections was measured at 3ng/mL.

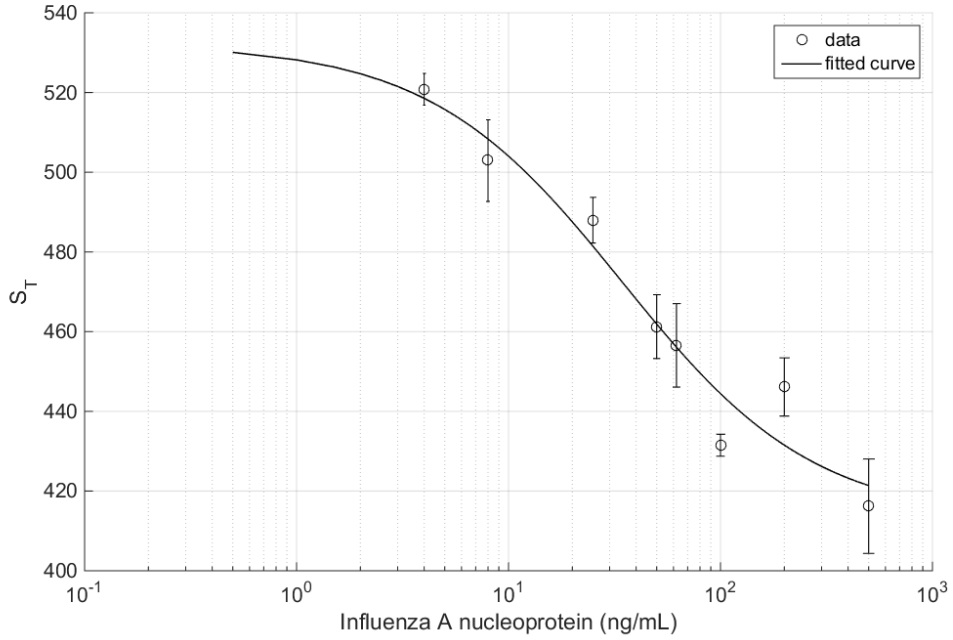

Figure 3.7 Calibration curve of the proposed system. The error bars indicate the standard deviation.

The first generation reader has been successfully used for the detection of influenza A nucleoprotein in various concentrations, with limit of detection at 3ng/mL, highlighting the significant advantages that this type of reader has to offer compared

to other type of readers, in terms of ease in implementation and operation, reproducibility of the results and low cost. However, the limit of detection of the first generation system was not significantly low and the variation of the results still required improvement. Also, the power consumption of the reader has not been optimized, therefore further reduction could be achieved.

3.4 SECOND GENERATION READER

After the successful implementation of the first generation/proof of concept reader, the second generation reader was realised. The main objectives of the new system were to optimize the setup in terms of best positioning of all the critical components (LEDs, LFIA and array of photodiodes) and use the optimum number of LEDs, in order to achieve uniform light distribution across the reading area of the LFIA. By improving these parameters, the performance of the reader can also be improved in terms of sensitivity and power consumption compared to the first generation system. Optimization was achieved by:

1. Changing the wavelength of the light source to match the optical characteristics of the gold nanoparticles present in the tested LFIA.
2. Modelling the optical behaviour of the surface of the tested LFIA
3. Modelling all the critical components and simulating their optical behaviour using a Ray Trace simulation program.

3.4.1 OPTIMIZATION METHOD

The optical characteristics of the gold nanoparticles among others depends on their size and shape. Figure 3.8 shows the absorbance of gold nanoparticles for different diameter sizes [43]. The diameter of the gold nanoparticles in the tested LFIA is between 20nm to 40nm and thus highest light absorption occurs in green wavelengths (≈525nm) and highest light reflection in red wavelengths (≈700nm). This explains why the test and control lines appear as red lines in ambient light. Based on Figure 3.8, all the LEDs used in the reader were changed from white color (as in the

first generation system) to 525nm wavelength instead. By changing the wavelength of the light source to suit the specifications of gold nanoparticles only the green wavelengths are absorbed from the test and control lines and only the red wavelength are reflected in the white parts of the strip and therefore, no other wavelength is affecting the results.

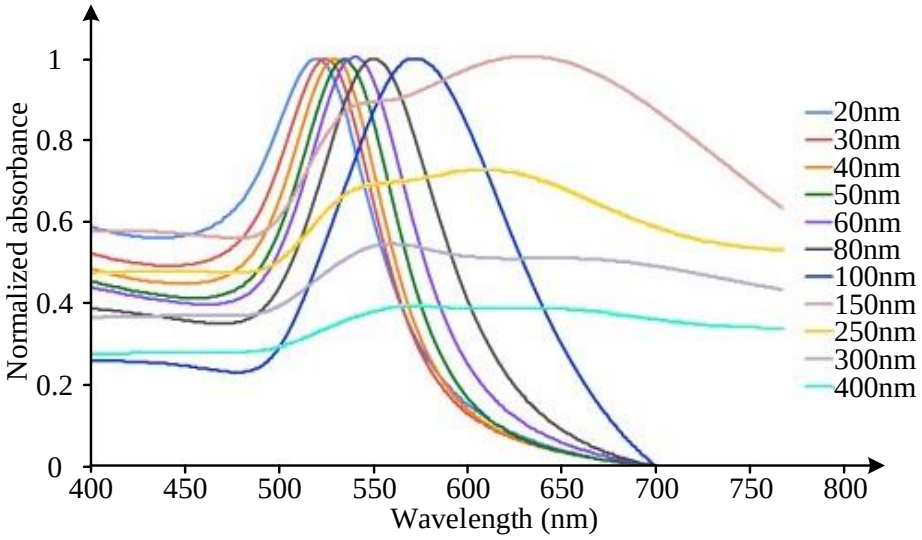

Figure 3.8 Normalized absorbance of gold nanoparticles for various gold nanoparticles diameters (reproduced from [43]).

In order to simulate the system and identify the optimized setup a ray trace simulation program (Zemax OpticStudio) was used. In this software all the critical components (light sources, photodetectors, LFIA) were modelled based on their actual size and their optical behaviour. However, the LFIA has porous surface that during the measurements is also wet and its optical behaviour is not well known. Therefore, the construction of a model that defines the light distribution in the surface of LFIA was required. The bidirectional scattering distribution function (BSDF) data were measured for the construction of the LFIA's surface profile [60].

The BSDF describes the scattered light from a surface in regards to the angle of incident light. The BSDF includes both the components of reflected scattered light (bidirectional reflectance distribution function, BRDF) and the transmitted scattered light (bidirectional transmittance distribution function, BTDF) [61]. In the specific application, only the BRDF is of interest. Mathematically the BRDF is described as the ratio of the reflected light radiance (L_r) to the incident light irradiance (E_i) [62],

[63], [64] as it is shown in Equation 3.3. Figure 3.9 illustrates the reflected light from a scattering surface.

$$BRDF = \frac{dL_r(\theta_r, \phi_r)}{dE_i(\theta_i, \phi_i)} \tag{3.3}$$

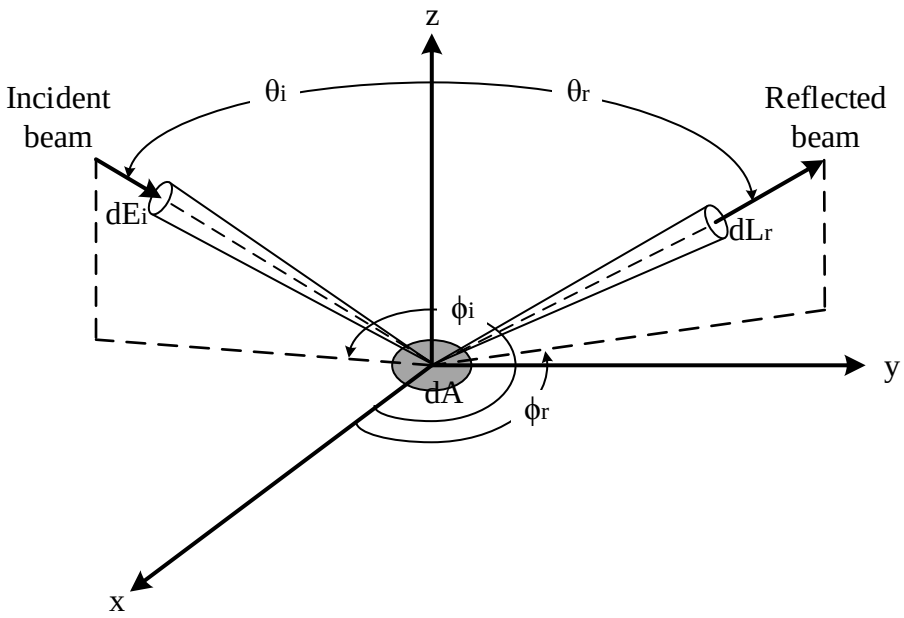

Figure 3.9 Light reflection from a scattering surface (redraw from [64]).

The BSDF is usually measured experimentally with the help of a goniometer, imaging sphere or any other custom-made setup. In these experiments the imaging sphere (Radiant Vision Systems) was employed [60]. It has a light beam to illuminate the surface at various angles (one at a time) and then measures the scattered light from the surface to a camera. Due to the highly reflective coating on the inside of the sphere and the convex mirror, the camera is able to measure the reflected radiation distribution over a full hemisphere (azimuth and elevation angle) [65]. Figure 3.10 shows the configuration of the imaging sphere as well as its photograph. A BSDF is generated in the form of tabular data, which defines the scattering properties of the surface. For an accurate model of the LFIA using the imaging sphere, a test strip with high concentration of Influenza A nucleoprotein was used. The incident beam used in the imaging sphere had wavelength 525nm, which matches with the wavelengths of the LEDs used in the system. Two BSDF models were generated; one for the white

part of the strip and one for the part of the strip with the test line (the control line will have a similar response as the test line) [32].

The generated BSDF data file is a text file with information for each selected angle of incidence in a table format of 181 × 181 data of scattering azimuth angles and scatter elevated angles. The percentage of the scattering light for each incident angle is also calculated. The remaining percentage is due to absorption or transmission [66].

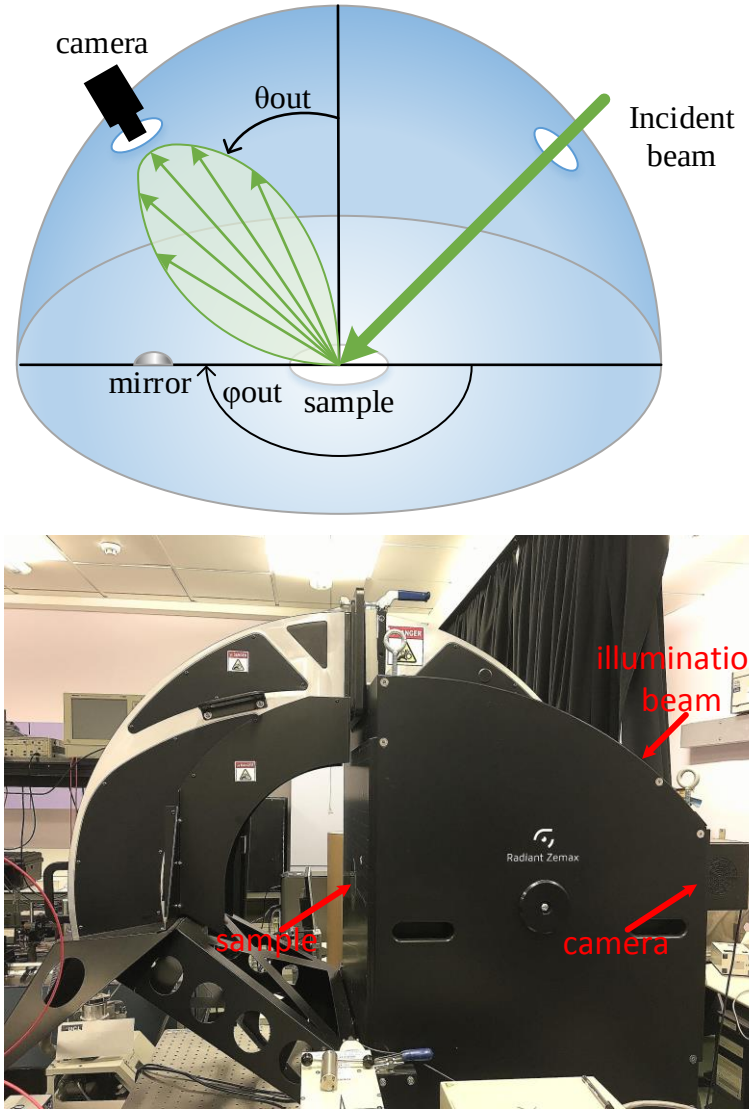

Figure 3.10 Imaging sphere (a) configuration where ϕ_{out} and θ_{out} shows the azimuth and elevation angles of reflected radiation (b) photograph.

The detection pad area, as opposed to the entire LFIA strip, was modelled in the ray trace simulation program, as this is the most important segment of the LFIA with

the test and control lines. The BSDF model from the white part of the strip was used as the surface profile for the white parts of the detection pad. Two small rectangular surfaces were positioned on top of the modelled detection pad to represent the test and control lines. The BSDF data from the test line that were recorded from the imaging sphere were imported in the program to represent the surface characteristics of the test and control lines of LFIA. The array of photodiodes were modelled as a photodetector with 1 × 128 pixels with size the same as the real array of photodiodes. The LEDs were modelled as point light sources, with the same optical characteristics as the actual LEDs used. The real dimensions of the LEDs were considered in order to accurately position each LED in the simulated setup. Simulation and analysis were performed in the ray trace simulation program in order to define the optimum setup.

A similar setup as in the first generation system was simulated as shown in Figure 3.11. The LEDs and the array of photodiodes were both placed on the same PCB facing upwards and the LFIA was positioned on top of the PCB facing downwards.

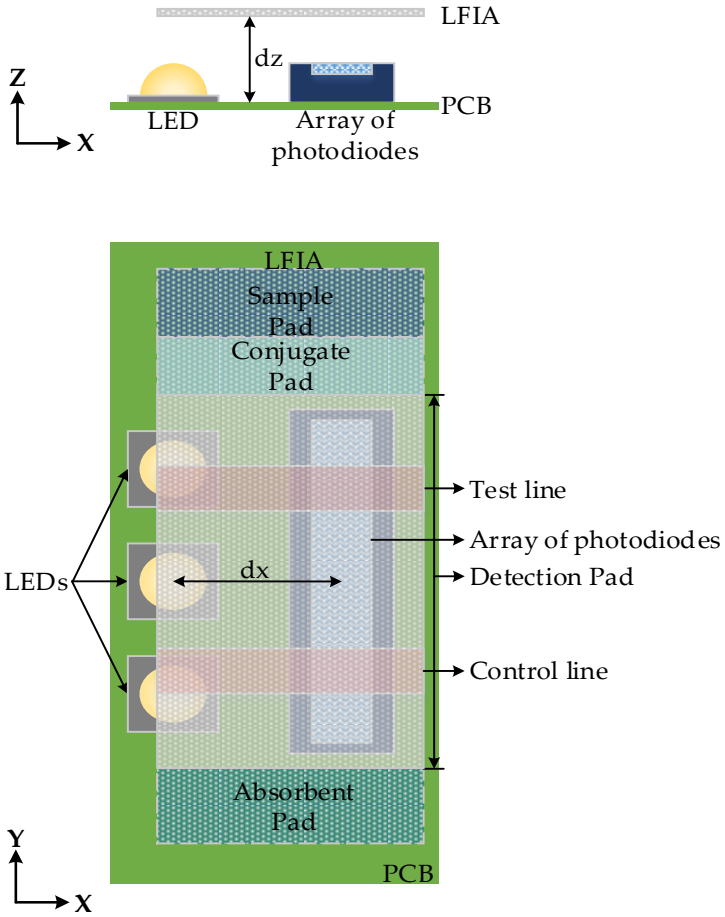

Figure 3.11 Simulation setup: plan and elevation (not to scale)

Firstly, the optimum number of LEDs needed to uniformly illuminate the detection pad of LFIA was defined. In order to do that, the 8 mm detection pad area (without any test or control lines) of LFIA was divided into eight distinct equal strips (1 mm each) and was placed above the LEDs (dz = 2 mm) and the array of photodiodes. The total power per mm^2 that hits each strip was measured and the maximum variation in irradiance was calculated. The same measurements were performed for varying number of LEDs (one to four). Figure 3.12 shows the normalized irradiance for each area in the detection pad. The LEDs were equally spaced along the y-axis to cover the detection pad area. As the minimum variation is similar for three and four LEDs, three LEDs were chosen in order to minimize the power used.

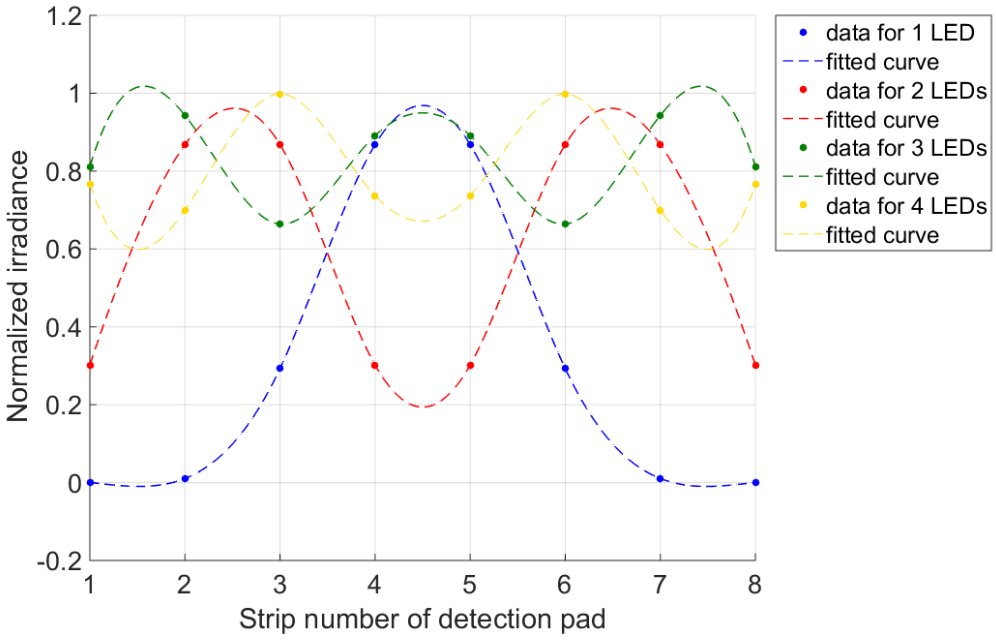

Figure 3.12 Normalized irradiance in each of eight 1mm detection pad strip when the impinging light is performed by varying he number of LEDs from one to four.

All subsequent simulations were, thus, performed using 3 LEDs. Next, in order to define the optimum distance with respect to the array of photodiodes in z-axis a parametric analysis was performed for dz = 2 mm to 5 mm. The simulated LFIA had test and control lines with surface optical properties based on the extracted BSDF data of the imaging sphere. The centre of the test line and the centre of the control line were 5 mm apart, as in the practical test strips used. As shown in Figure 3.13, the further

away the LFIA is from the array of photodiodes, the more the light diffuses in more pixels and the less distinguishable are the lines in the strip. The different parts of the strip (test line, white part, control line) are more distinct when *dz* is 2 mm (this was the minimum practical distance).

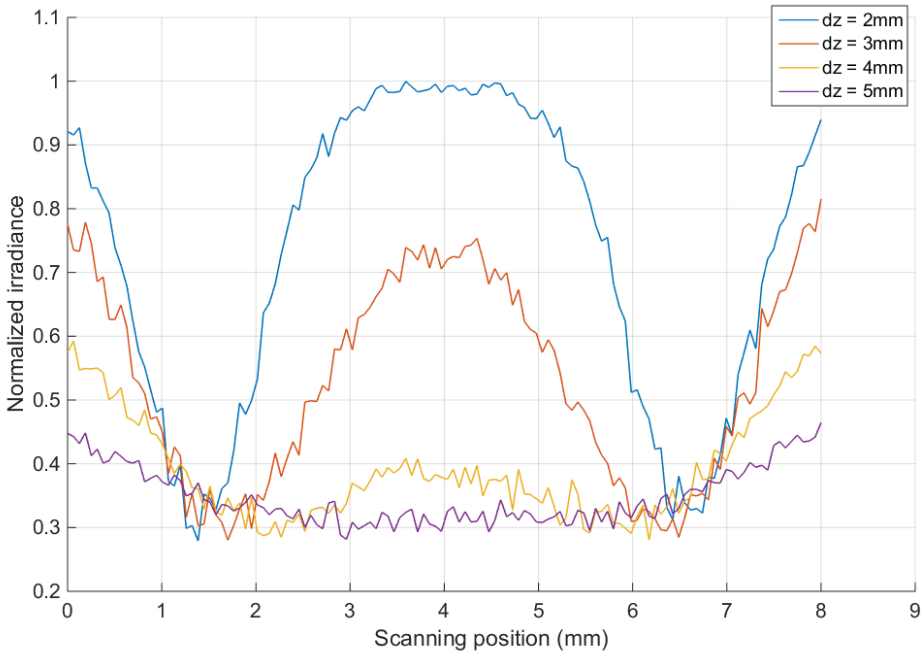

Figure 3.13 Normalized irradiance across the array of photodiodes when the *dz* varies from 2 mm to 5 mm and three LEDs are used.

The irradiance striking the photodiodes was simulated for different values of dx when *dz* = 2 mm. The results are shown in Figure 3.14. The most sensitive detection of the test and control lines is when *dx* = 2.5 mm. It should be noted that all the distances are measured from the centre of the LEDs to the centre of the array of photodiodes. A distance less than 2.5 mm was not considered possible due to component sizes and PCB manufacturing constraints (the PCBs were manufactured in the university facilities).

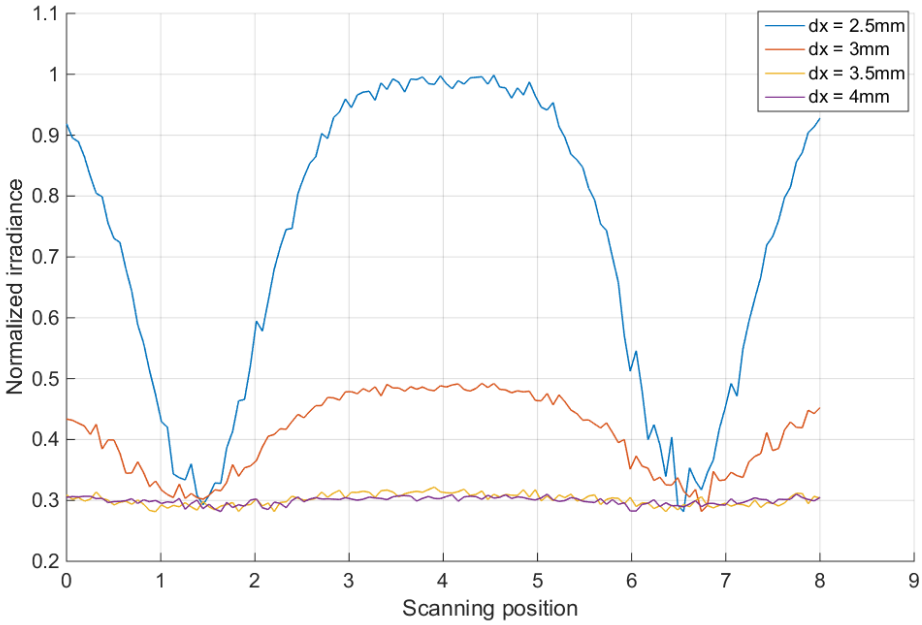

Figure 3.14 Normalized irradiance across the array of photodiodes when *dx* varies between 2.5 mm and 4 mm.

The irradiance across the array of photodiodes was also investigated when the LFIA is tilted in the y-axis by 0, 10, 20 degrees. The tilt is performed from the centre of the LFIA, therefore that point has a constant *dz* = 2 mm. The same setup as in Figure 4 was used but the LFIA was tilted as shown in Figure 3.15. Figure 3.16 shows the largest difference (highest sensitivity) between the peaks and valleys of the irradiance is for a tilt of 10 degrees.

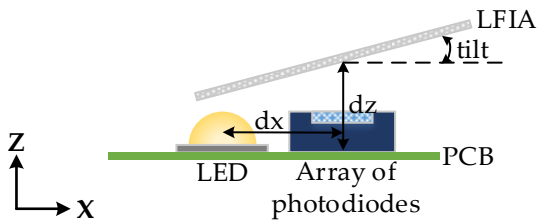

Figure 3.15 Details of the tilt position, dx = 2.5mm and dz = 2mm.

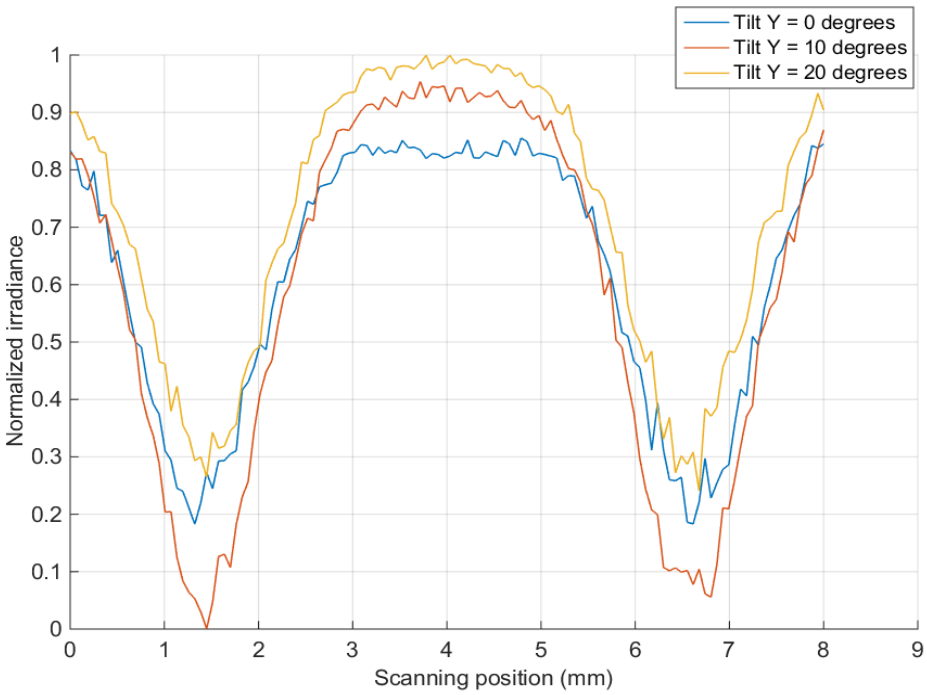

Figure 3.16 Normalized irradiance across the array of photodiodes when the strip is tilted in Y - axis from 0 to20 degrees.

3.5 IMPLEMENTATION AND TESTING

The optimized reader was realized based on the simulations results from the ray trace simulation program, as discussed in Section 3.4. All the components that have been used are commercially available. The three LEDs (Kingbright) have a wavelength of 525 nm, which is an approximate match to the absorption characteristics of the nanoparticles in the tested strips. Their dimensions are 1.6 mm × 0.8 mm × 0.95 mm each, which fit well to the requirements of the model. The maximum optical power of the LEDs was adjusted such that the light falling on the array of photodiodes does not saturate the pixels and provides a wide dynamic output range. The measurement method is based on the ratio of the signal in the test line to the signal in the control line, and to a first order the result is independent of LED optical power variations due to diode or power supply variation.

The same light detector as in the first generation reader has been used which has a line of 128 photodiodes extending over 8 mm (AMS-TSL1401CL). The same

microcontroller as in the first generation reader has also been used for the process and digitization of the analog output into its 10-bit analog-to-digital converter (ADC). A new low-power Bluetooth module has been used for the wireless transmission of the results to an open source app of a smart phone. All the electronic components were enclosed in a box specifically designed for this application using a 3D printer. A special carrier with small clips was designed for the LFIA so that the strip could be placed in the right position in the reader (above the array of photodiodes) with 10 degrees tilt as simulated in the ray trace analysis program. Figure 3.17 shows a photograph of the developed device. The material of the box is black acrylonitrile butadiene styrene (ABS) with dimensions around 85 mm × 70 mm × 49 mm and it weighs 128 grams. The system was powered using a standard 9 V battery.

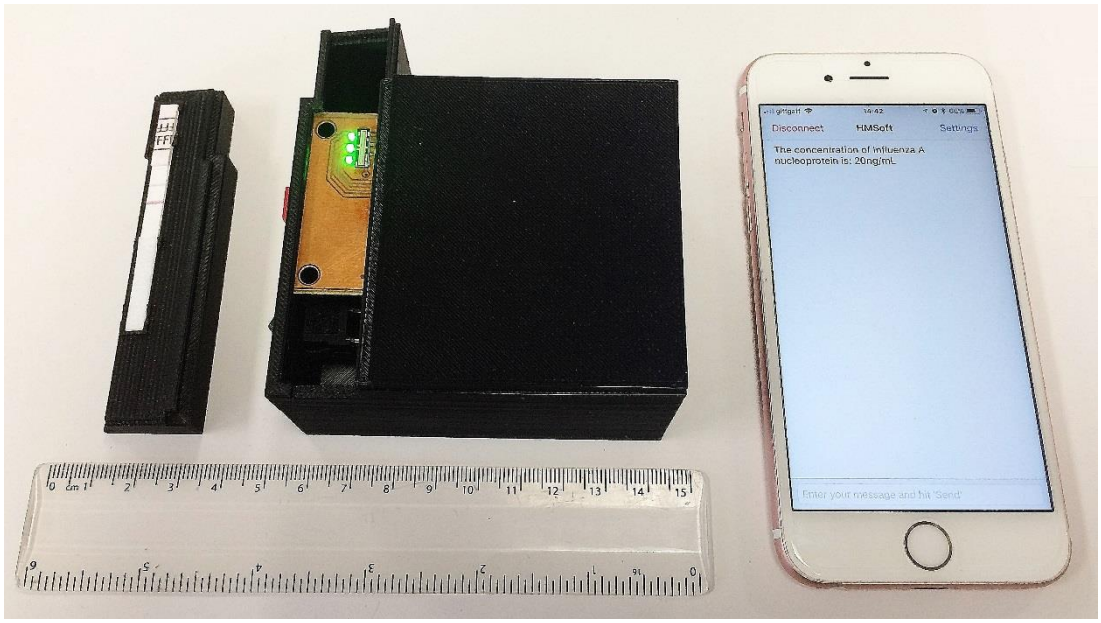

Figure 3.17 Photograph of the device. The lid is open, showing the carrier where the LFIA is placed fixed in the appropriate position.

3.5.1 TEST WITH FLU A LFIAS AND RESULTS

The performance of the device has been experimentally evaluated using test strips from BD Directigen in the concentrations range of 0.5ng/mL to 200ng/mL of Influenza A nucleoprotein in saline buffer as shown in Figure 3.18. Each strip was measured 10

times to check the reproducibility of the reader and the average signal from each strip was calculated. Figure 3.19 (a) shows the average calculated signal from a test strip with 20 ng/mL concentration. The net signal from the analyte was estimated from the results using the background correction method [67]. This performed by subtracting the signal of a blank strip (no lines, only saline buffer in the sample) from the average calculated signal. Figure 3.19 (b) shows the calculated signal for the strip of 20 ng/mL concentration after the background correction. Due to implementation of this correction, the data reversed compared to measured data from the device and the maximum values represents the signal from the test and control lines. From the derived signals, as in the first device the maximum value was detected for the first 20 to 50 pixels (124 pixels scan 8 mm) of each strip and then the average value of this maximum and the maxima of the ± 4 adjacent pixels calculated. The calculated value corresponds to the signal of the test line (S_T). The overall average value of 9 pixels was used because it is the number of pixels that approximately collect most of the reflected light from the test line. The same procedure was performed for the calculation of the signal of control line (S_C), but the maximum was this time scanned between the corresponding pixels 90 to 120. The ratio S_T/S_C was calculated for all the LFIAs shown in Figure 3.20.

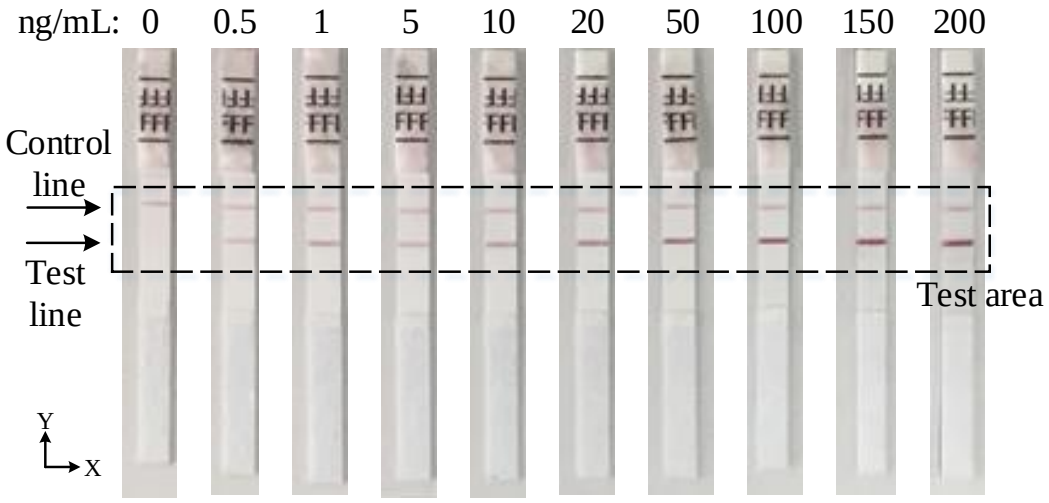

Figure 3.18 Photograph of the LFIA strips in various concentrations that have been used for the testing of the system.

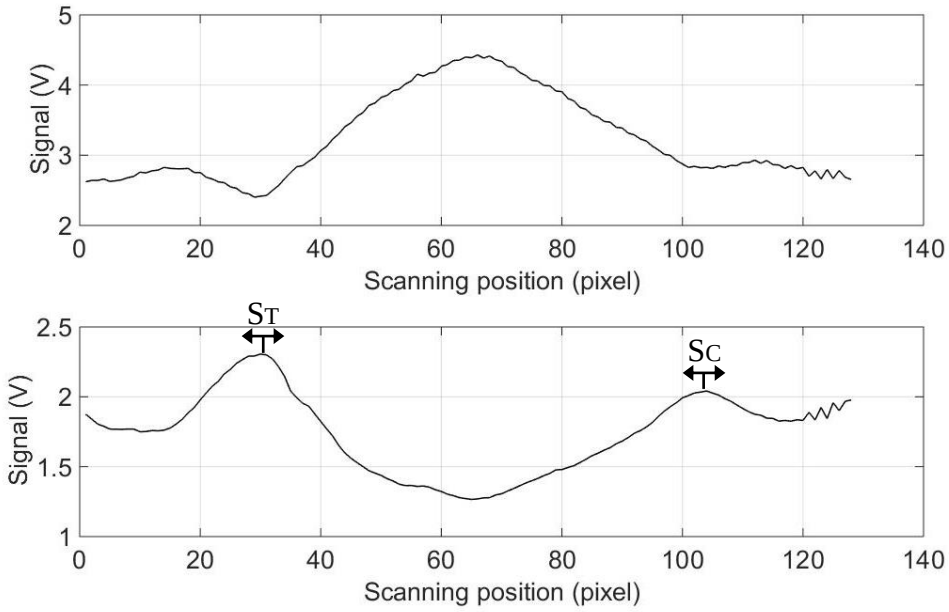

Figure 3.19 Lateral flow immunoassay with 20 ng/mL concentration of Influenza A nucleoprotein (a) voltage output of the 8 mm 128 photodiode chip; (b) Voltage output signal after the implementation of background correction using a blank strip showing positions of S_T and S_C.

This second generation system has further reduced the effect of line positioning variation. This is because the special carrier with small clips (Figure 3.17) ensures that the strip is always placed in the device in the right position, more than the proof of concept system with the slide-in slot design. In addition, the automatic detection of the test and control lines eliminates any errors due to variations in the position of the lines [32].

The 4PL model was used for the generation of the fitted curve as shown in Figure 3.20, with the measured signal being the S_T / S_C after background correction. The coefficient of determination is R^2 = 0.974 and the calculated parameters of Equation 3.1 are a = 0.97, b = 1.16, c = 32.95, and d = 1.33.

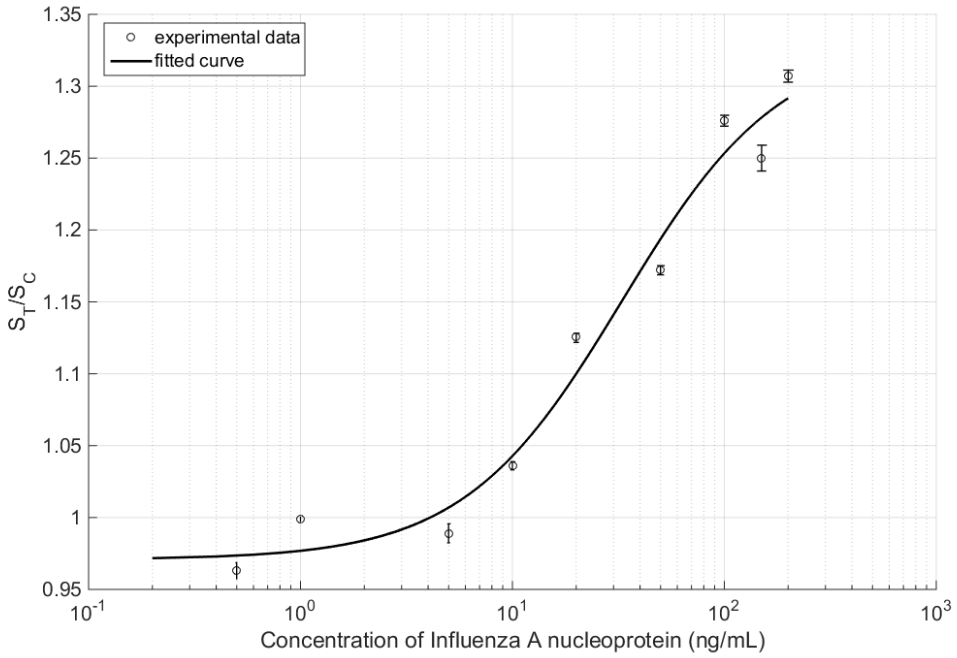

Figure 3.20 The fitted curve of S_T/S_C for various concentrations of Influenza A nucleoprotein based on the 4PL model. The error bars indicate the ±2σ limits.

It should be noted that even though the construction of the calibration curve was realized using the ratio of the signals S_T / S_C for each strip, this method is not always applicable for different types of LFIA / analyte. This is the case when the response of the control line varies with the analyte concentration and therefore, only the signal from the test line is needed for the construction of calibration curve.

The value of the cut-off signal was calculated using a sample with no concentration of analyte of interest (0 ng/mL, only control line). The strip with this sample has been tested 10 times with the mean signal value being S_T / S_C = 0.704 and the standard deviation σ = 0.0058. Therefore, the cut-off value that defines when the analyte of interest is not present in the sample is calculated as S_T / S_C + 3σ = 0.7214.

Comparing the first generation system with the second generation system it is evident that the system has been improved in many aspects through the optimization process. The power consumption is reduced by 62.5% simply from decreasing the required number of LEDs. In addition, the limit of detection improved from 3 ng/mL to 0.5 ng/mL. Table 3.1 summarizes the features and performances of the two devices.

Parameters	First generation system	Second generation system
Detection limit	3 ng/mL	0.5 ng/mL
Size	110 mm × 80 mm × 45 mm	85 mm × 70 mm × 49 mm
Weight	200 g	128 g
Number of LEDs	8	3
LEDs wavelength	White	525 nm (green)
LFIA position	On top of the detector	10 degrees tilt from the detector

Table 3.1. Features and performances of the first and second generation reader systems.

3.5.2 TEST WITH SURFACE-LAYER PROTEIN A LFIAS AND RESULTS

In addition to Influenza A nucleoprotein, the second generation system was also tested with Surface-layer protein A (SlpA) LFIAs. The aim of this test was to demonstrate that the proposed device can quantify the results in LFIA strips for a variety of analytes.

The *Clostridium difficile* (*C. difficile*) is a bacterium that naturally exists in the human gut. However, the use of antibiotics often results in the disturbance of the natural flora of the gut with subsequent multiplication of the *C.difficile* and colonization. This leads to the release of toxins that are responsible for the clinical symptoms of the Clostridium difficile infection [68]. The main symptoms of this infection are diarrhoea, blood in stools and high body temperature. Even though most of the infected patients recover with treatment, in old patients and people with weak immune system this infection can be fatal [69]. It is estimated that tens of thousands of people die from this infection worldwide every year [70].

The surface layer (S-layer) is the outer layer of the bacterial cell. In the S-layer of *C.difficile* cells, the SlpA is the most plentiful protein. This protein has a significant role among others in the cell adherence and the colonization process [71]. The tested

strips detect the presence of SlpA in the sample and generate a color test line based on sandwich format similar to Influenza A nucleoprotein strips.

Figure 3.21 shows the tested strips in various concentrations of SlpA. The tests were performed using the second generation device, which was slightly modified such that the special carrier with small clips where the strip is placed matched the new size of the tested strips, so that their test line could be placed on top of the array of photodiodes. The gold nanoparticles in the SlpA strips have 40ng diameter, which still has highest light absorption in green wavelengths and therefore, the rest of system remained unchanged.

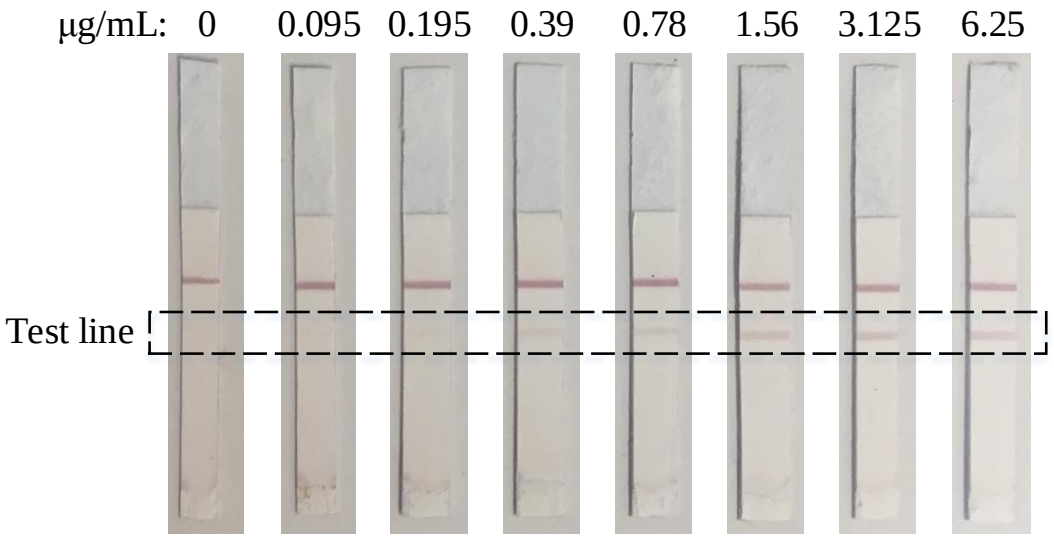

Figure 3.21 Photograph of the LFIA strips in various concentrations of SlpA.

The signal from the test line only was used in the calculations. This is because the signal from the control line is changing for different analyte concentrations. Similarly to the previous investigations, the background correction was performed first. Then the signal from the test line was automatically detected and compared with the background of the strip in order to calculate the S_T signal. Figure 3.22 shows the calibration curve of the system when measuring LFIAs with SlpA and using the 4PL model to generate the fitted curve. The coefficient of determination is $R^2 = 0.979$ and the calculated parameters of Equation 3.1 are $a = 9.01$, $b = 0.95$, $c = 2.32$, and $d = 59.14$.

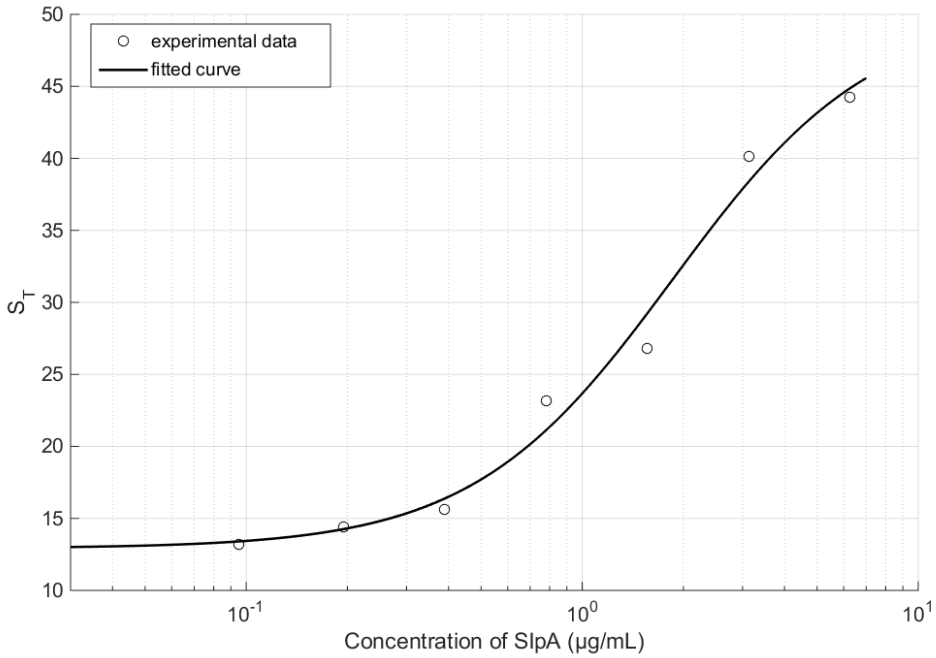

Figure 3.22 The fitted curve of S_T for various concentrations of SlpA based on the 4PL model.

3.6 DISCUSSION

Based on the analysis performed in chapter 2 it is evident that there is great demand for POC readers for quantification of the analyte in LFIAs and with particular specifications namely low cost, low power, high robustness, high reproducibility and low positioning error. In this chapter, two systems that fulfil these specifications were developed and implemented using discrete components. The first system is a proof of concept system, in which the scanning method was implemented without using any moving parts and any extra optical accessories. Therefore, the proposed system design remained robust, low cost and any positioning errors were avoided. The system was tested with LFIAs with Influenza A nucleoprotein and demonstrated quantification capabilities with limit of detection at 3ng/mL.

This first generation system was subsequently optimised, leading to the development of an improved second generation system. For the optimization, a numerical BSDF model that describes the LFIA's surface response in incident light

was firstly developed using experimental measurements from the imaging sphere. The BSDF model was then imported in a ray trace simulation program along with the models of all the critical components, and simulations were performed. The aim was to define the optimum position of these components in order to achieve uniform light distribution across the surface of LFIA and therefore, increase the system's sensitivity with a minimum required number of LEDs. Based on these simulation results the second generation system was developed. The wavelength of the LEDs used in this system was modified in order to match the maximum light absorption from the gold nanoparticles present in the tested LFIAs. A 3D printed enclosure was designed to protect the system from ambient light and to ensure that the tested strips were placed in the right position. The system was tested with Influenza A nucleoprotein and SlpA LFIA strips. As shown, the reader device can detect samples with concentrations of Influenza A nucleoprotein as low as 0.5 ng/mL, which is much less than the detection limit of the device in proof of concept system. In addition, the decrease of the number of LEDs led to a corresponding 62.5% reduction in power consumption.

3.7 CONCLUSION

In this chapter, the design implementation and performance of the first and second generation reader systems for LFIAs is presented. From the study performed and the obtained results the following conclusions can be drawn:

- The scanning method can be achieved without the use of moving parts, but just with the use of a sufficient size of an array of photodiodes. In this way any positioning errors are minimized.
- A reader can be implemented without the use of any lenses and other optical accessories and with the ability to detect the test line, if the sample under detection and the light source are in close proximity to the photodetector (array of photodiode).
- A tilt of the LFIA at 10 degrees can give better results than at 0 degree tilt in the proposed setup.

- Ray trace simulations are very important in reader system design. The second generation system was improved with respect to the limit of detections and power consumption.
- The specification of gold nanoparticles present in the tested LFIA should be taken into consideration when designing a readout device.

4

CIRCUIT DESIGN OF A CMOS IMAGE SENSOR ASIC

CISs are widely adopted in many electronic devices for variety of purposes such as recording, pleasure, exploration and medicine. A decisive factor in this trend were the advances in CIS circuit design and fabrication techniques leading to high quality images. The development of ASIC CIS to satisfy the properties of the application is a challenging process. According to author's best knowledge all the image sensors used so far in readout devices for LFIAs have never been designed specifically for this application. Therefore, they lack optimization in terms of power consumption, number of pixels and noise performance.

In chapter 4 the circuit design of a CIS ASIC is introduced. The design of the chip is based on the requirements of a point-of-care reader for LFIAs. A comparison between the two types of image sensors which are frequently used is presented. The basic principles of operation of photodiodes are explained, followed by the overview of most common existing CIS pixel topologies. The circuit specifications of the proposed CIS are presented and detailed analysis and simulation results of the proposed CIS circuit architecture is performed. Finally, the layout of the overall chip is presented.

4.1 IMAGE SENSORS

Image sensors convert the light wave information into voltage or current signals. These can then be converted into an image as viewed by the sensor. The image sensors that are currently widely used are the charge coupled device (CCD) and the active pixel CMOS image sensor (CIS).

CCD sensors contain an array of pixels which have metal-oxide semiconductor (MOS) capacitors as photodetector elements [72]. When photons hit the photosensitive area charge packets of electrons are produced [73]. As shown in Figure 4.1 (a) the charge packets are shifted to the end of a column where they are sequentially read using an output preamplifier [72].

Active Pixel CISs consists of an array of pixels, as shown in Figure 4.1 (b) in which each pixel has a photodiode and electronics for integration of the photocurrent. Column and row circuits shift the pixels' output signals for further processing at the end of each column and then out of the sensor.

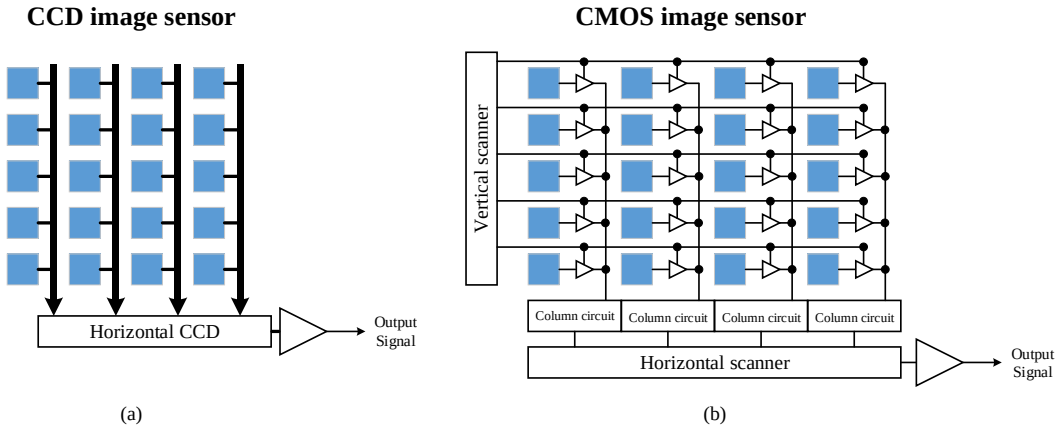

Figure 4.1 Schematic diagram of (a) CCD image sensor and (b) CMOS image sensor architecture.

Charge Coupled Devices (CCDs) have been for many years the first choice in the image sensor market. However, with the improvement in fabrication techniques and circuit designs, the CMOS image sensors have been successfully competing in some areas the CCDs. The main advantage of CISs are the low power consumption, the low cost, compatibility with standard CMOS technology that can lead to complete integrated systems, random access of data and high speed. On the other hand CCDs

are still superior in comparison to CISs in the areas of noise, dynamic range and sensitivity due to the Fill Factor [74]. In the proposed reader for LFIAs the CIS has been considered as the most appropriate technology for the implementation of the image sensor, because it offers advantages important for point-of-care applications and its noise performance has been improved using noise cancellation techniques.

4.2 PRINCIPLE OF OPERATION OF PHOTODIODES

The most common photosensitive element in CIS is the photodiode (PN junction). For the photodiode to operate as a photosensitive element it must operate in its third quadrant of *I-V* characteristics [75]. If the photodiode is illuminated with a photons that have energy higher than the bandgap energy of the material, $hv = hc/\lambda > E_g$, the covalent bonds are destroyed, liberating electrons and creating holes. This is known as photogeneration process and its probability of occurrence is related to the absorption coefficient of the material, a, while the photogeneration process is more intense in the surface of the material [76]. Given that the E_g of silicon is 1.12 eV, almost all the spectrum of solar radiation can perform the photogeneration process in the silicon.

When photo-generated carriers are generated within the depletion region (*W)* of the diode, the existing electric field drifts them towards the respective majority carrier region (electrons are collected in the n region and holes are collected in the p region), creating the photocurrent that flows from n-side towards the p-side. The photons can also generate minority carriers (electrons and holes) in the neutral N-type and P-type regions. If these carriers diffuse to the depletion region they contribute to the photocurrent [77]. The resulting photocurrent, I_{ph}, due to all optically generated carriers is:

$$I_{ph} = qAG_{ext}(W + L_n + L_p) \tag{4.1}$$

Where q is the electron charge, A is the total area of the junction including the bottom and sidewalls, the generation rate G_{ext} is the number of electron-hole pairs generated in a unit of the depletion-layer volume per second, L_n and L_p are the depletion electron diffusion length and hole diffusion length respectively, W is the depletion region width and is [75]:

$$W = \sqrt{\frac{2\epsilon(V_0 - V_R)}{q}\left(\frac{N_a + N_d}{N_a N_d}\right)} \tag{4.2}$$

Where ϵ is the silicon permittivity, N_a and N_d the doping concentration of the p and n type materials respectively, V_R the applied voltage and V_0 the built-in diode potential [78]:

$$V_0 = \frac{kT}{q}\ln\frac{N_a N_d}{n_i^2} \tag{4.3}$$

Where n_i is the intrinsic carrier concentration of silicon, k is the Boltzmann constant and T the absolute temperature.

The sensitivity of a photodiode depends on the depletion region width. Therefore in order to achieve maximum width the doping levels in the PN junction should be as low as low as the fabrication technology allows [77]. In the case of symmetrically doped junction the junction capacitance is described as in Equation 4.4 [75]:

$$C_j = \epsilon A\left[\frac{q}{2\epsilon(V_0 - V_R)}\frac{N_d N_a}{N_d + N_a}\right]^{1/2} = \frac{\epsilon A}{W} \tag{4.4}$$

The *I-V* characteristic of the photodiode changes as a result of the photocurrent, as in Equation 4.5 and shown in Figure 4.2.

$$I = I_s\left[exp\left(\frac{qV}{kT}\right) - 1\right] - I_{ph} \tag{4.5}$$

Where I_s is the saturation current of the photodiode (or reverse bias diffusion current) and V the anode to cathode bias voltage.

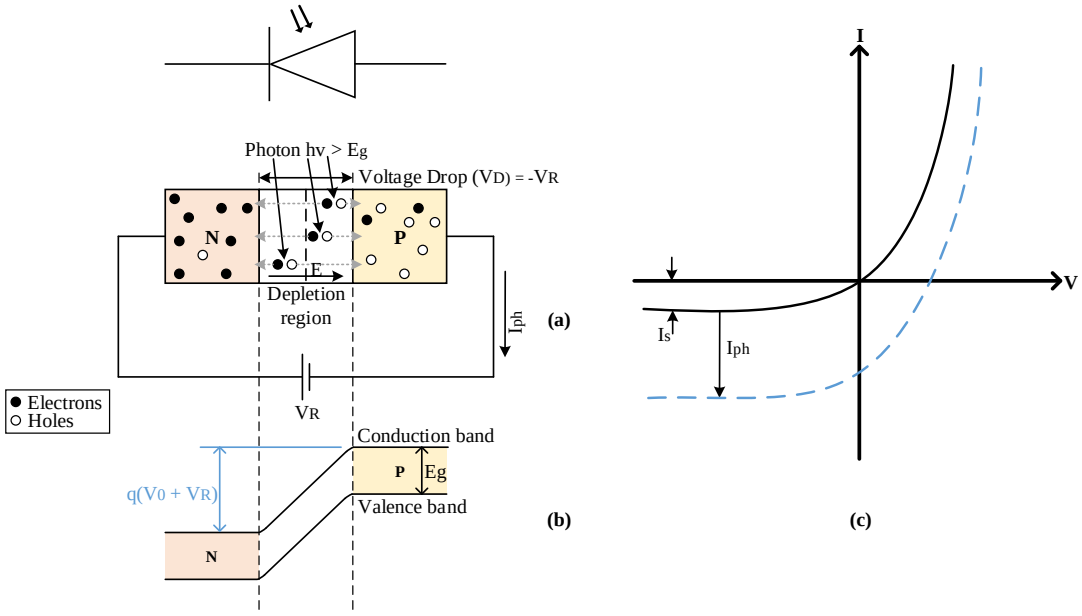

Figure 4.2 (a) Cross section of reverse biased photodiode, (b) its energy band diagram. (c) I-V characteristics of an illuminated PN junction (dashed line).

4.2.1 BASIC PHOTODIODE CONFIGURATIONS

Three basic photodiode configurations that are commonly found in a standard CMOS process, the n+/p-sub, the n-well/p-sub and the p+/n-well/p-sub, as shown in Figure 4.3.

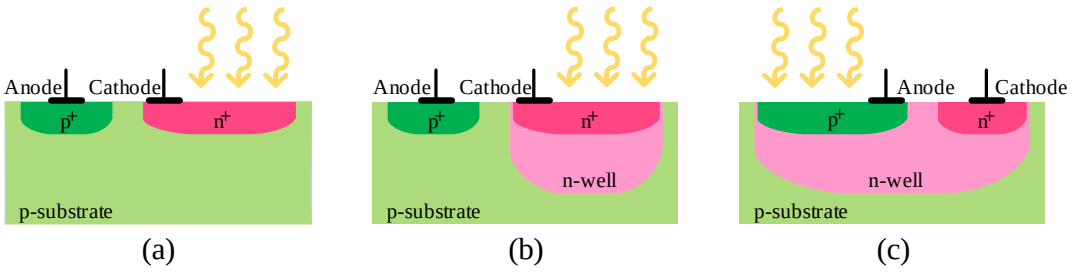

Figure 4.3 Schematic representation of the three photodiodes (a) n+/p-sub, (b) n-well/p-sub and (c) p+/n-well/p-sub [79].

The n+/p-sub photodiode is fabricated from the n+ doped area in a p-substrate. It occupies small area based on the minimum technology spacing and width compared to other photodiodes. Because of the high doping concentrations it has small depletion region width. This results in low collection efficiency due to its shallow junction,

which results in the loss of those photo-generated carriers which are generated deeper in the material, particularly at longer wavelengths. Also due to small depletion region width the junction capacitance is high [78].

The n-well/p-sub photodiode has the junction made of lightly doped n-well area in a p-substrate. It occupies larger area than the n+/p-sub photodiode and due to low doping concentration it has large depletion region width. This leads to higher collection efficiency and low junction capacitance [78].

The p+/n-well/p-sub photodiode is also called “pinned" photodiode and has one extra p+ doped area in an n-well/p-sub photodiode. This photodiode occupies the largest area of the three photodiodes. The two junctions result in the larger depletion region width and therefore it has the highest collection efficiency. The two junction capacitors are added in parallel resulting in an overall higher junction capacitance compared to the other photodiodes [79].

4.3 OVERVIEW OF EXISTING CMOS PIXEL TOPOLOGIES

The generated photocurrent from the photodiode is usually small and therefore its direct measurement is very difficult. For this reason most of the CIS architectures are based on an integration procedure [80]. In this approach, the photodiode is set to a known voltage controlled by closing a reset switch. After the reset switch is opened and the photocurrent is integrated in a capacitor.

The signal conversion stages of a CIS are shown in Figure 4.4 [80]. Photons impinging in the photodiode, convert into photocurrent according to Quantum Efficiency (QE) factor. This factor indicates the portion of the impinging photons that contributes to photocurrent, which always is smaller than 1. The QE is mainly affected by the wavelength, the doping concentrations, the fill factor and the photodiode geometry. The photocurrent is then integrated in a capacitor (C_{int}) and converted into voltage, based on the conversion gain, C_{gain}, where:

$$C_{gain} = \frac{q}{C_{int}} \ (\mu V/e^{-}) \tag{4.6}$$

The conversion gain is defined as the output voltage generated by one electron at the integration capacitor [81].

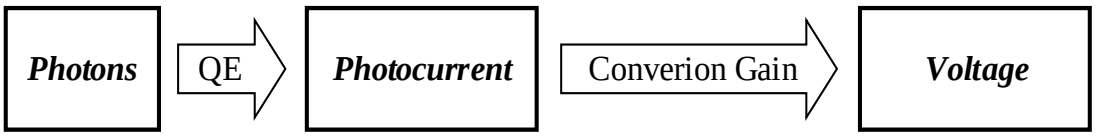

Figure 4.4 Block diagram of the signal conversion at the different stages of a CIS [80].

The most common pixel architectures used in CIS designs are the 3T-APS (3-transistor active pixel sensor), the 4T-APS (4-transistor active pixel sensor) and the CTIA (capacitive transimpedance amplifier).

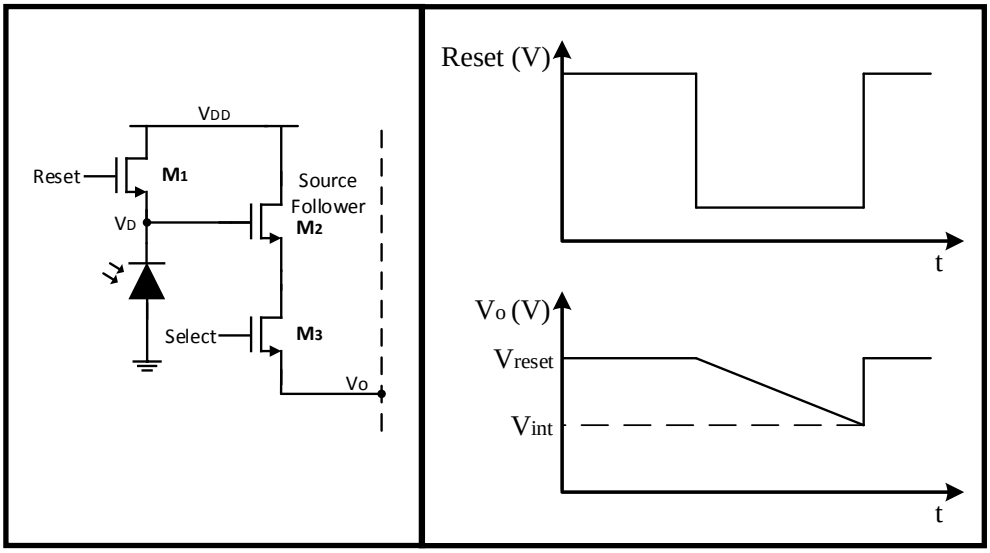

Figure 4.5 Circuit of conventional 3T-APS pixel architectures and timing diagram of the reset switch and the transient response of the output voltage.

The 3T-APS is the simplest architecture, as shown in Figure 4.5. M_1 is the reset transistor which controls the integration time, M_2 is the source follower transistor which acts as a buffer amplifier and M_3 is the readout switch transistor [72]. Initially the M_1 is closed and the photodiode is connected to the power supply charging the photodiode capacitor to a high voltage (it should be noted that all the switches used in

this thesis are active high). Then M_1 opens and the photocurrent starts to discharge the capacitance at a constant integration time [78] as shown in Figure 4.5 and Equation 4.7.

$$V_o = \frac{1}{C_{ph}} \int I_{ph} dt \tag{4.7}$$

The access of the pixels is performed through M_2 and M_3. Although this architecture has simple implementation and high fill factor, it has low sensitivity. This is because the photocurrent is integrated on the capacitor of the photodiode which has large capacitance [37].

The 4T-APS architecture uses 4 transistors as shown in Figure 4.6. As with the 3T-APS it has a reset transistor M_2, a source follower transistor M_3, a readout switch transistor M_4 and an extra transistor M_1 to decouple the floating diffusion node (V_{DF}) from the photodiode and therefore separate the read and reset operation from the integration phase [82] [83]. In this way the correlated double sampling (CDS) technique can be implemented in order to remove the reset noise.

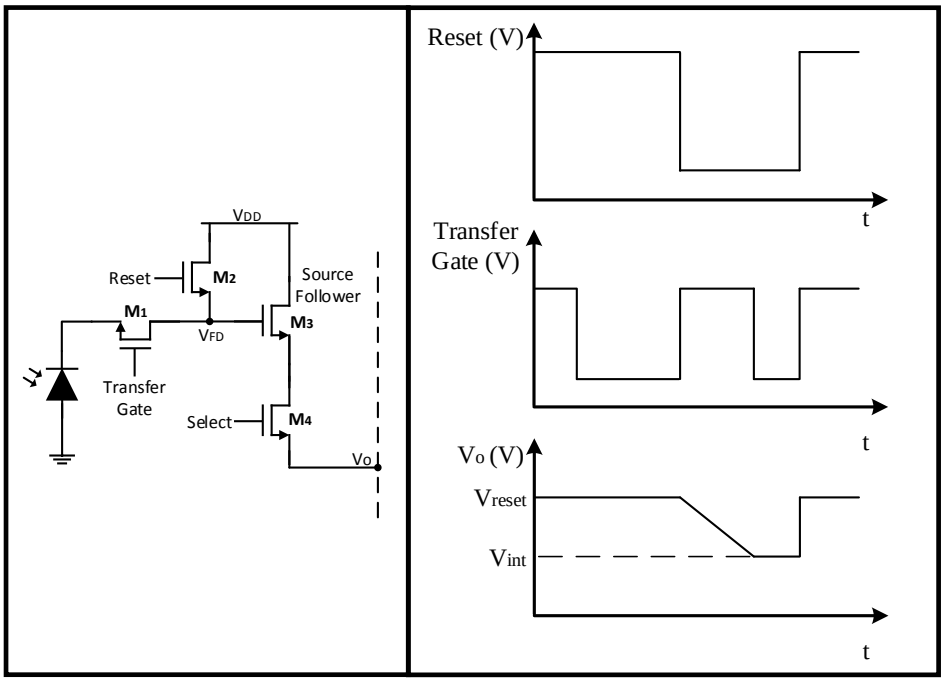

Figure 4.6 Circuits of conventional 4T-APS pixel architectures and timing diagram of the reset switch, transfer gate switch and the transient response of the output voltage.

Initially the M_1 and M_2 are closed removing any remaining electrons in the photodiode. Then the transfer gate opens decoupling the photodiode from the floating diffusion node which stays in its reset condition. In the photodiode the accumulation of photo-generated charges begins. Then the reset transistor opens and the transfer gate closes. The charges from the photodiode are transferred into the floating diffusion node (V_{FD}) [82]. Because the charge to voltage conversion is performed at the floating diffusion node capacitance, it has small capacitance value so sensitivity is high [84] [83]. Finally the transfer gate opens and the pixel output voltage signal is related to the power intensity of light impinging in the photodiode over the integration time [82]. In CDS this output signal is subtracted from the reset output signal.

Despite the advantages this architecture has in low light illumination it generates delayed images because of the slow charge transfer from the photodiode to the floating diffusion capacitance. In order to overcome this the pinned photodiodes can be used. The size of the transfer gate and floating diffusion capacitance can also be increased for high speed imagers. However larger parasitic capacitors at the floating diffusion node results in reduced sensitivity [37], [83].

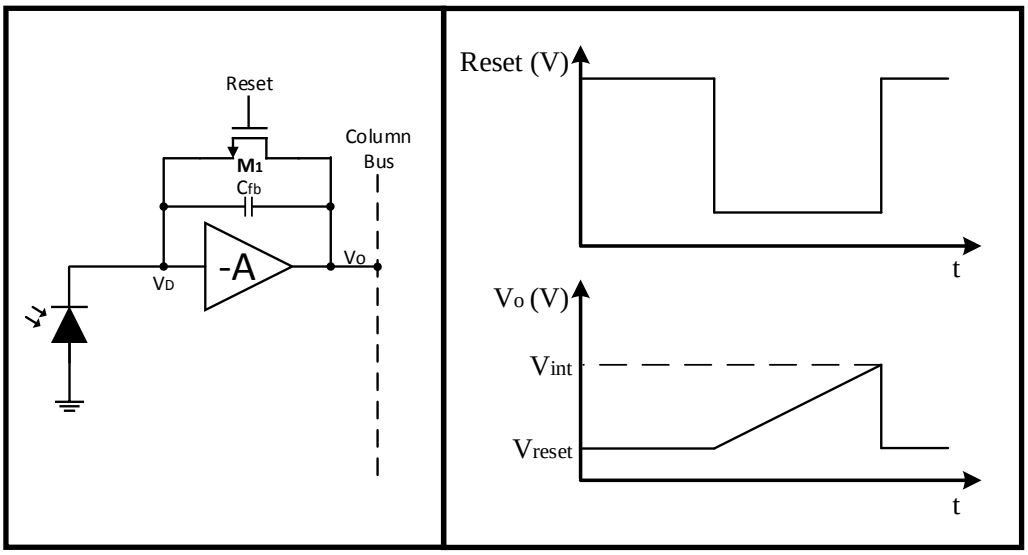

Figure 4.7 Circuits of conventional CTIA-APS pixel architectures and timing diagram of the reset switch and transient response of the output voltage.

The CTIA architecture has an amplifier with a capacitor and a reset switch in a negative feedback as shown in Figure 4.7. When the reset switch closes, the inverse output of the amplifier defines the reverse bias across the photodiode and the

photodiode capacitance is charged to that voltage level (V_D) [78], [85]. Then the reset switch opens and the photocurrent is integrated through the negative feedback capacitor. According to Miller effect there will be an increase in the equivalent input capacitance of the inverting voltage amplifier resulting in an input Miller capacitance ($C_M = C(1 + A)$) parallel to the photodiode capacitance (C_{ph}). Figure 4.7 shows the CTIA-APS architecture and its transient output voltage. Due to the inverse characteristics of the amplifier the output voltage in the CTIA architecture increases [78]. The input voltage change is:

$$\frac{dV_{in}}{dt} = -\frac{I_{ph}}{C_{ph} + (A+1)C_{fb}} \tag{4.8}$$

Where C_{ph} is the photodiode capacitance and I_{ph} is the photocurrent.

The output voltage is:

$$V_{out} = -AV_{in} \tag{4.9}$$

From Equations 4.8 and 4.9:

$$\frac{dV_{out}}{dt} = -A\frac{dV_{in}}{dt} = \frac{AI_{ph}}{C_{ph} + (A+1)C_{fb}} \tag{4.10}$$

For $(A + 1)C_{fb} \gg C_{ph}$ and $A \gg 1$, the output of the CTIA topology (4.10) simplifies to:.

$$\frac{dV_{out}}{dt} \approx \frac{I_{ph}}{C_{fb}} \rightarrow V_{out} = \frac{1}{C_{fb}}\int I_{ph}dt \tag{4.11}$$

4.4 SYSTEM SPECIFICATIONS

The developed CIS is required to have low power consumption so that it can perform many readings from a single battery, and have low noise and good Signal-to-noise ratio (SNR) performance in order to distinguish accurately the different concentrations of LFIA even when the test line is faint. Given that no lenses will be

used when reading the paper strip in Figure 4.8 the required number of pixels should be sufficient to cover the test line area lengthwise plus leaving some extra space around the test line in case that the strip is slightly moved during the insertion in the reader case, as shown in Figure 4.8. The strip can be up to 5 mm wide however no more than 1 – 4 rows are required for the measurements. As the results from the first and second generation system showed, even with one row of pixels quality readings can be measured. Therefore the proposed system was chosen to have 4 × 64 pixel with binning capabilities. The photocurrent to voltage conversion is performed using compact pixel architecture that combines the CTIA topology with noise cancelation techniques reusing the same amplifier for reduced power consumption.

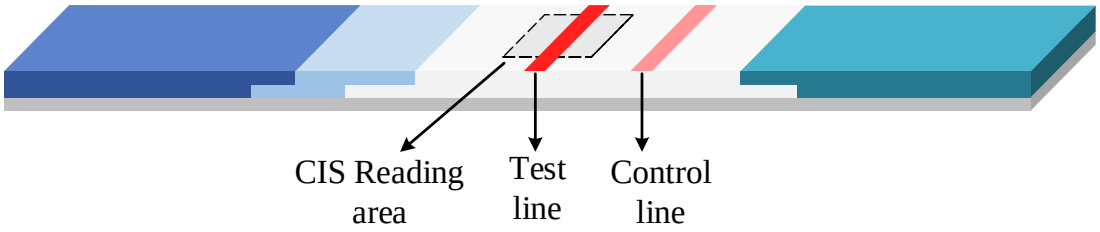

Figure 4.8 Schematic of lateral flow immunoassay. The dashed box indicates the area of interest where the CIS will be used for measurements.

The design technology used is AMS 0.35 μm and the photodiodes are n - well/p - substrate with anti-reflecting coating. This extra layer was used to attenuate the reflections on top of the photodiode and thus increases its photosensitivity. The photodiode has responsivity 0.29 A/W at 550 nm, which is in the range of wavelengths of interest. The chosen photodiode size is 20 μm × 20 μm which is a good trade-off between the active area and the circuit area in the pixel. Furthermore, given that the CIS does not require to have high resolution but to be able to collect more photons, there was no need to have very small photodiode size.

The photocurrent range that is required for the system to operate was calculated using the setup of the first generation system but in the position of the array of photodiodes a power meter was placed. Therefore when the LFIA was inserted into the system the power meter measured the light impinging into its surface, which is in the range of approximately 5 $\mu W/cm^2$ – 50 $\mu W/cm^2$. Then using these values the photocurrent was calculated as shown in Equations 4.12 and 4.13.

$$I_{ph} = R \cdot P \rightarrow I_{ph} = \frac{0.29A}{W} \cdot \frac{5\mu W}{cm^2} \rightarrow I_{ph} = \frac{1.45\mu A}{cm^2} = 0.0145\ A/m^2 \quad (4.12)$$

$$I_{ph} = R \cdot P \rightarrow I_{ph} = \frac{0.29A}{W} \cdot \frac{50\mu W}{cm^2} \rightarrow I_{ph} = \frac{14.5\mu A}{cm^2} = 0.145\ A/m^2 \quad (4.13)$$

Where I_{ph} the photocurrent (in A/cm^2), R is the photodiode responsivity (in A/W) at a specific wavelength and P is the incident optical power (in W/cm^2) [81].

Given that the photodiode size is 20 µm × 20 µm the expected photocurrent generated is 5.8 pA to 58 pA. The feedback capacitor for each CTIA was chosen to be 10 fF which is a trade-off between the conversion gain Equation 4.6 and 4.14 and the reset noise Equation 4.15 due to reset switch. In the proposed design the integration capacitor is the feedback capacitor. Table (4.1) summarises the design specification parameters.

$$C_{gain} = \frac{q}{C_{fb}} = \frac{1.6 \cdot 10^{-19}}{10 \cdot 10^{-15}} = 16\mu V/e^- \quad (4.14)$$

$$\langle n_{reset} \rangle = \sqrt{\frac{kT}{C_{fb}}} = 0.64mV_{rms} \approx 40e^- \quad (4.15)$$

Specifications	Value
Current range	5.8 pA – 58 pA
Photodiode capacitor	70 fF
Feedback capacitor	10 fF
Integration time	> 17 µs, < 2.6 ms

Table 4.1. Design specification parameters.

4.5 SYSTEM ARCHITECTURE

The architecture of the proposed CIS is shown in Figure 4.9. It comprises 4 × 64 pixels and each pixel consists of a 20 μm × 20 μm photodiode with two logic gates and two switches to enable the column and row selection. The generated photocurrent in each pixel is transferred to its respective column processing circuit. There is only one processing circuit per column, and all 4 photodiodes of the same column share the same processing circuit. In this way the binning technique can also be implemented. In this technique 2 or 4 pixels of the same column are enabled at the same time sending their sum photocurrent for processing simultaneously. The column selection is controlled from a shift register with 64 outputs that are connected to 64 3 - bit counters which generate the signals to control various gates. The row selection is controlled externally with 4 digital signals.

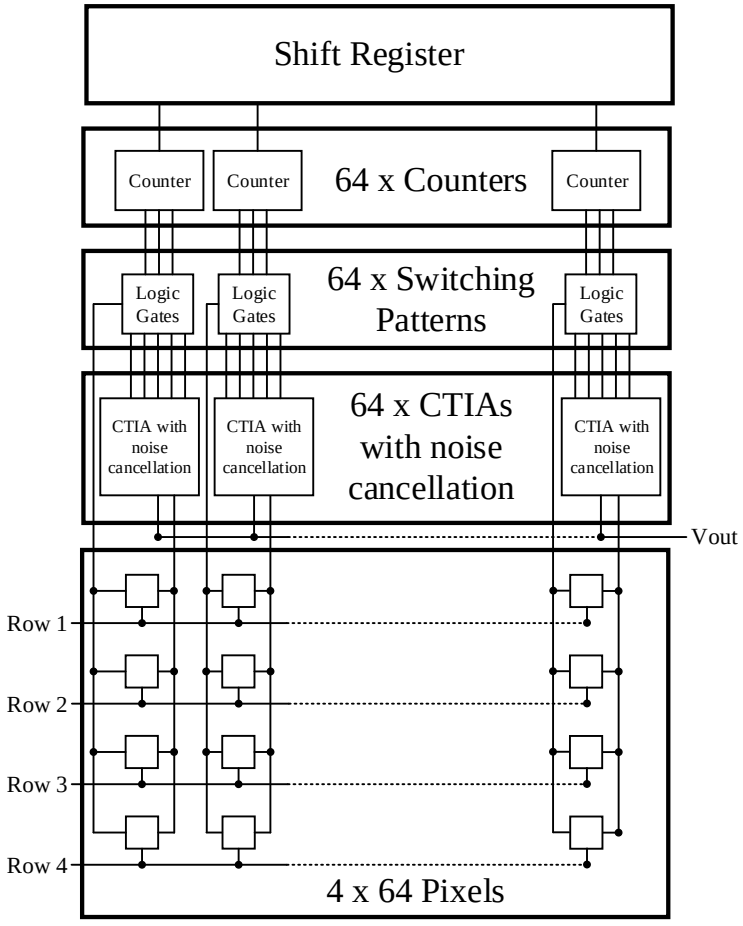

Figure 4.9 System diagram of the CIS chip

4.6 PROPOSED COMPACT CTIA WITH NOISE CANCELLATION CIRCUIT ARCHITECTURE

In the proposed design the photocurrent to voltage conversion is performed using compact processing circuit architecture that combines the CTIA topology with noise cancelation. The CTIA topology was chosen because:

- The sensitivity can be increased by decreasing the feedback capacitor and also by increasing the photodiode size area.
- The voltage at the junction capacitance is kept constant and therefore the depletion region is kept constant.
- The drawback of reduced fill factor does not affect this design. This is because only 4 rows of pixels are required and therefore the processing circuit can be shared between them outside the pixel area.

4.6.1 CTIA ARCHITECTURE

The amplifier of the CTIA architecture is the main component in the photocurrent processing design and must satisfy some specific requirements: a high open loop gain is required for stability of the input biasing point and therefore linear response to incident photons [85], low input referred noise is needed in order to achieve low temporal noise of the CIS [86], and the amplifier must have low power consumption because in total 64 amplifiers are required, one for every column.

The implemented amplifier is a single input, single output cascode common source amplifier, operating in weak inversion with bias current of 10 nA and 3.3 V power supply as shown in Figure 4.10.

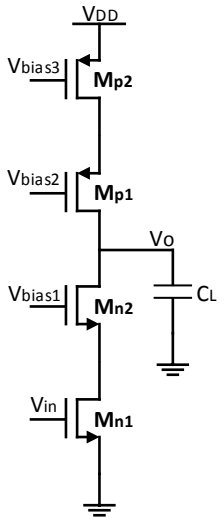

Figure 4.10 Single input single output cascode common source amplifier

The voltage gain is:

$$A_V = \frac{V_o}{V_{in}} = g_{m1}\left[R_{on}//R_{op}\right] = g_{m1}[(g_{m2}r_{o1}r_{o2})//(g_{m3}r_{o3}r_{o4})] \tag{4.16}$$

Where $R_{out} = R_{on}//R_{op}$ and $R_{on} = gm_2r_{o1}r_{o2}$, $R_{op} = gm_3r_{03}r_{o4}$.

The Gain-Bandwidth product is:

$$GBW = \frac{g_{m1}}{2\pi C_L} \tag{4.17}$$

The design parameters of the cascode common source amplifier are listed in Table 4.2. For the simulations the load $C_L = 200fF$. The resultant voltage gain A_V is 105.4 dB and the *GBW* is 219.66 KHz .The bias voltages V_{bias1}, V_{bias2}, V_{bias3} were generated on-chip using a cascode current mirror as shown in Figure 4.11.

Parameter	Value
V_{DD} (V)	3.3
I (nA)	10
V_{bias1} (V)	1.4
V_{bias2} (V)	2.1
V_{bias3} (V)	2.7
$\left(\frac{W\ (\mu m)}{L\ (\mu m)}\right)_{Mn1}$	$\left(\frac{9.6}{4}\right)$
$\left(\frac{W\ (\mu m)}{L\ (\mu m)}\right)_{Mn2}$	$\left(\frac{3.5}{1}\right)$
$\left(\frac{W\ (\mu m)}{L\ (\mu m)}\right)_{Mp1}$	$\left(\frac{14}{2}\right)$
$\left(\frac{W\ (\mu m)}{L\ (\mu m)}\right)_{Mp2}$	$\left(\frac{14}{2}\right)$

Table 4.2. Design parameters of the cascode common source amplifier

The photodiode was simulated using a current source in parallel to a capacitor that has capacitance equivalent to the photodiode's expected capacitance. [85]. The simulated parameters of the cascade common source amplifier are shown in Table 4.3. In a MOS transistor, the flicker noise (1/f noise) is inversely dependent on the *WL* size while the thermal noise is directly dependent on transconductance *gm*. The output-referred noise is equal to input-referred noise multiplied by the voltage gain.

Specifications	Value
A_v	105 dB
GBW	220 KHz
Input-referred Noise (flicker)	2.38 $\mu V/\sqrt{Hz}$ at 1Hz
Input-referred Noise (thermal)	624 $nV/\sqrt{Hz}$ at 10KHz
Power Consumption	98.24 nW

Table 4.3. Simulated parameters of the cascode common source amplifier.

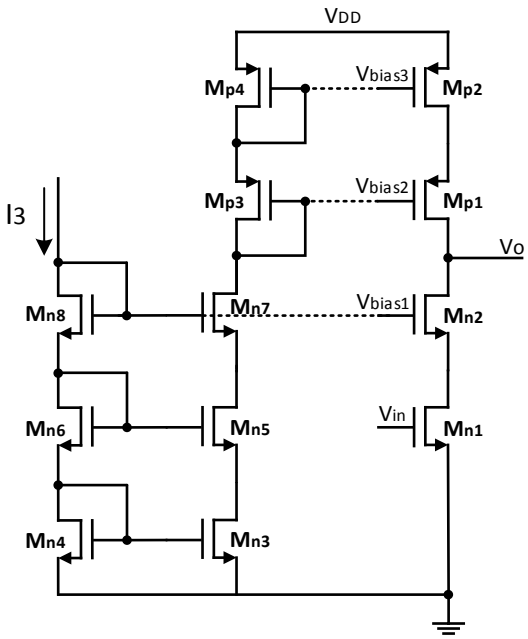

Figure 4.11 Cascode current mirror connected a cascode common source amplifier.

The output voltage swing of the system in Figure 4.11 was measured in simulations and is in the range of 12.73 mV – 3.28 V, as shown in Figure 4.12. This is because the transistors are biased in subthreshold. Table 4.4 lists the design parameters of Figure 4.11.

Parameter	**Value**
I_3 (nA)	10
$\left(\frac{W\ (\mu m)}{L\ (\mu m)}\right)_{Mn3-8}$	$\left(\frac{9.6}{4}\right)$
$\left(\frac{W\ (\mu m)}{L\ (\mu m)}\right)_{Mp3-4}$	$\left(\frac{14}{2}\right)$

Table 4.4. Design parameters of the cascode current mirror.

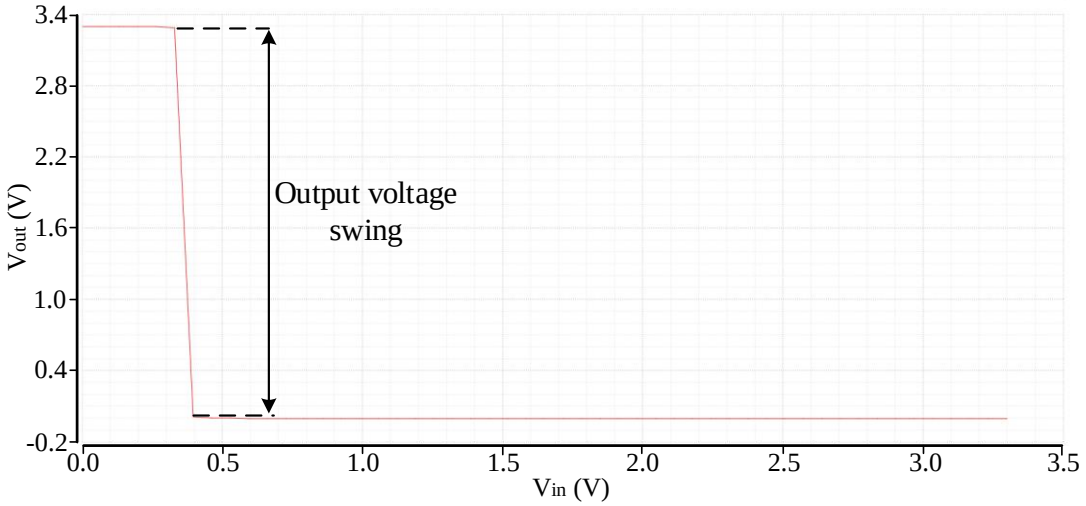

Figure 4.12 Simulated output voltage swing of the amplifier with the cascode current mirror.

The switches implemented in the design uses a complementary topology for minimum charge injection [85], as shown in Figure 4.13. When the switch turns off the injected charges for each transistor are opposite and therefore will cancel each other [87]. This is achieved when $W_1 L_1 C_{ox}\left(V_{ck} - V_{in} - V_{th,n}\right) = W_2 L_2 C_{ox}\left(V_{in} - \left|V_{th,p}\right|\right)$. The equivalent Ron of the complementary switch is the parallel combination of the Ron of the two transistors, and can operate over a wide input voltage range.

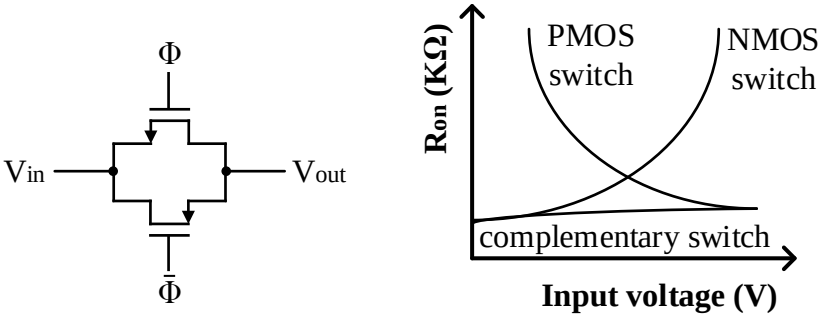

(a) (b)

Figure 4.13 Complementary switch (a) schematic (b) on-resistance.

4.6.2 NOISE CANCELLATION

The noise sources in image sensors are classified into two categories the spatial or fixed pattern noise (FPN) and the temporal noise. The FPN is the output pixel to pixel variation when they are uniformly illuminated. It is generated by component mismatches that are caused from manufacturing process, and variations in doping and lithography [72]. The FPN is subcategorised in offset FPN and gain FPN. The offset FPN is due to amplifier offset variation [81]. Also the FPN caused by dark current variation is considered as offset FPN and is called dark signal nonuniformity (DSNU) [80]. The gain FPN depends on the signal variations level and is called photo response nonuniformity (PRNU). The temporal noise consists of the shot noise from statistical fluctuation of photocurrent and dark current, the readout noise which includes the thermal and flicker (1/f) noise of the readout electronics and the reset noise or *KT/C* noise from the thermal noise of the reset switch [80].

In CIS the attenuation of the FPN and reset noise is achieved using Correlated Double Sampling (CDS) technique, where the pixels output is sampled under reset conditions and again after the integration level and then subtracted one from the other [88]. Even though the CDS can be directly implemented in 4T-APS topologies, in 3T-APS and CTIA architectures it cannot because the read and reset operations are coupled to the integration period and therefore memory cells are needed [37]. Instead, the delta difference sampling (DDS) technique is used in the 3T-APS and the CTIA architecture. This technique can be used for the reduction of FPN but not reset noise. This is because it calculates the difference between the pixels output signal after integration and again after the reset of the next frame [80], [89]. Both CDS and DDS circuits are usually implemented at the end of each column and are shared between the pixels of the same column [72]. Figure 4.14 shows two examples of the implementation of CTIA architecture with CDS [90] and CTIA architecture with DDS [89].

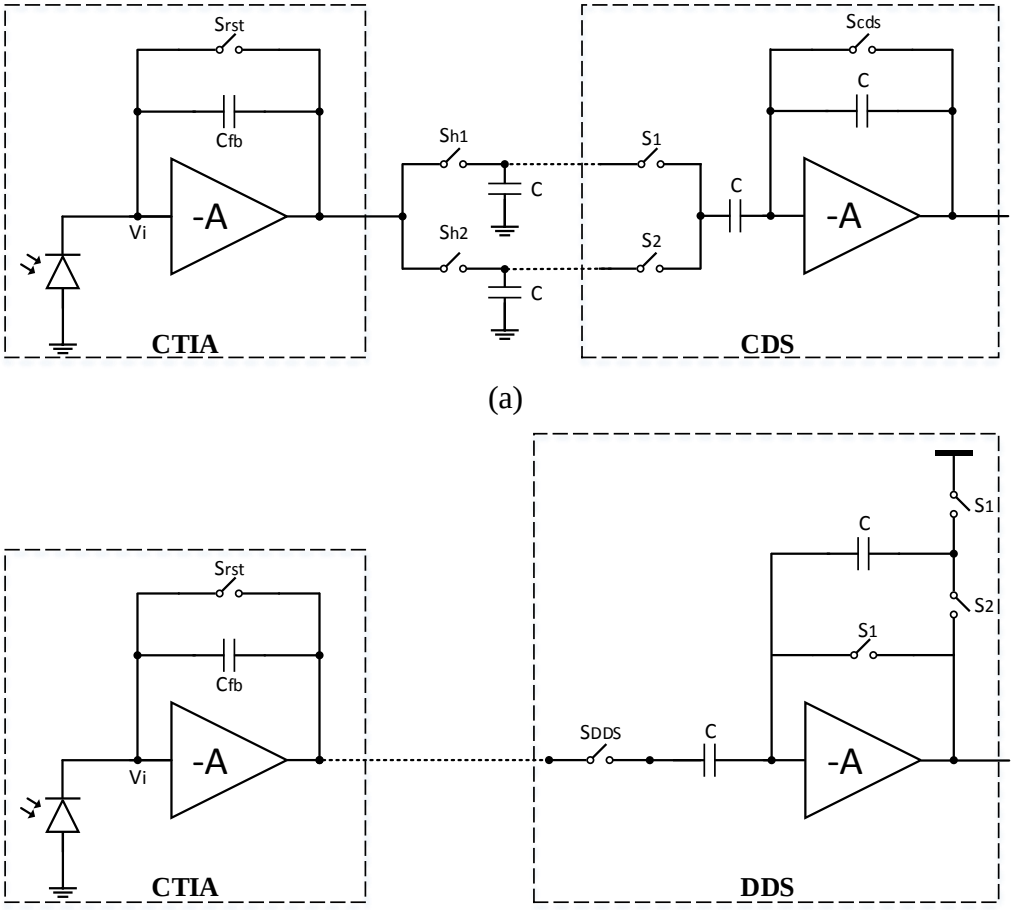

Figure 4.14 (a) CTIA architecture with CDS [90] and (b) CTIA architecture with DDS [89].

The noise charges at the output after the implementation of CDS as shown in Figure 4.14 (a) are:

$$Q_{int} - Q_{rst} = (Q_{FPN} + Q_{rst} + Q_{read2} + Q_{shot} + Q_{DSNU} + Q_{PRNU}) - (Q_{FPN} + Q_{rst} + Q_{read1}).$$
$$\rightarrow Q_{int} - Q_{rst} = Q_{read2} - Q_{read1} + Q_{shot} + Q_{DSNU} + Q_{PRNU} \quad (4.18)$$

Where Q_{FPN} is the offset FPN due to amplifier, Q_{shot} is the shot noise, Q_{read} is the readout circuit noise, Q_{DSNU} is the FPN due to dark signal nonuniformity and Q_{PRNU} is the photo response nonuniformity . Q_{int} is the output charge at integration level and Q_{rst} is the output charge at reset level.

The noise charges at the output after the implementation of DDS as shown in Figure 4.14 (b) are:

$$\begin{aligned} Q_{int} - Q_{rst} &= (Q_{FPN} + Q_{rst1} + Q_{read1} + Q_{shot} + Q_{DSNU} \\ &\quad + Q_{PRNU}) - (Q_{FPN} + Q_{rst2} + Q_{read2}). \\ \rightarrow Q_{int} - Q_{rst} &= Q_{read1} - Q_{read2} + Q_{rst1} - Q_{rst2} + Q_{shot} \\ &\quad + Q_{DSNU} + Q_{PRNU} \end{aligned} \tag{4.19}$$

The proposed circuit for processing the photocurrent consists of a new compact circuit architecture, which combines the CTIA with noise reduction, as shown in Figure 4.15, [91]. Both operations are performed using the same amplifier, reducing the power consumption by half compared to the CDS and DDS topologies.

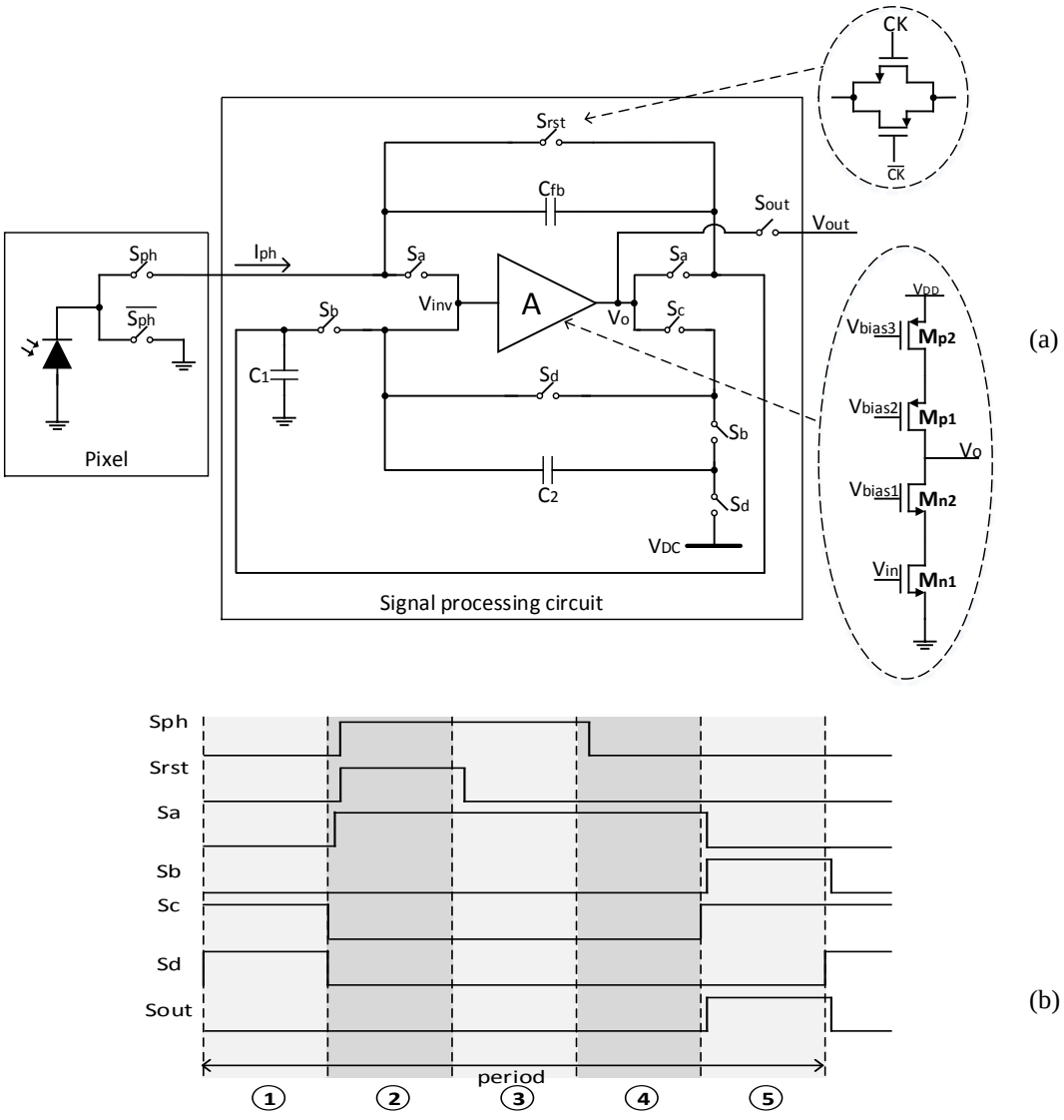

Figure 4.15 (a) Schematic of the pixel and processing architecture and (b) timing diagram.

The available drain current to M_{n1} is defined by bias voltage V_{bias3} and M_{p2} (chosen as 10 nA). The initial dc value of the gate of M_{n1} is set by short circuiting its output to its input by switch S_d. The value is thus defined by the drain current of M_{p2}. This voltage is connected to a selected (inversely biased) photodiode by switches. When the reset switch S_{rst} is opened the diode photocurrent I_{ph} charges the feedback capacitor C_{fb} [85] [91]. By the choice of a small value capacitor the output voltage V_{int} of the amplifier is:

$$V_{int} = \frac{1}{C_{fb}} \int I_{ph} dt \tag{4.20}$$

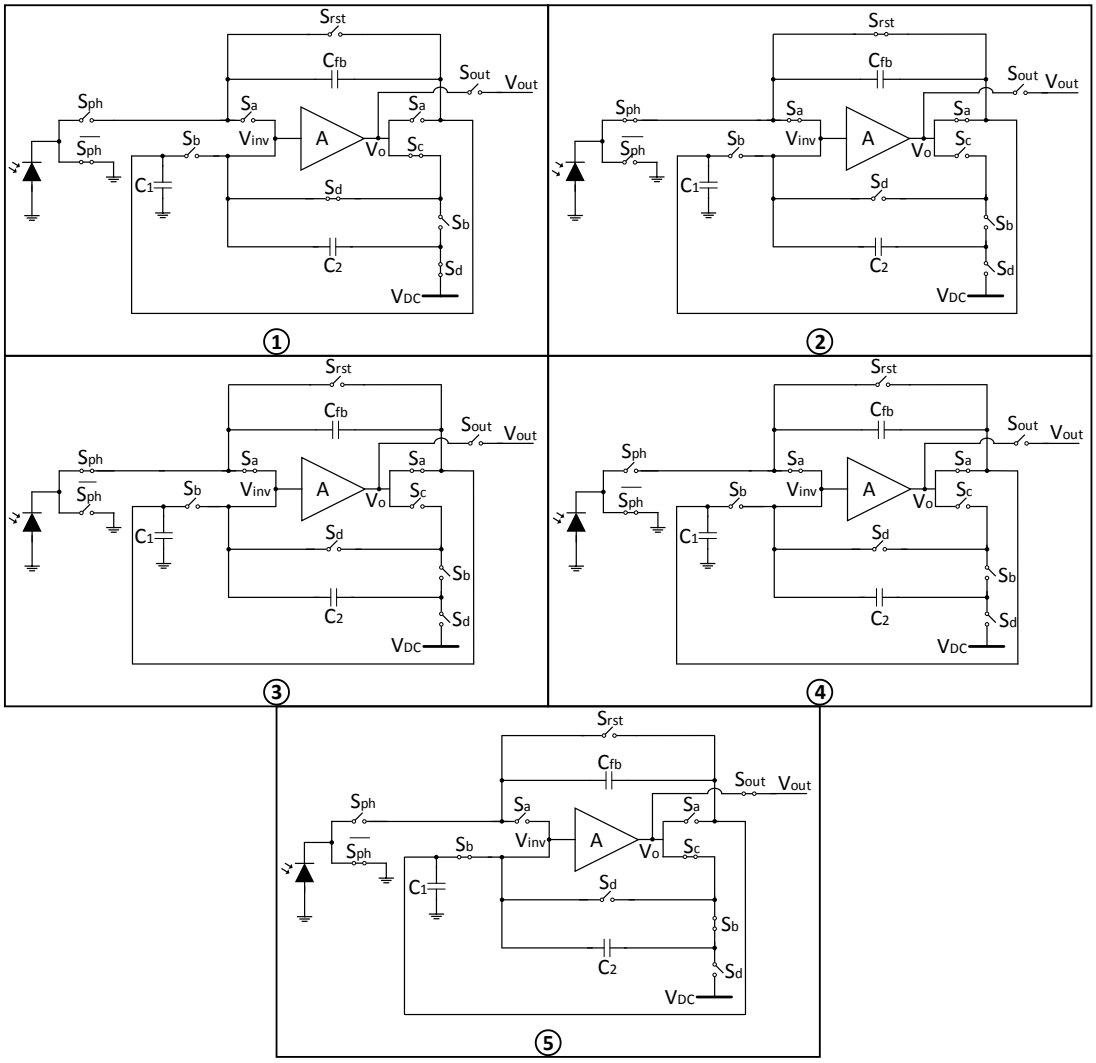

Figure 4.16 Schematic illustration of the 5 phases required for the conversion of photocurrent to voltage and noise cancellation.

The processing circuit requires 5 phases to generate a voltage at the output node V_{out} in response to the incident photons at the input as shown in Figure 4.15(b). In phase 1 the charge stored on C_2 is $V_{inv} - V_{DC}$, were V_{DC} is an external reference dc voltage level and V_{inv} is the inverse voltage level from the amplifier. In phases 2 and 3 the reset and integration operations are performed respectively, similar to a conventional CTIA topology, as shown in Figure. 4.16. In phase 4 the integrated voltage is held constant and stored on C_1. Subtraction of the charges is performed in phase 5. Both C_1 and C_2 have the same value. The output voltage V_{out} is given by

$$V_{out} = V_{DC} + V_{inv} - V_{int} \tag{4.21}$$

where V_{int} is the integrated voltage as described in Equation 4.20.

Given that the photocurrent in CTIA starts to integrate from the V_{inv} level, the resulting output voltage V_{out} of the proposed processing circuit will be independent of the V_{inv} voltage level where:

$$V_{out} = V_{DC} - \frac{I_{ph} \cdot T_{int}}{C_{fb}} \tag{4.22}$$

T_{int} is the integration time.

Figure. 4.17 shows the simulated output voltage at the node V_o for all the 5 stages when $V_{DC} = 2V$. Both V_{inv} and V_{rst} have the same value of 364 mV. V_{rst} is the output voltage at phase 2. Using Equation 4.21 and $V_{int} = 787mV$ the output voltage can be calculated as $V_o = 1.57V$ which is equal to the output voltage shown in the Figure 4.17. The glitches observed at the output signal (V_o) in Figure 4.17 are due to overlapping clock signals as shown in Figure 4.15(b).

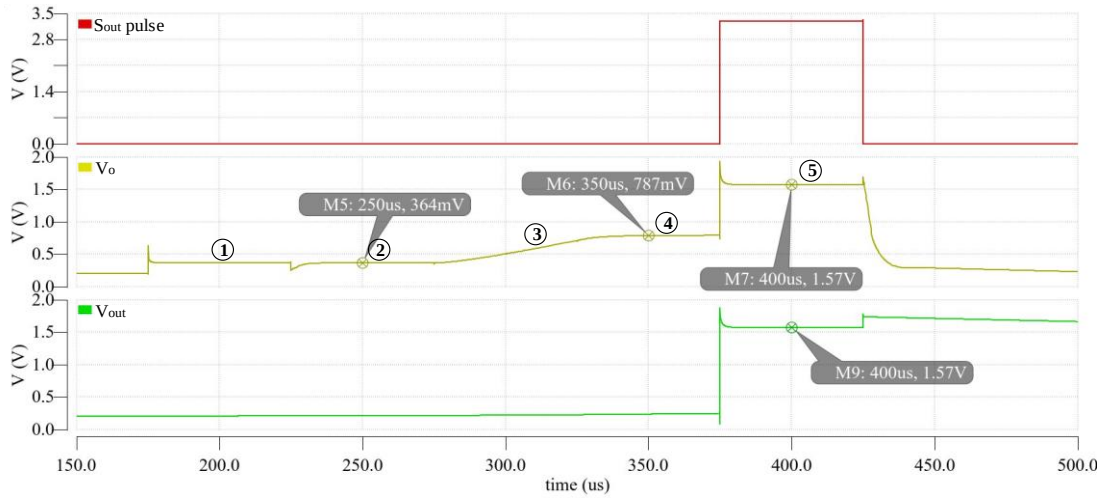

Figure 4.17 Simulation of the output voltage at V_o and V_{out} nodes. The circled numbers indicate the five different phases required for the processing of the photocurrent. In phase 5 the S_{out} pulse is enabled allowing the voltage to exit the processing circuit (V_{out}).

The noise charges at inverse level are:

$$Q_{inv} = Q_{FPN} + Q_{read1} \tag{4.23}$$

The noise charges at integration level are:

$$Q_{int} = Q_{FPN} + Q_{read2} + Q_{rst} + Q_{shot} + Q_{DSNU} + Q_{PRNU} \tag{4.24}$$

Therefore at the output of the processing circuit the noise charges will be:

$$Q_{out} = Q_{read1} - Q_{read2} - Q_{rst} - Q_{shot} - Q_{DSNU} - Q_{PRNU} \tag{4.25}$$

Equation 4.25 shows that at the output of the proposed processing circuit the offset FPN will be suppressed, while the read noise will increase and the reset noise due to the feedback switch remains.

Comparing the proposed circuit with CTIA - CDS and CTIA - DDS it is evident that even though in all topologies the offset FPN is suppressed in the proposed circuit this is performed using one amplifier instead of two and therefore requiring half the power consumption at the cost of extra switches. In DDS the reset noise is double while in the proposed circuit it remains constant. In CDS the reset noise is cancelled at the cost of an extra two capacitors. In both circuits only the reset noise of CTIA due to feedback capacitor has been considered ignoring the other reset noises. This is because all other capacitors are expected to have large value and therefore much small reset noise compared to the noise due to feedback capacitor. In the proposed circuit C_1 and C_2 are 200 fF resulting in 0.14 mV_{rms} reset noise for each capacitor, which is more than 4.5 times smaller than reset noise due to feedback capacitor.

Figure 4.18 shows a Monte Carlo analysis for process and mismatch variations performed for both the proposed architecture and the conventional CTIA pixel without noise cancellation. The results shows reduction of the output voltage variation for the proposed architecture.

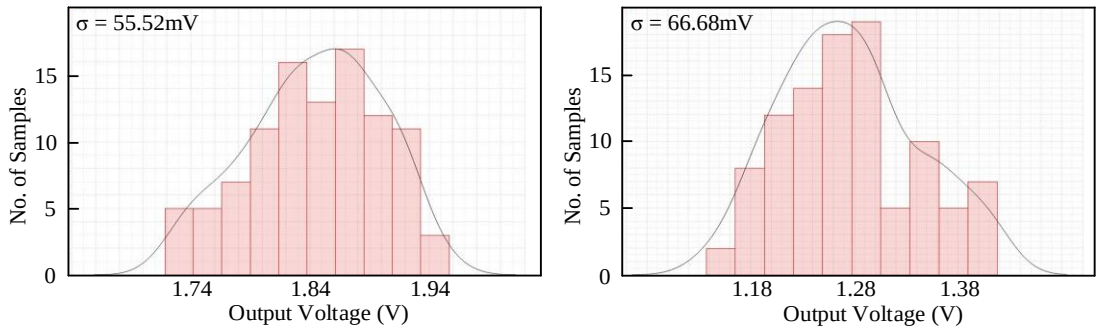

(a) (b)

Figure 4.18 Output variation using Monde Carlo analysis in (a) the proposed architecture and (b) the output of conventional CTIA architecture.

4.6.3 PIXEL ARCHITECTURE

Each pixel was realized using one n-well/p-substrate photodiode of 20 μm × 20 μm, two switches connected to the cathode of the photodiode and two logic gates to control the switches operation, as shown in Figure 4.19. When both the Row selection signal is available and the S_{ph} signal is high the AND logic gate sent a pulse to close the switch S_1 that connects the photodiode with the processing circuit. In this way, the photocurrent is transferred to the processing circuit. The S_2 switch is controlled by an OR logic gate through the combination of signals $\overline{Row}$ and $\overline{S_{ph}}$. When the S_2 closes, the photodiode is connected to ground. The use of OR gate could have been omitted and instead a NOT gate could be have been used to control the S_2 signal based on $S_2 = \overline{S_1}$. However, that would not have much effect on the pixel's fill factor given that the size of both OR gate and NOT gate are similar.

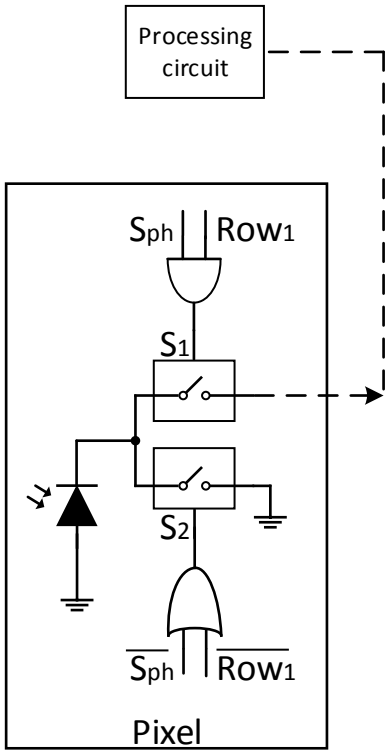

Figure 4.19 Pixel architecture.

The proposed design allows the pixel binning technique to be implemented. In this technique the photocurrent of multiple pixels is combined together increasing the sensitivity of the CIS at the cost of reduced resolution [88]. In this design the photocurrent of the 2, 3 or 4 pixels of the same column can be combined to increase the CIS's sensitivity. This is achieved by having the same Row signal as follows: Row1 = Row2 and Row3 = Row4 for 2 pixel binning or Row1 = Row2 =Row3 for 3pixel binning or Row1 = Row2 = Row3 = Row4 for 4 pixel binning.

4.7 CURRENT BIAS CIRCUIT

A current divider has been used for biasing the CIS reducing the externally provided input current of 1 μA to 10 nA. In this way extensive and complicated off chip instrumentation setup is avoided for the generation of nano-ampere range current. The implemented topology is shown in Figure 4.20, and is based on [92]. The principle of operation of this current divider is based on the linear division of the current when

flowing in or out of two MOS transistors that have the same gate voltage. The current (I_{REF}) is divided in each branch by the *N* factor. Transistor size ratios are shown in Table 4.5.

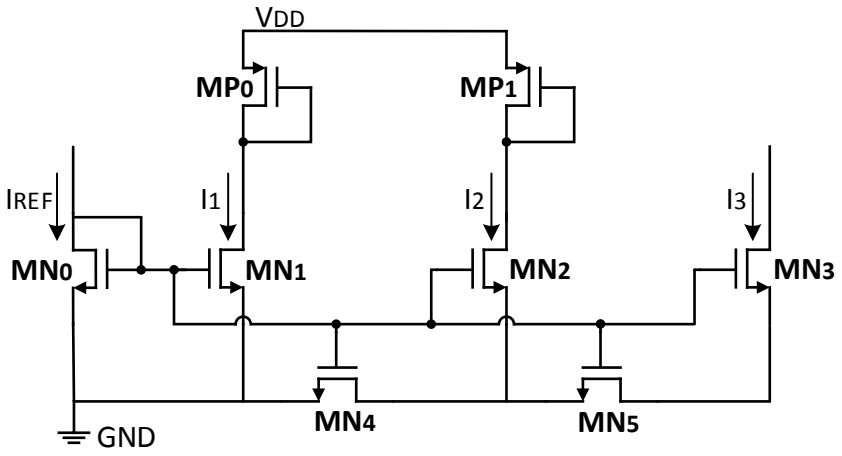

Figure 4.20 Circuits schematic of current divider.

.Parameter	Ratio	Value
$(W/L)_{MN_{0-2}}$	$N-1$	$22.5\mu m/2.5\ \mu m$
$(W/L)_{MN_{4-5}}$	$N/(N-1)$	$25.2\mu m/22.5\mu m$
$(W/L)_{MN_3}$	1	$2.5\mu m/2.5\mu m$
$(W/L)_{MP_{0-1}}$		$14\mu m/2\mu m$

Table 4.5. Transistors size ratios and their actual value.

I_{ref} was selected to be 1μA and the value of *N* is equal to10. Therefore only two branches are required to reduce the 1μA to 10nA. P-type metal-oxide semiconductor (PMOS) transistor loads on the N-type metal-oxide semiconductor (NMOS) transistors to keep them in saturation. Monte Carlo analysis performed for the simulation of the DC current variation due to mismatches error in the 3 branches. Figure 4.21 shows histograms of Monte Carlo analyses and the mean and standard deviations. The analysis performed for 100 runs. In the third branch after the 10 nA current was available it was copied into the 64 amplifiers using cascode current mirrors with interdigitated fingers in order to minimize mismatches.

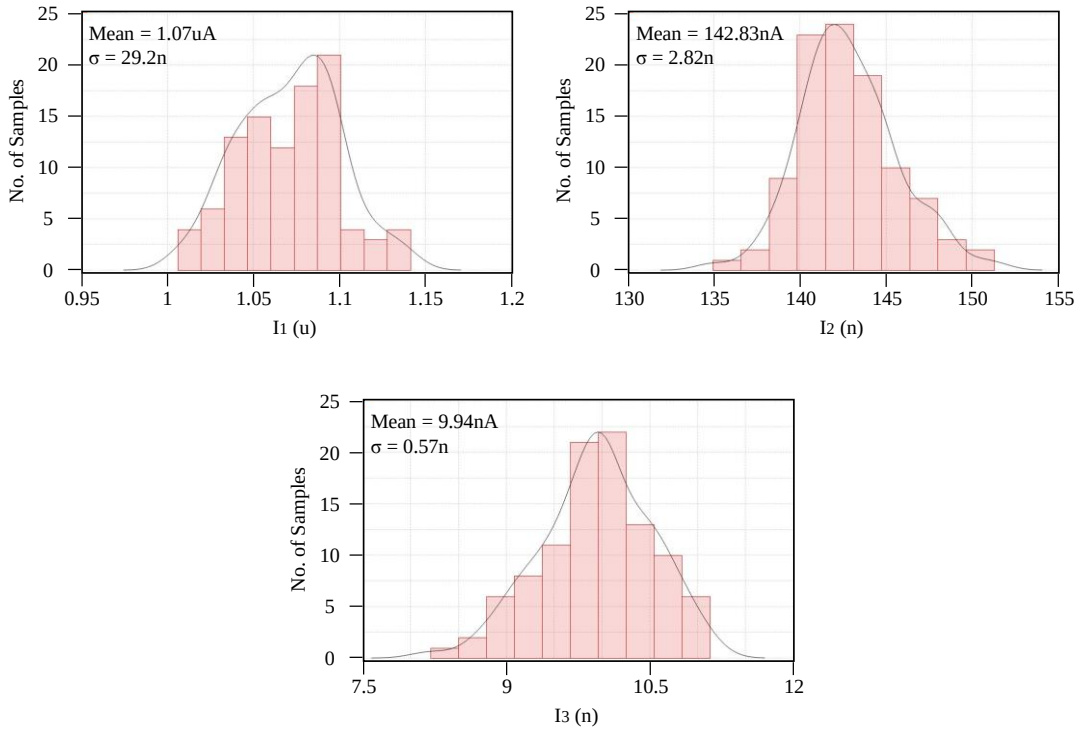

Figure 4.21 Monte Carlo analysis of the output current variation of each branch due to mismatch error.

4.8 PERIPHERAL CIRCUITS

The row selection is controlled externally whereas the column selection is performed serially on chip. Once the row is selected the pixel of the first column is enabled and its photocurrent is sensed and processed by the circuit. While the processing is in progress the pixel of the next column is enabled, sending its photocurrent to its respective column processing circuit. When the output of the first pixel is available the second pixel is still in the processing mode. The output of each column has an integration time, T_{int} seconds delay from its previous column, where T_{int} can be between 40 μs-4 ms. All outputs of the processing circuits are connected together to the gate of a single PMOS transistor (which acts as a voltage buffer) and then its source is connected to a single pad.

The Master clocks with one clock delay between each stage were generated using a serial-input to parallel-output 64 - bit shift register with JK flip-flops as shown in

Figure 4.22 to generate 64 master clocks for each column. Initially all flip-flops (FFs) are reset to logic level "0". At T_3 clock the $Data_2$ pulse is at logic level "1" and thus output of the first FF Q_1 at T_4 becomes "1" whereas the outputs of all the other FFs will remain at "0". Since Q_1 is connected to J_2 the output of the second FF (Q_2) at T_5 will be "1". The $Data_2$ will continue shifting to the right in each clock pulse until the last logic level "1" reaches the 64th FF. The output of each FF is also connected to an AND logic gate. When both the inputs of the AND gate are high the output of the gate is also high generate the Master clocks (CLK_M) that will be used in the next stages. In total 64 CLK_M are generated with one clock_shift pulse delay from each other.

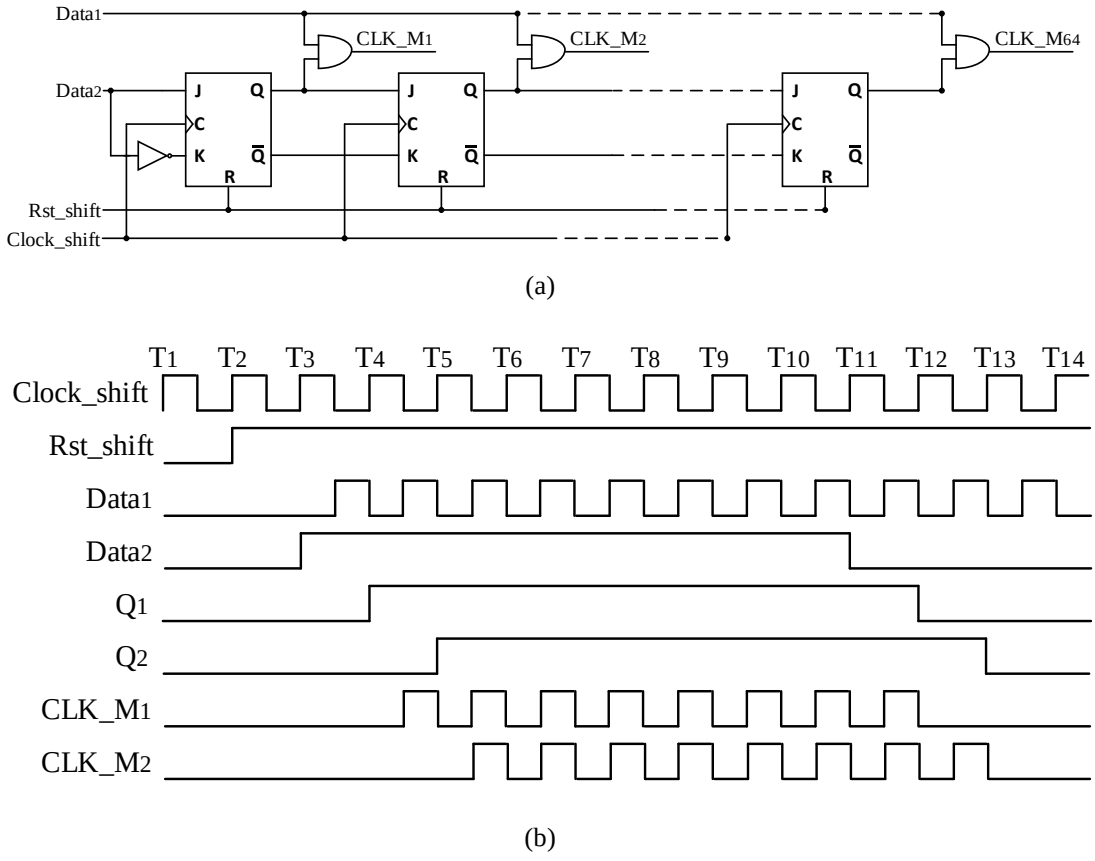

Figure 4.22 (a) Circuit diagram of serial input parallel output shift register and (b) pulse diagram.

In every column there is a 3-bit synchronous "up" counter that has been implemented using 3 JK FFs as shown in Fig. 4.23 (a). The input clock of the counter is the master clock generated from the shift register. The operation of the JK FF is shown in Table 4.6. $Q_{(t)}$ refers to the state of the FF output before the clock edge and $Q_{(t+1)}$ refers to the state after the clock edge [93].

J	K	$Q_{(t+1)}$
0	0	$Q_{(t)}$
0	1	0
1	0	1
1	1	$Q'_{(t)}$

Table 4.6. JK flip-flop operation.

Initially all the FFs are reset with their outputs at "0" logic level. Then the first FF change logic state with every clock positive edge pulse $\overline{CLK\_M}$. The output of the second FF changes state for every clock period of the output of the first FF. Finally the output of the third FF changes state for every clock period output of the second FF. Fig. 4.23 (b) shows an example of the pulse generated from the counter when the CLK_M_1 is used as master clock from the shift register.

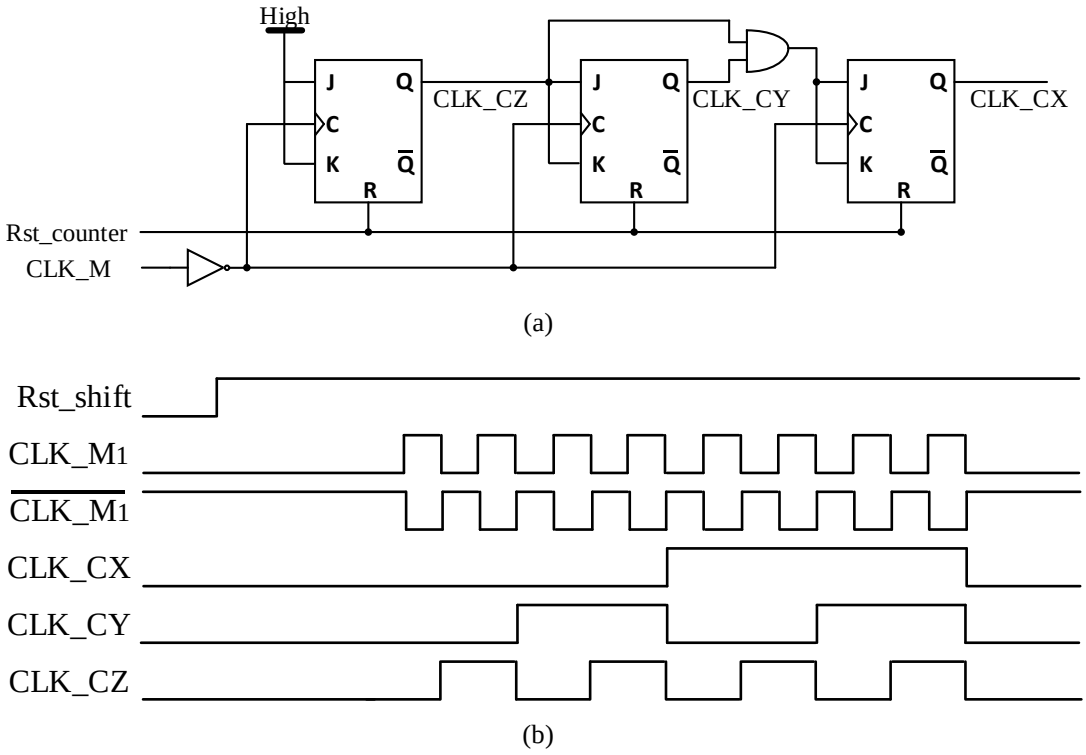

Figure 4.23 (a) Circuit diagram of 3-bit counter and (b) example of the pulse diagram when the input master clock is CLK_M_1 from the shift register.

The 64 counters were connected with 64 switching pattern blocks. These blocks used the three clocks generated from the counter to produce the various pulses required for the proper operation of the CTIA with noise cancelation circuit. The optimum logic gate level realization of the required pulses was achieved by deriving a Boolean function to describe each pulse that was achieved using the Karnaugh map method. Figure 4.24 shows the resulting gate implementation. D FFs were used at the output of each gate configuration. The D FFs replicate the input to the output when the clock pulse is enabled. In this way ripple effects of the pulses at the input of D FFs are avoided and all signals are synchronize since all D FFs uses the same clock pulse.

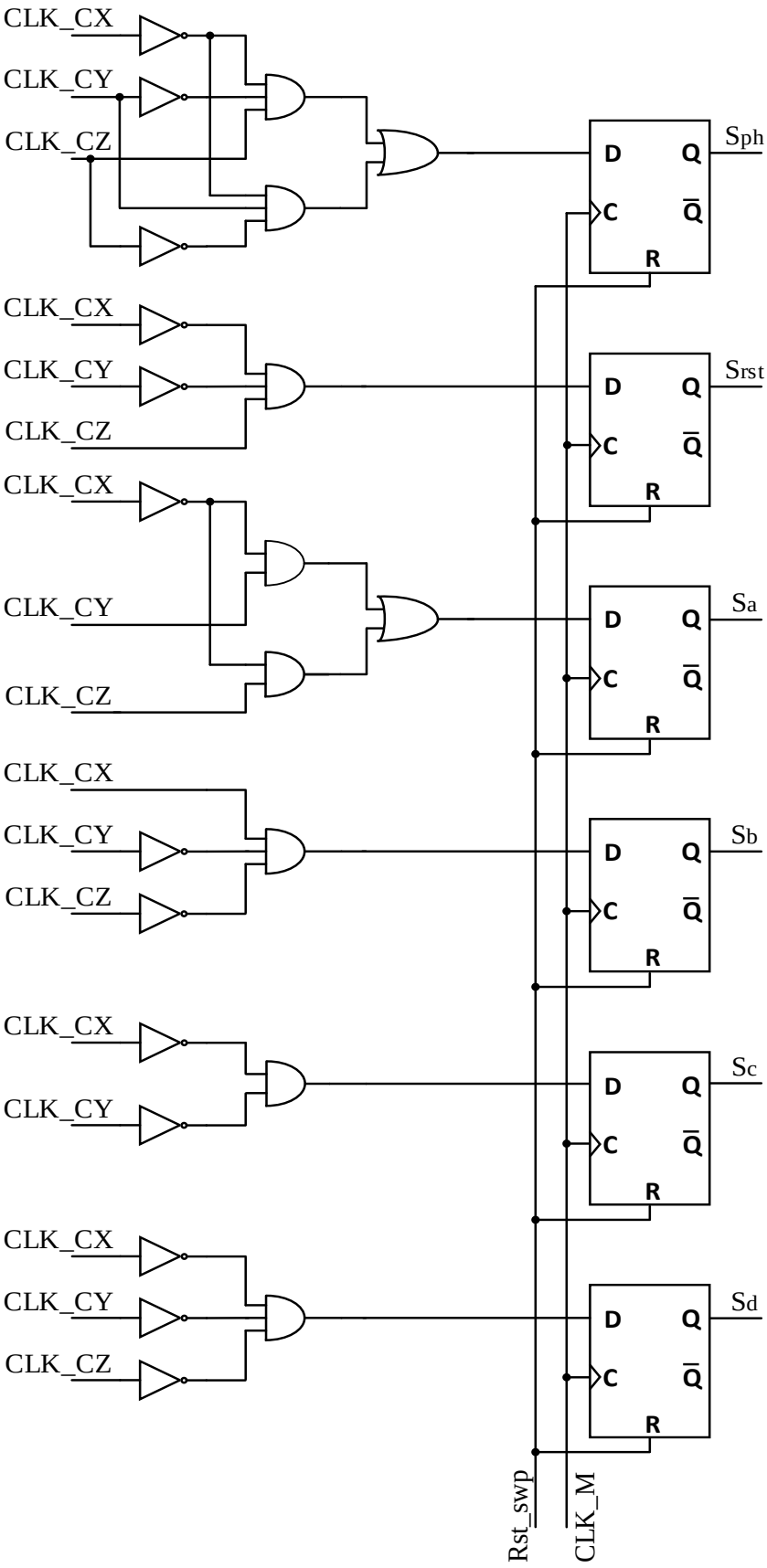

Figure 4.24 Gate level realization of the required pulses for the pixel correct operation.

4.9 CHIP LAYOUT

The chip layout was designed using foundry design rules and basic layout techniques. Among the techniques used are the common-centroid which is used to minimize the process variation in the chip. This was performed by dividing the matching transistor into two halves and placing each in a way that all components have the same centroid. Another method used to reduce the gate resistance of wide transistors is by folding the transistors into multiple fingers. Also dummy structures were added to reduce the influence of the surrounding environment in the circuit of interest. Figure 4.25 shows the chip micrograph. The overall chip area is 12.28mm^2 including the pads. The pads were arranged on two sides for maximum area efficiency. Table 4.7 summarises the area of main building blocks of the CIS.

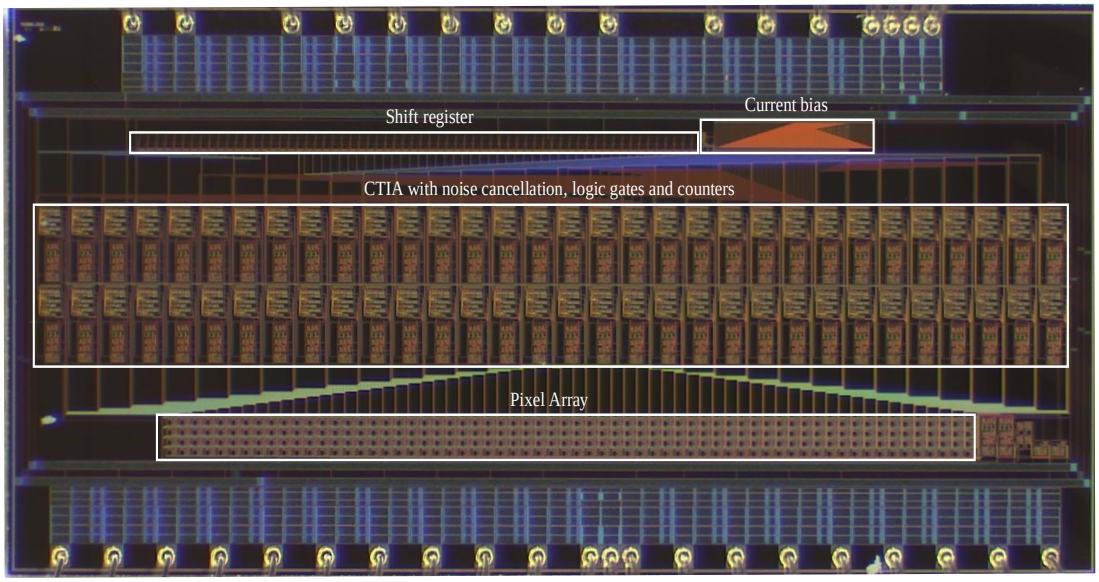

Figure 4.25 CIS chip micrograph.

Block	Size
Pixel Array	$3957\ \mu m \times 147\ \mu m$
CTIA with noise cancellation, logic gates and counters	$5097\ \mu m \times 666\ \mu m$
Shift register	$2763\ \mu m \times 86\ \mu m$
Current bias	$859\ \mu m \times 134\ \mu m$

Table 4.7. Size of main building blocks

4.10 DISCUSSION

The circuit design of a CIS specifically fabricated to be used in readers for LFIA at the point-of-care was presented. The aim was to further improve the second generation system presented in chapter 3 by replacing the of the shelf component linear sensor array with the proposed CIS. The chip was implemented in 0.35 μm CMOS technology with 3.3 V power supply. The CIS was designed to have low power consumption, since it will be used at the point-of-care. Low noise and good SNR was required so that the sensor can distinguish the various concentrations in LFIA, even when the test line is faint. The optimum number of pixels was used in order to minimize the excess power consumption, which is 4 × 64.

Among the most common pixel topologies 3T-APS, 4T-APS and CTIA, the latter was chosen. This is because the sensitivity is controlled by the feedback capacitor and photodiode size, and the voltage across the photodiode is kept constant.

A new compact pixel architecture was proposed for the offset FPN cancellation, which combined the CTIA performance with noise cancellation using only one amplifier. All the transistors were biased in subthreshold and thus consumed low power. The CIS specifications required only 4 rows of pixels and therefore the processing circuit could be placed outside the pixels. However, in CIS where many row of pixels are required the processing circuit must be placed inside the pixel consuming space and reducing the fill factor. Consequently further simplification and more compact layout design is required for the proposed processing circuit to be implemented in the CIS for other applications.

The current bias of the CIS was implemented using a current divider which divided the current of 1μA to 10nA, using only two branches. The column address performed using digital structures, where the row selection operated using an external pulse.

The simulation results of the chip showed that it can successfully convert the photocurrent into a logic level voltage output while removing the offset FPN. Basic layout techniques were implemented in order to minimize mismatching and process variations. Improvement of the pixel layout design can further increase the fill factor.

4.11 CONCLUSION

In this chapter the performance of the developed CIS is presented. From the analysis performed and the obtained results the following conclusions can be drawn:

- This system's specifications can be used as a benchmark for future CIS designs for LFIA's readers.
- CTIA and FPN noise cancellation operations can be combined reusing the same amplifier and therefore reduce the power consumption.
- Image sensor design with a bias current of 10nA is possible using transistors biased in subthreshold.

5

ASIC MEASUREMENT PERFORMANCE

Initially the electrical performance of the fabricated CIS is investigated in regards to different light irradiances, different integration times and binning and not binning techniques. Several parameters that characterise the function of CIS are defined and compared to other CIS used for biomedical applications. The proposed design shows good response in terms of noise and power consumption.

Next, the reader is built based on the results from ray trace measurements. The developed reader is tested with LFIA strip with Influenza A nucleoprotein in various concentrations. The results show that the developed CIS can detect the different LFIAs with limit of detection around 0.5 ng/mL.

5.1 ELECTRICAL PERFORMANCE

The main equipment used for the assessment of chip performance includes: a current regulator for the current bias of the chip, two power supplies to supply the chip with V_{DD} and V_{dc} voltages and a complex programmable logic device (CPLD) board (Xilinx, Coolrunner II) for the generation of all the digital pulses from an external 2MHz crystal oscillator, as shown in Figure 5.1(a). All these components were mounted in a custom made PCB board. Figure 5.1(b) shows a photograph of the test setup.

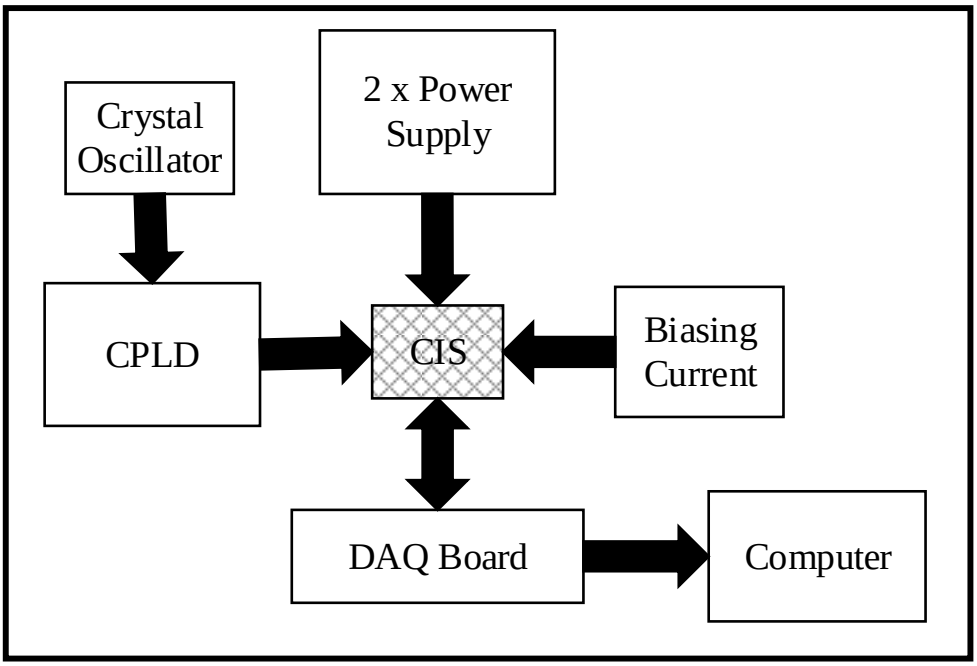

(a)

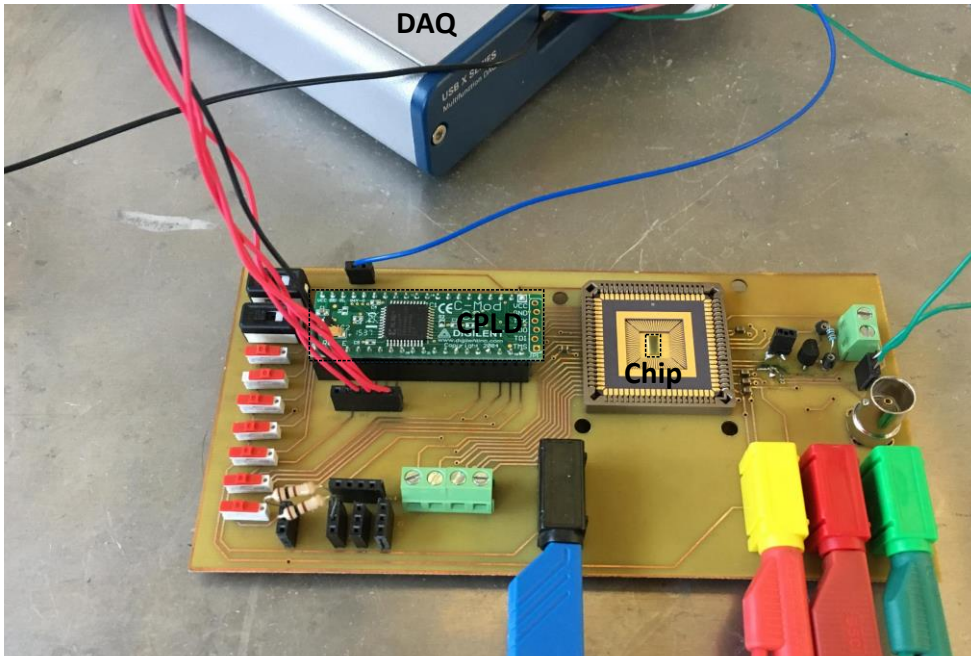

(b)

Figure 5.1 (a) Diagram of the measurement setup and (b) photograph of the setup.

A Verilog code was generated in order to program the CPLD device. Using only one external clock all the input pulses required for the correct operation of the chip like Row pulses, Clock_Shift, Rst_Shift etc were generated. The Verilog code was written in way to provide selection of different integration times from predefined options and the choice of binning technique or not. Figure 5.2 shows the simulated Verilog code, operating at 50µs integration time. These pulses follow the details shown in chapter 4.8.

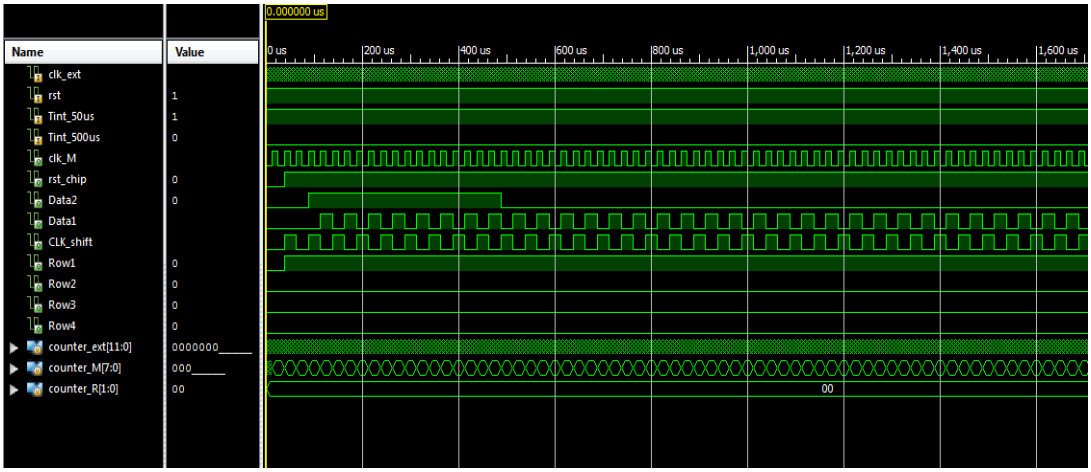

Figure 5.2 Simulation results of the Verilog code used for program of the CPLD boards.

The analog output of the ASIC CIS was digitized and interfaced to the PC with a data acquisition system (DAQ, National Instrument) and its 16-bit ADC. A custom LabVIEW code was generated for signal recording. Figure 5.3 shows the LabVIEW window during the operation of the chip. The specific snapshot shows the recording of the output voltage (white line) during the end of R_{ow1} (green pulse) reading and at the beginning of R_{ow2} (blue pulse). The red pulse is read from the chip and indicates the S_{out1} pulse from the first processing circuit out of the 64 processing circuits.

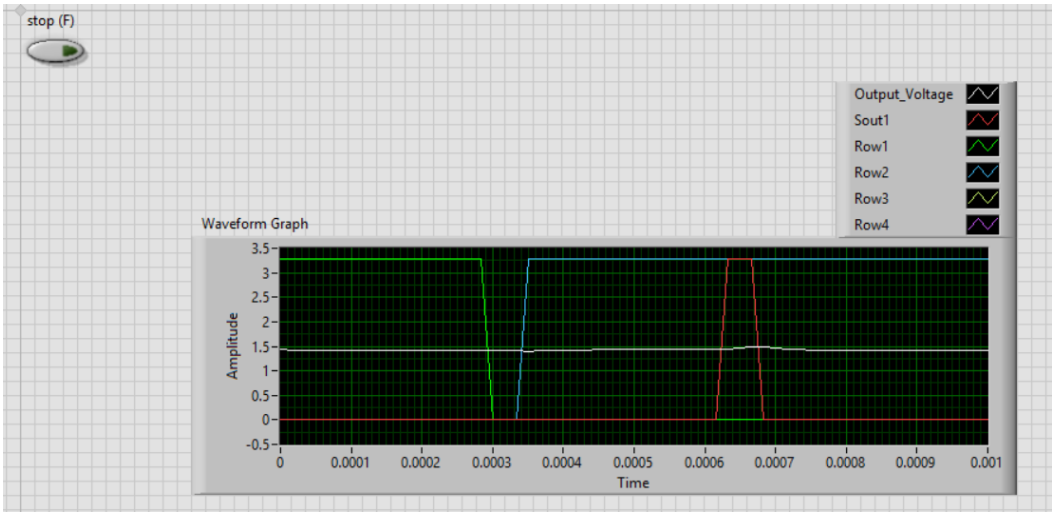

Figure 5.3 LabVIEW window during the recording of the CIS output voltage.

The experimental characterisation of the chip was performed with using a monochromatic LED light source with a centre wavelength of 525nm. The LED was positioned on top of the chip at a fixed distance to create uniform irradiance over the entire active area. Then for different LED irradiances the pixels responses were measured. The irradiance of the LED was measured with a power meter. The measurements were performed with the CIS chip operating at 67 frames per second (fps) with V_{DC} = 2 V. A total number of 100 frames were sampled for each irradiance for analysis. The sampling frequency of the DAQ was at 60 KHz, so that for T_{int} = 50 μs, three measurements were obtained for each pixel each frame. In order to ignore settling effects between the pixels only the middle value of the three was stored and used in the calculations. Figure 5.4 shows the average output voltage of all the pixels over 100 frames for different irradiances. The voltage output of the pixels decreases when the light intensity is high whereas when the light intensity is low the voltage output increases up to the saturation voltage level. The linear range of operation is approximately 1.7 V, [91].

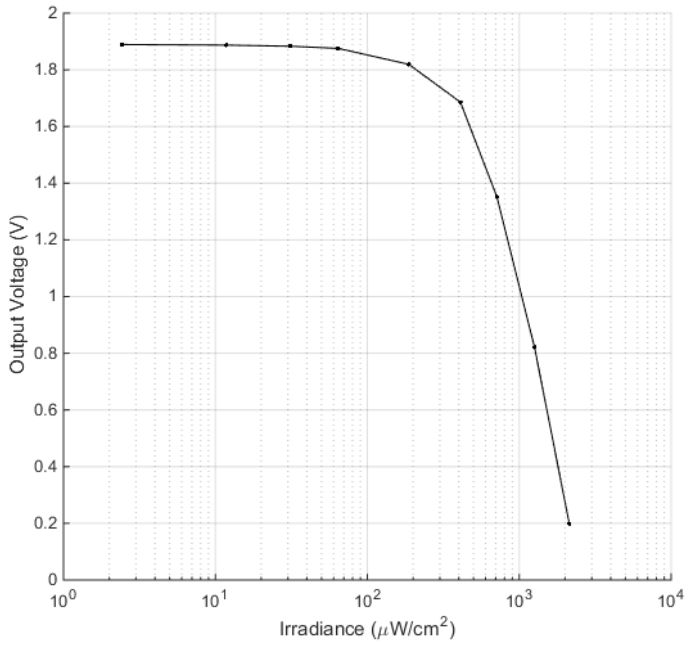

Figure 5.4 Output voltage of all pixels. The measurement performed using 100 frames at increasing light intensity. The CIS had integration time 50μs. The centre light wavelength was 525nm.

The calculation of the FPN was performed by producing an average image from the 100 frames of the same irradiance and then calculating the standard deviation of

all pixels in that frame normalized to the saturation voltage [85][94]. The FPN at 2.1 mW/cm^2 irradiance is 1% and at the dark (no light) is 1.8%. This FPN is due to mismatches in the feedback capacitor C_{fb} and in the ratio of C_1 and C_2 capacitors of the processing circuits [85].

The SNR was calculated using Equation 5.1 for N = 100 and the results are shown in Figure 5.5 where μ_i is the *i*th mean output pixel value, $\mu_{i,D}$ is the *i*th mean output pixel value at dark and σ_i the *i*th standard deviation. *N* is total the number of pixels. As shown in Figure 5.5 the SNR is approximately at 50 dB at irradiance 2.1 mW/cm^2.The dynamic range is approximately 45 dB and was calculated as the ratio of the maximum detectable irradiance to the minimum detectable irradiance [95].

$$SNR = 20log\frac{\left(\sqrt{\left(\sum_{i=1}^{N}\left(\mu_{i,D}^2 - \mu_i^2\right)\right)/N}\right)}{\left(\sqrt{\left(\sum_{i=1}^{N}\sigma_i^2\right)/N}\right)} \tag{5.1}$$

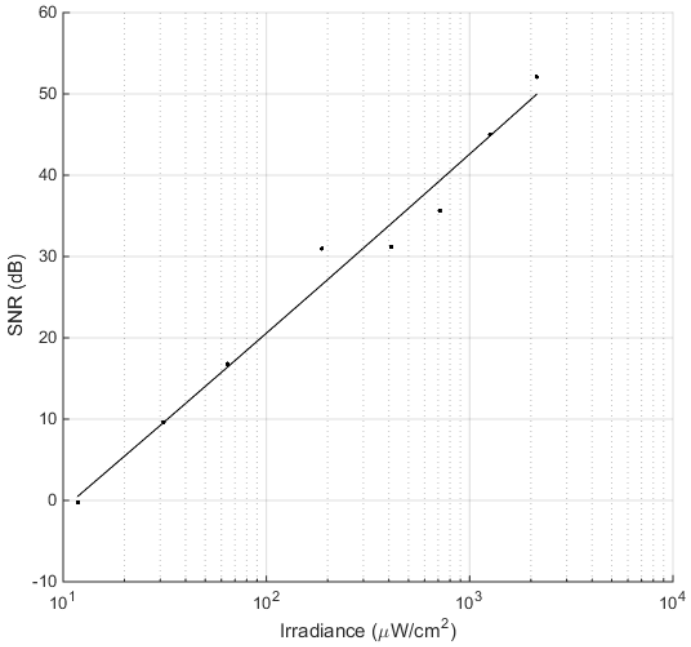

Figure 5.5 SNR of all pixels. The measurements performed using 100 frames at increasing light intensity. The CIS had integration time 50μs. The center light wavelength was 525nm.

The temporal noise was calculated as sum of the squares of standard deviations for each pixel in the 100 frames divided by the total number of pixels. The equation describing this process is the same as the denominator of equation (5.1). The output referred read noise is 1.9 mV_{rms} and was calculated as the temporal noise in zero incident light [96]. Based on the conversion gain ($16\mu V/e^-$) the input referred charge noise is calculated at $119e^-$ [89].

The full well capacity defines the highest number of electrons that can be kept in a pixel [73] and is calculated as shown in equation (5.2) [81]. This parameter is influenced by the photodiode size and structure and the pixel's processing electronics. The chip required 4.1μA current from the 3.3 V analog supply and 2.3μA current from the 3.3V digital supply.

$$full\ well\ capacity = \frac{saturation\ votlage}{conversion\ gain} = \frac{1.9}{16 \cdot 10^{-6}} = 1.2 \cdot 10^5\ e^- \qquad (5.2)$$

Using the same setup as before the output voltages of the CIS for two different integration times, T_{int} = 50 μs and T_{int} = 500 μs have been measured. Again the LED used had wavelength 525nm and the V_{DC} = 2 V. Ten measurements were taken for each irradiance. The average output voltage of each pixel out of 10 frames was calculated to generate one frame. Then from that frame the average output voltage of all pixels for each different irradiance at a time was used to generate the graph in Figure 5.6. For the same irradiance the output voltage is higher for smaller integration time. This response confirms the trend of Equation 4.22. Both graphs saturate at around 1.9V.

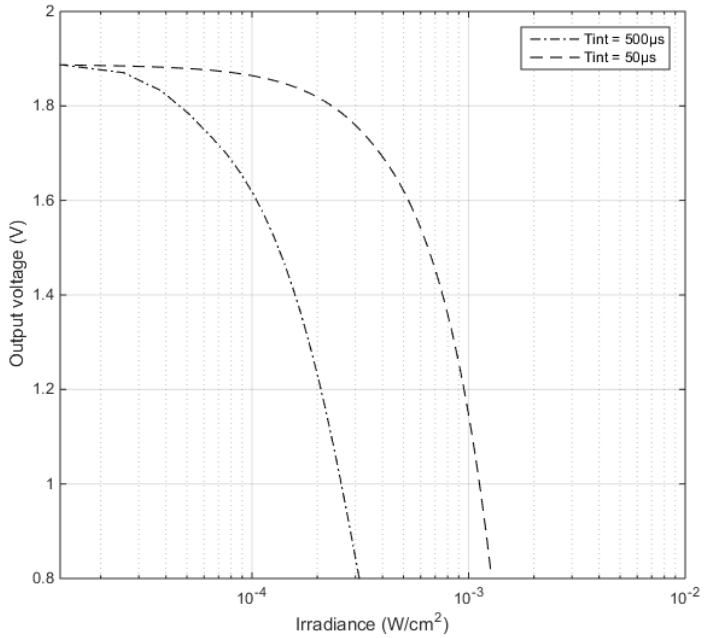

Figure 5.6 Output voltage of all pixels. The measurement performed using 10 frames at increasing light intensity. The CIS had integration times 50µs and 500µs. The center light wavelength was 525nm.

The binning technique was also implemented in the CIS connecting all 4 pixels of the same column to the same processing circuit simultaneously. Figure 5.7 shows the CIS output voltage for different irradiances and 2 different integration times, T_{int} = 50 µs and T_{int} = 500 µs when the binning technique is implemented. All the calculations were performed the same way as before using 10 frames for each irradiance. Comparing Figure 5.6 and 5.7 it is evident that when the binning technique is implemented the operational range of the CIS shifts towards smaller irradiances. This is expected since for smaller irradiances less photocurrent is generated and it is more difficult to be recognised. Whereas when the binning technique is implemented for the same small irradiance the photocurrents of all four photodiodes are added and therefore is easier to be recognised. Table 5.1 summarizes the parameters of the proposed CIS.

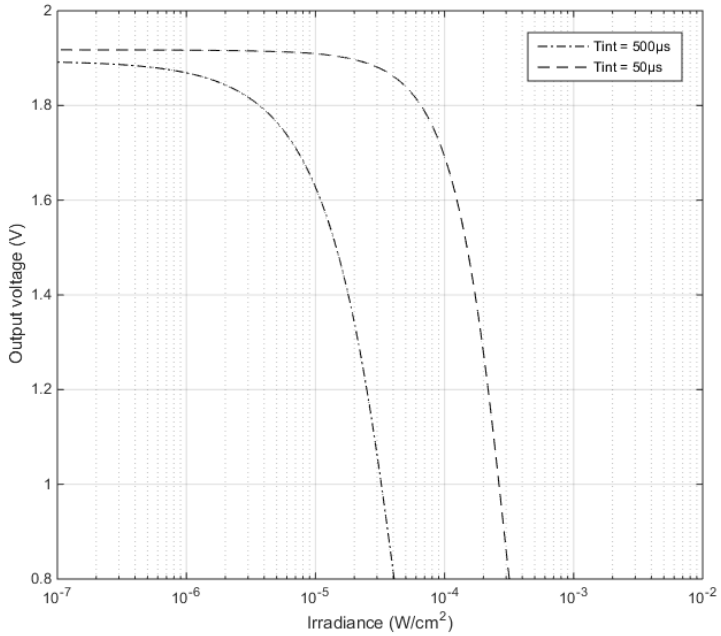

Figure 5.7 Output voltage when binning technique is implemented for all 4 pixels of the same column. The measurement performed using 10 frames at increasing light intensity. The CIS had integration time 50µs and 500µs. The centre wavelength of the light was 525nm.

Parameter	**Value**
Technology	0.35 µm
Pixel Type	CTIA
Number of Pixels	4 × 64
Photodiode size	20 × 20
Pixel size	61.8 µm ×36.7 µm
Pixel Fill Factor	18 %
Frame rate	67 fps
Maximum SNR	50 dB
DR	45 dB
FPN	1.8 % at dark
Conversion gain	16 µV/e^-
Full Well capacity	1.2×10^5 e^-
Power supply	3.3 V
Power consumption	21 µW

Table 5.1. Parameters of the CIS.

5.1.1 COMPARISON WITH OTHER WORK

According to author's best knowledge no other CIS has been designed specifically to be used for LFIA readers, therefore comparison has been made with other CIS used for biomedical applications as shown in Table (5.2). The CIS in this work has low read noise, good SNR and the lowest power consumption per pixel.

Reference	[97]	[85]	[89]	[98]	[99]	[100]	This work
Application	Fluorescent contact imaging	Brain spectroscopic imaging	Fluorescence imaging	Micro-computed tomography	Contact imaging	Fluorescence lifetime microscopy	Reader for LFIAs
CMOS technology	0.35 µm	0.35 µm	0.5 µm	0.18 µm	0.5 µm	65 nm	0.35 µm
Array size	128 × 128	144 × 144	132 × 124	256 × 256	96 × 96	32 × 32	4 × 64
Pixel size	15.4 µm × 15.4 µm	9.5 µm × 9.5 µm	20.1 µm × 20.1 µm	15 µm × 15 µm	-	60 µm × 72 µm	61.8 µm × 36.7 µm
Fill factor	28%	26%	42%	37%	17%	37%	18%
Photodetector	n+/p-sub	n-well/p-sub	n-well/p-sub	n-well/p-sub	n+/p-sub	p+/n-well/p-sub	n-well/p-sub
Pixel architecture	3T-based	CTIA	CTIA	CTIA	3T		CTIA
Read noise (mV_{rms})	-	1.9	0.82	3.1	2.5	-	1.9
Peak SNR (dB)	-	49	44	-	-	-	50
Frames rate (fps)	30	60	70	1500	-	20	67
Power supply (V)	3.3	3.3	3.3	-	5	-	3.3
Power per pixel (µW)	1.59	4.1	20.16	5.95 (with ADC)	7.59	8.06	0.32

Table 5.2. Comparison of CIS parameters for biomedical applications.

5.2 ASIC TESTING WITH LFIAS

The CIS was experimentally tested using LFIA strips. As mentioned in chapter 4 due to the size of the array of pixels and because no lenses or moving parts were used, the chip is able to only read in the detection pad the test line and some area around it, as shown in Figure 4.8. This reading area is sufficient to extract information regarding the concentration of analyte in the sample. At the same time it is less sensitive to position displacement errors due to the additional readings also performed around the nominal position of the test line.

Prior to tests the optimum setup was needed to be identified. Even though optimization was performed in chapter 3 for the second generation system, that setup is not applicable in the third generation reader. This is due to size differences between the CIS and the array of photodiodes. In the overall size of the CIS is included the carrier case (package) where the chip was wire bonded plus a socket where the carrier was placed. All this extra bulk increased the minimum distance between the LEDs and the pixel array influencing the performance of the system.

In a ray trace simulation program the array of pixels of the chip was modelled using 4 × 64 pixels with their exact dimensions. The LFIA was modelled as in chapter 3, with the optical surface properties of the strip again based on the results of the Imaging Sphere. The outside boundaries of the socket were simulated using same size rectangles. The LEDs were modelled as point sources and they were positioned next to the socket, see Figure 5.8 (a). As expected the light cannot reach the LFIA strip and thus no light is reflected in the array of photodiodes. Figure 5.8 (b) shows the simulated irradiance in the array of photodiodes, when the setup of Figure 5.8 (a) is used.

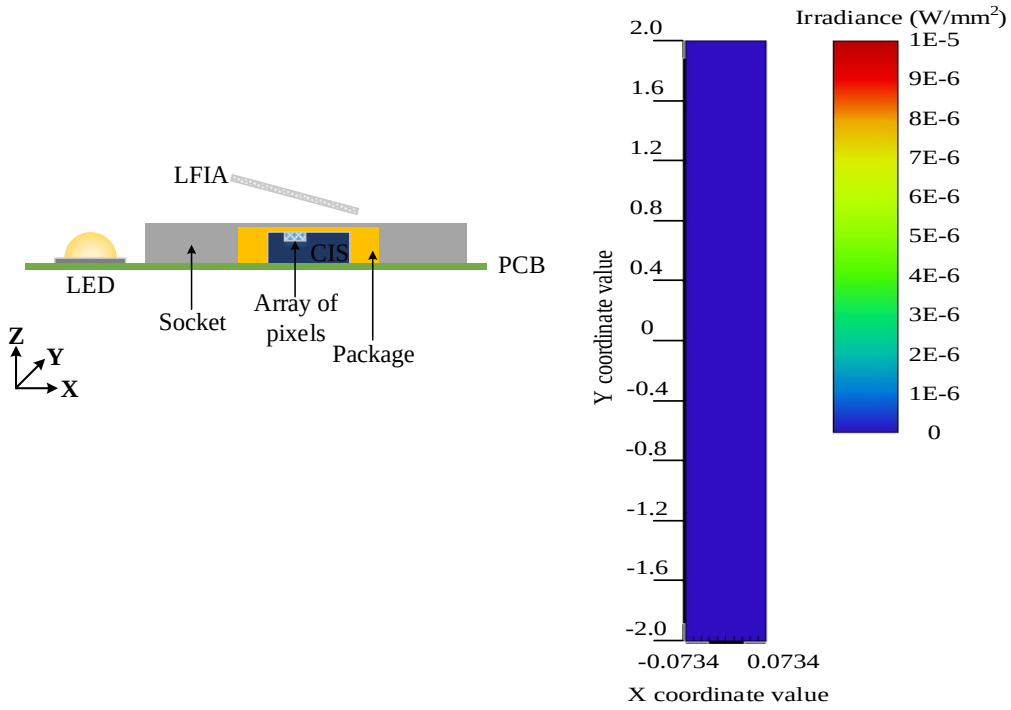

(a) (b)

Figure 5.8 (a) Simulated setup and (b) Irradiance across the array of pixels, its blue color indicates that it does not receive light, as it is interpreted from the color bar.

5.2.1 TEST SETUP

In order to overcome the problem with the LEDs being far away from the array of pixels the LEDs were placed along the Y-Z axis at 90 degrees in a separate PCB facing the chip direction as shown in Figure 5.9.

First the optimum number of LEDs required was determined to achieve uniform light distribution in the strip when there is no test line, while at the same time enough light is collected from the pixels. For the measurements the LFIA used had no test line and was divided into 4 areas, 1mm each. Then by changing the number of LEDs that were used to shine light in the LFIA from 1 to 3 two parameters were measured. The first was the light difference between the impinging light in the different areas of the LFIA as shown in Figure 5.10. This parameter shows how uniform the light is distributed in the LFIA. The other parameter was the average irradiance across all the pixels in the active area. The highest irradiance was achieved with 3 LEDs as shown in Figure 5.10. By combining these two parameters it was concluded that best

compromise was to use two LEDs in order to achieve relative good uniformity across the LFIA and good irradiance in the array of pixels.

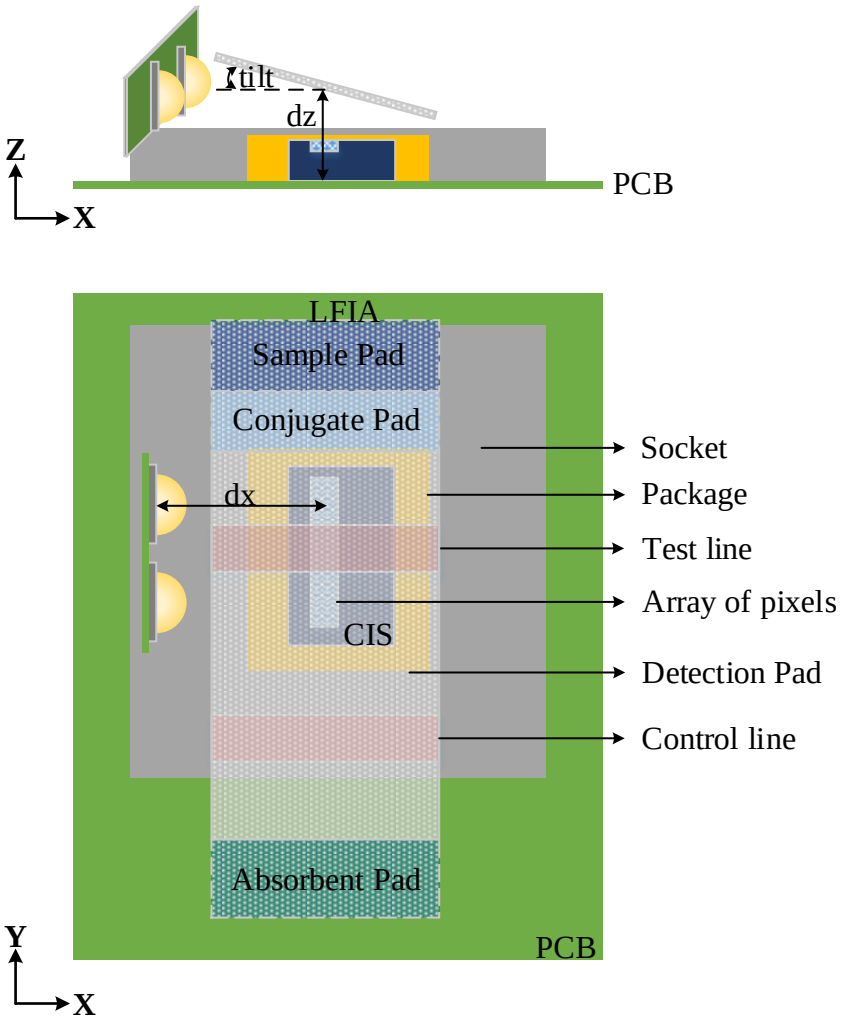

Figure 5.9 Simulation setup: plan and elevation (not to scale).

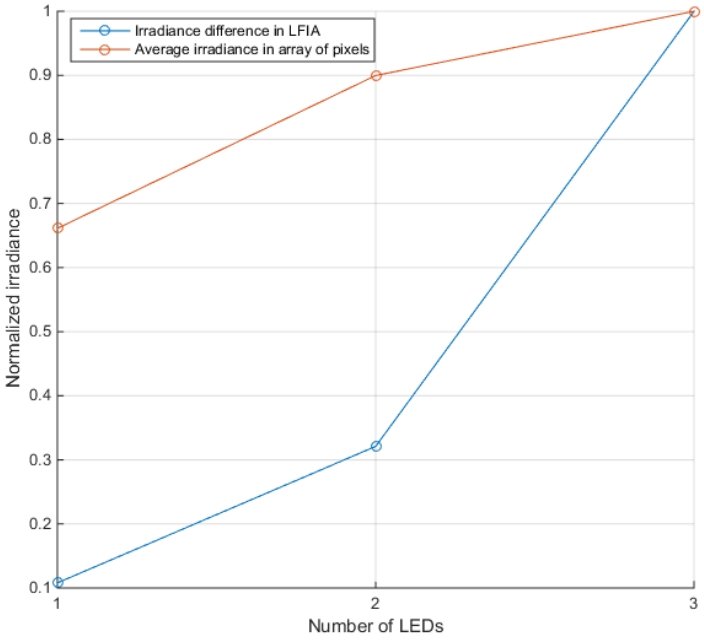

Figure 5.10 Measurements showing the irradiance difference across the different areas of the LFIA and the average irradiance collected from the pixels.

A parametric analysis was performed in order to define the optimum distance between the LEDs and the array of pixels in the *x* - axis. The position of the array of pixels and the LFIA were both fixed. The middle point of the test line faced the middle point of the array of pixels. In the measurements two LEDs were used. The dx distance is measured from the middle of the array of photodiodes, which is considered x = 0 to the middle of the LEDs.

For different *dx* distances the irradiance in the pixels was measured. Then the average irradiance for all 4 pixels of the same column was calculated. Figure 5.11 shows the normalized average irradiances in the array of pixels for difference *dx* distances. The low irradiance in the middle of the array of pixels is due to the test line. Around the line in the white parts of the LFIA the irradiance is expected to be high as in the Figure 5.11. The best results are for *dx* = 8.6 mm, because the irradiance difference between the white parts of LFIA and the test line is the highest. For dx lower than 6.6 mm the test line is not distinguishable due to most of the LEDs light impinges directly on the array of pixels, instead of first impinging in the LFIA and the reflected light hit the array of pixels. For *dx* higher than 8.6 mm the irradiance in the array of pixel is very small.

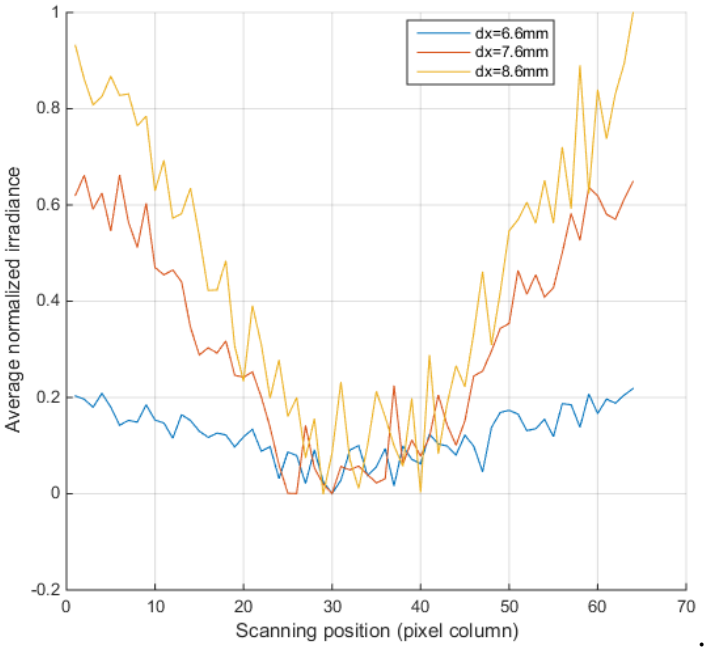

Figure 5.11 Normalized average irradiance across the array of pixels when the *dx* is varied.

Next the effect of the distance *dz* of the LFIA strip was measured together with the tilt of the strip as shown in Figure 5.9. Two LEDs were used to shine light in the LFIA, positioned 8.6 mm away from the array of pixels. The minimum distance that the LFIA could be positioned on top of the array of pixel is dictated by the size of the socket. Therefore at *dz* = 5 mm there is enough space for the strip to be tilted up to 10 degrees in *y* - axis. At *dz* = 6 mm there is enough space for the strip to be tilted up to 40 degrees in *y* - axis. For all these combinations the irradiance in the array of pixels was measured and the average irradiance of each column was calculated. Figure 5.12 (a) shows the normalized average irradiance of each scanning position for different *dx* distances and tilts. In all 5 positioning combinations the array of pixels can detect the test line successfully. This is evident with the drop of the irradiance in the middle of the pixels array. In *dz* values higher than 6 mm the irradiances in the array of pixels were much smaller than the irradiances shown in the Figure 5.12 (a).

The same experiment performed with the test line in the LFIA removed. Then the 4mm area of interest in the detection pad of the LFIA was divided into four distinct equal areas, 1 mm each. After, the position of the LFIA in y-axis and its tilt was varying the same pattern as before. The light hitting each area in the LFIA was measured and the maximum variation in irradiance per area (Δi) was calculated. Figure

5.12 (b) shows the normalized irradiance for each area in the detection pad. The smallest variation is measured for dz = 5 mm and a tilt of 10 degrees. Therefore in accounting for the results of the previous experiments the conclusion was that the dz = 5 mm and tilt 10 degrees was considered the best position for the LFIA.

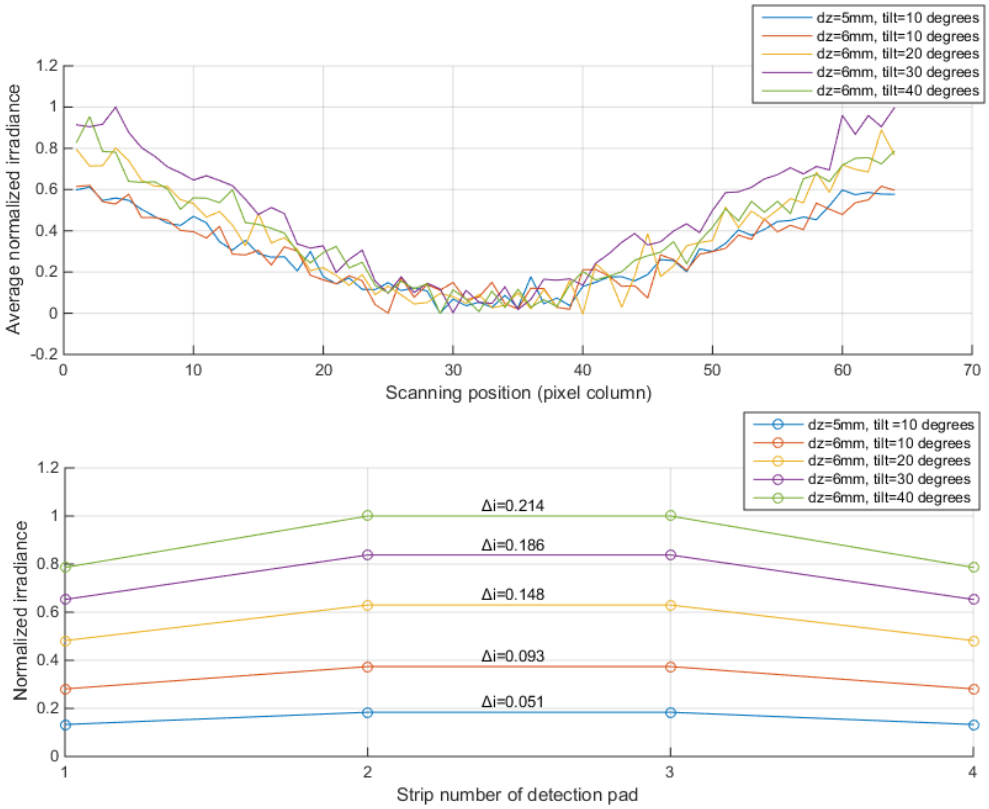

Figure 5.12 (a) Normalized average irradiance across the array of pixels when the LFIA's *dz* and tilt is varied. (b) Normalized irradiance in each of the four 1mm detection pad strips when the LFIA's dz and tilt is varied. The Δi indicated the variation in normalized irradiance of the 4 points of each measurement.

5.2.2 MEASUREMENTS

A 3D printed enclosure was designed and printed to isolate the system from ambient light. A special receptacle was designed which enabled the strip to be accurately placed above the chip with a 10 degree tilt to match the previous measured results. In the two sides of the enclosure two slits were made, in which the PCB with the LEDs was positioned. Figure (5.13a) shows the setup open during the insertion of the strip in the receptacle. Figure (5.13b) shows the receptacle inserted in its position and the lid of the reader closed.

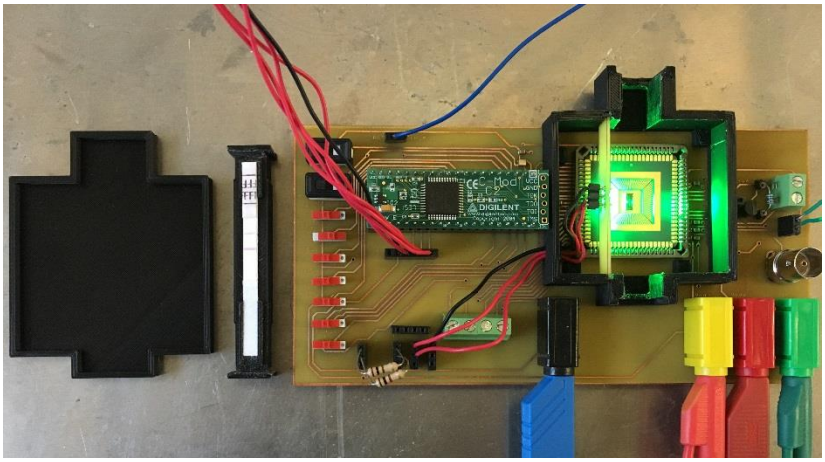

(a)

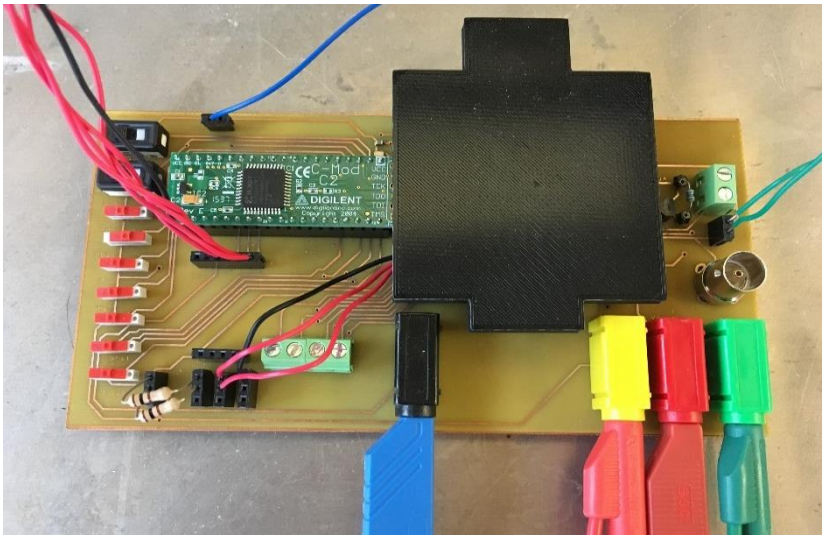

(b)

Figure 5.13 Photographs of the reader (a) the strip is placed in the receptacle and (b) the receptacle is positioned on top of the array of photodiodes and the reader lid closes.

The system was tested using LFIAs with influenza A nucleoprotein in saline buffer from 0.5ng/mL to 200ng/mL concentrations as shown in Figure 5.14.

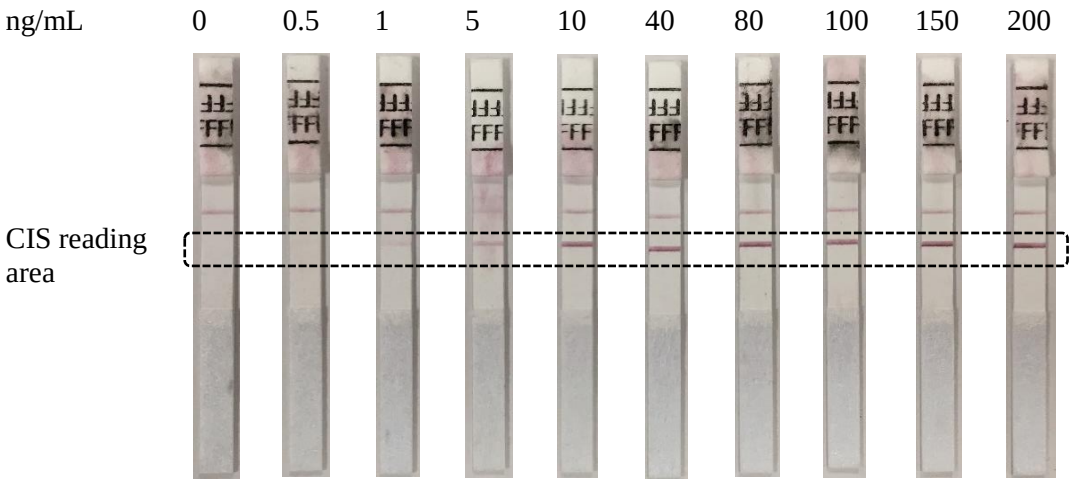

Figure 5.14. Photographs of the tested LFIAs in various concentrations of Influenza A nucleoprotein.

The measurements were based on the binning technique where all 4 pixels in the same column were binned. The integration time used is 50 μs and V_{DC} =2 V. The DAQ sampling frequency was 60 KHz. Therefore as in section 5.1 three samples were measured for every pixel's output. However only the middle samples were used in the calculations, in order to remove settling time effects. Each strip was measured ten times and the first frame of each measurement used in the calculations. Then background correction was performed using the averaged data from the ten measurements from a blank strip with 0 ng/mL concentration. The peak value was automatically detected and the average value of this maximum and the values of ±5 adjacent pixels were calculated (S_T). The signals from these 11 pixels were used because they receive most of the reflected light from the test line of the LFIA. Figure 5.15 shows the average signal from each strip when they are measured 10 times and the error bars indicate the standard deviation. The 4PL model was used for the generation of the fitted curve with R^2 = 0.986.The calculated parameters of Equation 3.1 are a = 3.81e-9, b = 0.39, c = 26.19, and d = 0.83.

The reader can distinguish the various concentrations of Influenza A nucleoprotein in LFIAs. The limit of detection is 0.5 ng/mL where the line is very faint. The cut-off signal which defines when there is no analyte in the sample has been calculated using the mean signal from the strip with 0 ng/mL concentration plus three times the standard deviation (3σ). The cut-off signal was 9.27 mV.

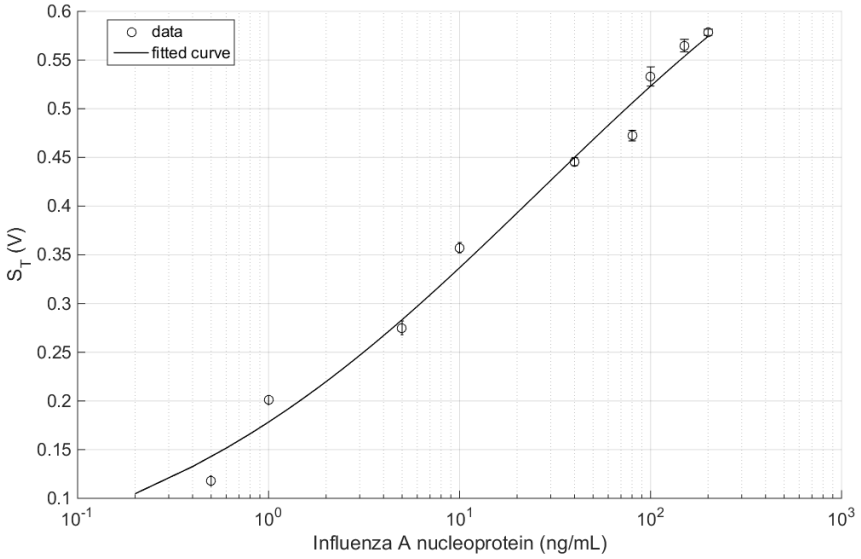

Figure 5.15 Measured S_T signal after background correction for various concentrations of Influenza A nucleoprotein using the CIS chip.

In table 5.3 a comparison between the discrete component array of photodiodes used in the first and second generation systems with the fabricated CIS is shown.

Parameter	Discrete component array of photodiodes	Proposed CMOS image sensor
Number of Pixels	1× 128	4 × 64
Pixel size	63.5 μm ×63.5 μm	61.8 μm ×36.7 μm
Power consumption	16.5 mW	0.021 mW
Limit of detection of Influenza A nucleoprotein	0.5 ng/mL	0.5 ng/mL*

* The actual limit of detection for Influenza A nucleoprotein in the proposed CIS is lower than 0.5ng/mL as it is explained in the paragraph below.

Table 5.3. Comparison of the photodetector used in the first and second generation systems with the proposed CMOS image sensor.

It is evident that the CIS (third generation system) has a reduced power consumption of 99.87% compared to the discrete component photodetector (second generation) and it can therefore perform significantly more measurements than the discrete component with the same battery. The limit of detection in both systems is 0.5 ng/mL. However, it should be noted that the CIS in reality can measure LFIA strips with much less concentration. This is evident from the two strips shown in Figure 5.16. The first strip was used in the tests for the second generation system and the second strip was used in the tests for the third generation system. As it can be visually observed, the test line intensity for the two strips is not the same (second line almost invisible), even though they have the same concentration of Influenza A nucleoprotein. This is because of the time difference between the two experiments. For the preparation of the test strips the same nucleoprotein antigen was used which is stored in a tube in the fridge. For every test set a portion of the antigen is taken from that tube and diluted according to the required concentration. However, because of the time difference between the two experiments the antigen was degraded. This could have happened partly due to time, but also due to contaminants being introduced and

break down the antigen. Every time the antigen is used there is a potential introduction of contamination.

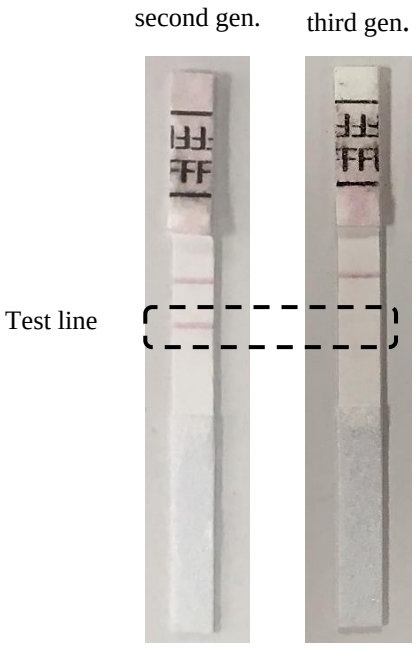

Figure 5.16 Photograph of the two test strips used in the second and third generation systems. Both have 0.5ng/mL concentration of Influenza A nucleoprotein but the color of their test lines is not comparable.

A comparison between the specifications of the three generation of systems presented in this thesis is shown in Table 5.4. All systems are considered to be low cost since only a limited amount of components are used. However due to the use of a specifically designed photodetector the third generation system can have low power consumption when in mass production. The power consumption of the three systems has progressively improved in each generation due to the number of LEDs required and to improvement in power consumption of the integrated CIS. All three systems are considered to be robust since no optical accessories and no moving parts were used. The results in the first generation system are considered to be moderately reproducible due to the relative high standard deviation in some measurements. This was improved in the second and third generation systems with the optimized designs and the use of the special carrier case for LFIA that holds it in a constant position in the system. All three systems have low positioning error because of the use of a stable array of photodiodes to scan the test line and some area around it.

Specification	First generation system	Second generation system	Third generation system
Cost	Low	Low	Low in mass production
Power	Medium	Low	Very low
Robustness	High	High	High
Reproducibility	Medium	High	High
Positioning error	Low	Low	Low

Table 5.4. Comparison table of the three generation of systems presented in this thesis.

5.3 DISCUSSION

In this chapter various test have been performed for the characterization of the developed CIS. Initially the setup required for the correct operation of the CIS was developed. Then using uniform light above the CIS and varying its irradiance the output voltage was measured. From these data multiple parameters were possible to be calculated which are used to characterize the performance of the CIS. Furthermore, the response of the CIS was measured for different integration times, with and without binning technique enabled. Next comparison performed between the proposed CIS and other CISs used in biomedical applications. In regards to noise performance and power consumption the reader has very good results comparable to other CISs.

Before the implementation of the reader, ray trace simulations performed to define the optimum position of the important components CIS, LEDs and LFIA. Then tests were implemented using LFIAs with Influenza A nucleoprotein in various concentrations. The results show that the reader was able to detect the different concentrations even when the test line was very faint.

5.4 CONCLUSION

In this chapter the performance of the CIS, and third generation system are presented. From the tests performed the following conclusions can be drawn:

- The CIS has very good performance in terms of noise and power consumption comparable with other CIS used for biomedical applications.
- Ray trace simulations are required for the optimum position of all the critical components because the same setup as in chapter 3 cannot be used. This is due to the overall size of the CIS including the chip, the package and the socket.
- When the CIS was tested with LFIAs with Influenza A nucleoprotein it was able to distinguish the different concentrations and had a lower limit of detection of 0.5ng/mL.

6

CONCLUSION

This thesis reports the work performed to investigate and develop novel systems for the quantification of analytes in LFIAs for POC. The work has focused on the implementation of a system based on a new method, the optimization of the system's performance based on ray trace simulation results and the design of a suitable photodetector. This thesis addresses various important limitations found in other systems, which make them unsuitable for POC testing or susceptible to erroneous results.

Infectious diseases cause death to millions of people every year. Especially in developing countries and resource limited settings where access to healthcare centres is very difficult. POC biosensors can help to identify, monitor and potentially minimize the spread of infectious diseases. LFIAs are biosensors that can be particularly useful for POC diagnostics due to their numerous advantages. However, for the quantification of the results in these biosensors an external electronic reader is required. The systems presented in this thesis have great potential as POC diagnostic devices.

The first step performed, was to investigate and compare other systems designed for POC applications and identify their limitations. The conclusion of this study was that important specifications are missing from these systems either altogether or partially making their possible adoption in the field of need very difficult. The specifications required for these systems are: low cost, low power, high robustness, high reproducibility and low positioning error.

The proposed system achieves all these specifications. It is based on the scanning method without the use of any moving parts and any optical accessories. In this way, the system is less susceptible to brake and therefore can be easily carried around in the field of need. Whereas with the implementation of the scanning method not just the test line in LFIAs is recorded but also some area around it making it less susceptible to positioning errors. The first system implemented as a proof of concept of the proposed method uses discrete components. As a light source, LEDs were used and as photodetector, an array of photodiodes was utilized. The system processes the measurements in a microcontroller and sends the results wirelessly to a smartphone via Bluetooth. Tests using LFIAs with influenza A nucleoprotein showed that the system can quantify the results, with limit of detection at 3ng/mL.

The second system developed is an optimized version of the first generation system. For its optimization, three important steps were required. The first step was to change the wavelength of the LEDs in the system to match the optical characteristics of the gold nanoparticles in the tested LFIAs. The second step was to model the optical profile of the surface of the LFIA, particularly the area of the test line and the area of the white part around the test line. An imaging sphere was used for this purpose, in which a light beam illuminated the surface under investigation in various angles and the scattered light was recorded in a camera. In this way, a BSDF model in tabular format was generated for the test line and the white part of the LFIA. In the third step of optimization a ray trace simulation program was used. In this program, the models of all the critical components (LEDs, array of photodiodes and LFIA) of the reader were simulated. The BSDF model developed was imported into the program for accurate simulations of the optical behavior of LFIAs. The main objective of the simulations was to increase the sensitivity of the system and derive the optimum number of LEDs required. It was achieved by finding the best position to place each component in order to have uniform light distribution in the LFIA and to have the highest light difference recorded by the array of photodiodes between the test line and the white parts around it. Based on the results from the simulations a second generation system was developed. It was built using discrete components and the same array of photodiodes as in the first generation system. A custom enclosure was fabricated using a 3D - printer, to protect the system from ambient light and to place the LFIA in the correct position. The performance of the device was validated using LFIAs with

influenza A nucleoprotein and SlpA in order to demonstrate the versatility of the system (detection of different analytes). Comparing the performances of the two systems the optimized second generation system has reduced power consumption by 62.5 %, because fewer LEDs were used. In addition, the limit of detection of the second system was improved from 3 ng/mL to 0.5 ng/mL.

Further improvement of the second generation system was performed by using a different photodetector than the photodetector used in the two previous systems. For that reason, and for first time a CIS was designed, fabricated and tested specifically for this application. The objective was to reduce power consumption and implement noise cancellation while having a miniaturised system. The CIS was designed in 0.35 μm CMOS technology. The photocurrent to voltage conversion was realised using the CTIA architecture. The offset FPN was reduced using a new compact design that reuses the same amplifier of the CTIA architecture in a feedback loop and therefore achieves low power consumption. All the transistors were biased in subthreshold using a 10 nA current for ultra low power reduction.

Tests were performed in the fabricated CIS in order to characterise its performance using varied irradiances impinging light on top of the image sensor. Then, the response from the chip was recorded and analysis of the results performed in order to calculate its operating range, the SNR and noise. Because no other chip has ever being designed specifically to be used in LFIA readers, the performance of the CIS was compared with other CIS designed for other biomedical applications. As it was shown in Table 5.2, the proposed CIS has the lowest pixel power consumption and comparable noise and SNR. The power consumption of the chip is 99.8% lower than that of the photodetector used in first and second generation systems. Ray trace simulations was performed to define a new test setup for LFIAs. This was necessary because the package and socket of the chip gave extra bulk to the developed CIS, compared to the array of photodiodes component used previously. From the results, a new setup was developed and tested with influenza A nucleoprotein LFIAs which showed that the system can perform successful quantification.

It should be noted that even though the focus of this thesis has been the development of readers for the detection and quantification of infectious diseases at the POC the same readers could be used for the detection and quantification of other

biomarkers. For example, there are LFIAs developed for the detection of hard attacked biomarkers, which require quantification and regular monitoring of the patient's health status. Therefore, systems such as the proposed reader could be widely used at home settings, for monitoring patient's health. These readers are required to have similar specifications as the readers for developing countries, namely: low cost, medium to low power, high robustness, high reproducibility and low positioning error.

6.1 FUTURE WORK

This section discusses strategies for improvement of the work presented in this thesis.

6.1.1 QUANTIFICATION MEASUREMENT TECHNIQUE

As described in this thesis the calculation of the S_T signal from the measurement of each LFIA strip can be performed using various methods. Mainly by using the data after background correction and calculating the S_T signal only or by calculating the S_T/S_C signal or by calculating the S_T in relation to the white part of the strip. Given that the strip is based on flexible material it can be easily bent or not placed correctly in the device resulting in change in the height between the strip and the detector which can also affect the results. Another source of error can be presented when the LFIA strips are tested with real human samples, which sometimes can result in staining and producing a yellowish color in the strip. In order to overcome these problems a solution is to measure the area generated from the rectangle at the test line instead of just measuring the minimum value at the test line, as shown in Figure 6.1.

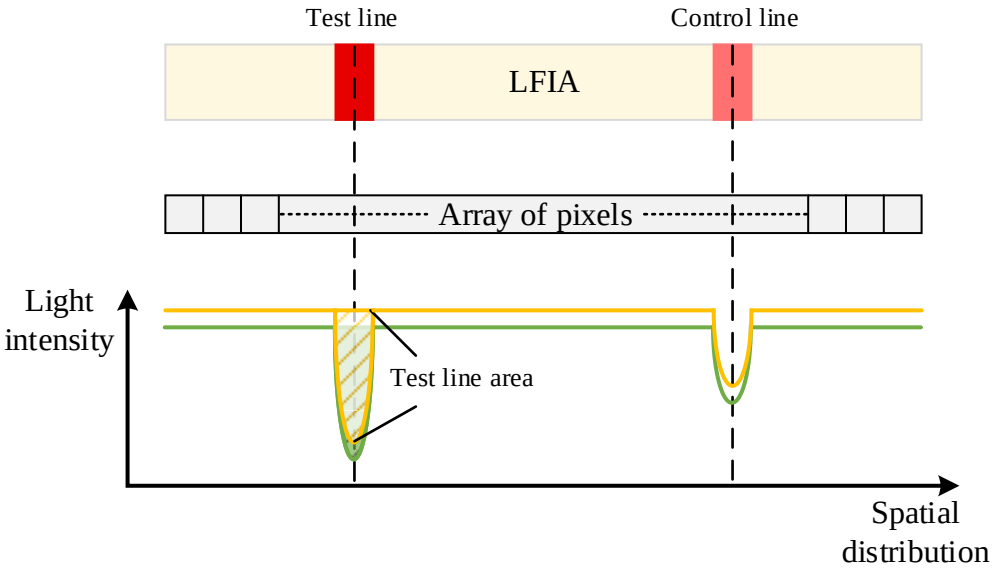

Figure 6.1 Schematic representation of the reflected light variation at the test and control lines for the same strip. The area for the test line valley is presented with the gradient color.

6.1.2 MODIFICATION OF THE SETUP OF THE THIRD GENERATION SYSTEM

In chapter 5 a setup for the tests of the CIS has been proposed, based on the ray trace simulation results. However, due to the large overall size of the CIS chip which includes the wire bonding case and the socket, the position of the LEDs was restricted. To overcome this problem the LEDs were positioned vertically across the pixels array of photodiodes in a different PCB. Two suggestions are proposed to overcome this problem for future designs:

a. Use a very small chip package and solder it directly on the PCB without the socket.
b. During the layout design place the pixel array close to one side of the chip and in the remaining sides place the wire bonding pads. Then the fabricated bare die should be wire bonded directly on the PCB.

When one of the above suggestions is realized the performance of the CIS can be improved as it is demonstrated from the following ray trace analysis. For the simulation a setup was used similar to the setup of the second generation system. Two

LEDs were positioned on the same PCB as in the CIS chip. The LFIA was placed on top of the array of pixels with a10 degree tilt along the Y-axis, as shown in Figure 6.2.

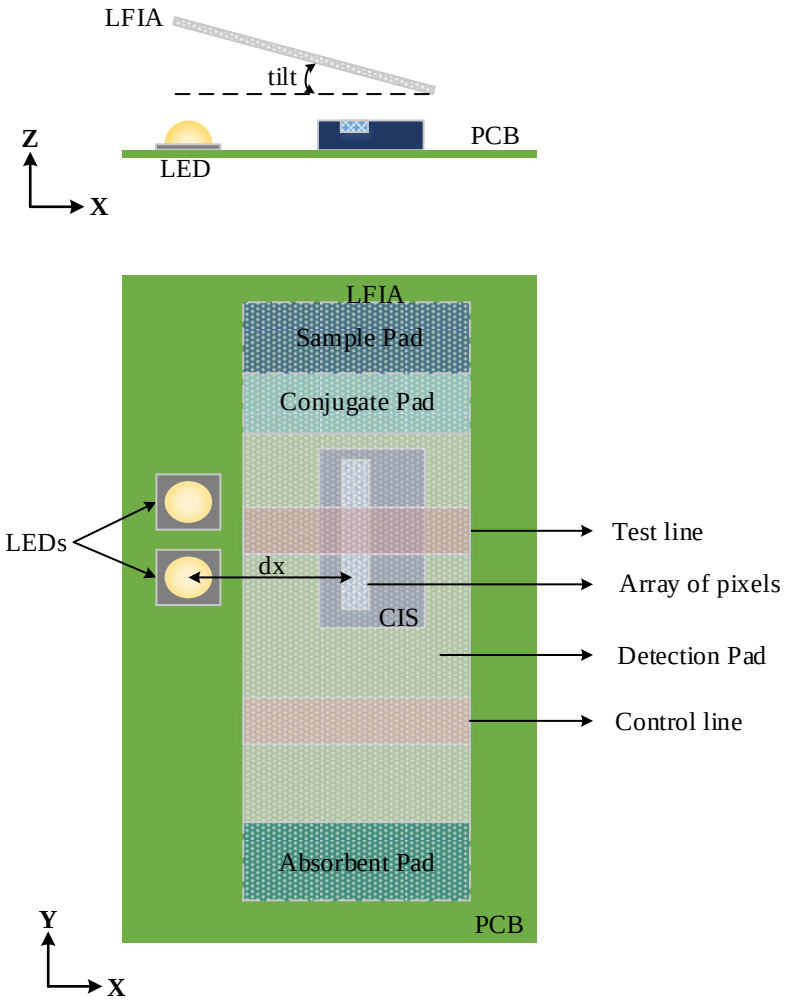

Figure 6.2 Simulation setup: plan and elevation (not to scale)

The irradiance in the array of pixels was measured for increasing dx distances between the middle point of the LEDs and the middle point of the photodiodes in the array of CIS in x-axis. The results are plotted and compared with the results from the final setup used in chapter 5, as shown in Figure 6.3. The best result, is when the test line has the highest irradiance difference with the white part of the paper. As shown in Figure 6.3 this is valid for dx = 3mm. As the dx distance reduces the test line becomes less and less distinguishable. The irradiance from the setup used in chapter 5 to measure the concentration of Influenza A nucleoprotein in LFIA was simulated and is indicated in the legend as LEDs vertically. The overall size of the CIS influences

the position of the LEDs, which also affect the overall sensitivity of the system. With the adoption of one of the proposed suggestions in the setup, the system will be more sensitive and able to detect better the test line in LFIAs.

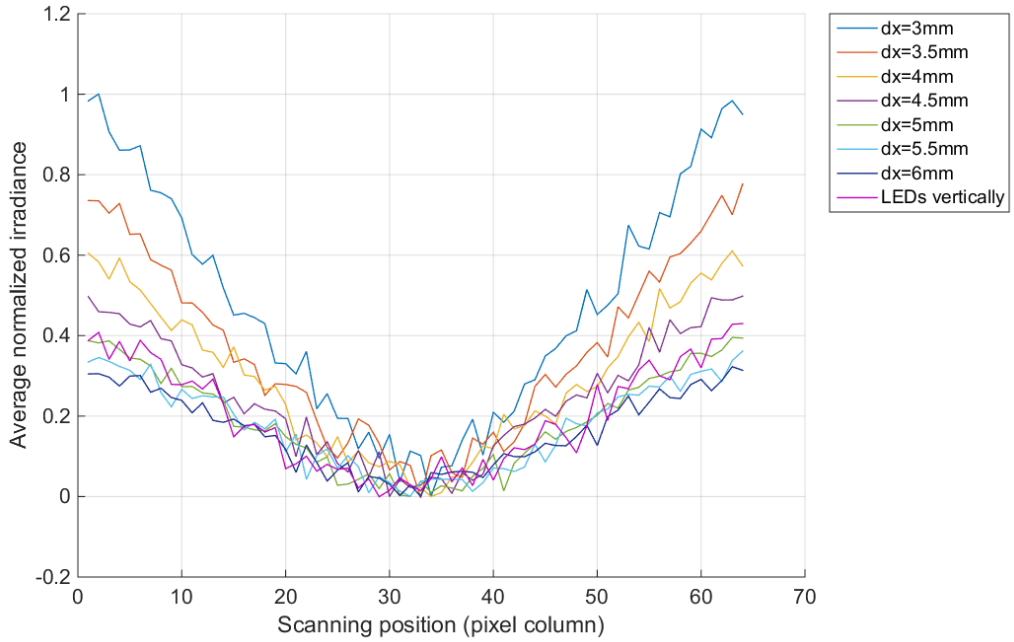

Figure 6.3 Normalized average irradiance across the array of pixels when the *dx* is varied. The LED vertically indicates the simulation measurement performed for the final test setup in chapter 5.

6.1.3 Improvement of the Addressing Method Used in the CMOS Image Sensor

The addressing method adopted in this design is performed mainly inside the chip and the testing designer does not have much flexibility during the chip testing. For example the selection of a specific pixel and the measure of its output, with the proposed design it cannot be performed. Instead, the output of the entire row of pixels must first be read and then the output of the pixel under investigation can be defined. A solution to this problem is to remove the shift register used in this design and instead use a demultiplexer, which will enable the control of each counter of each column using external pulses.

6.1.4 MINIATURIZATION

The proposed CIS consists only a first step towards the miniaturization of the readout system. Future developments in this direction could include the on chip control logic that will generate all the signals required for the operation of the chip and therefore replace the CPLD used in the existing tests, as well as include an on-chip ADC.

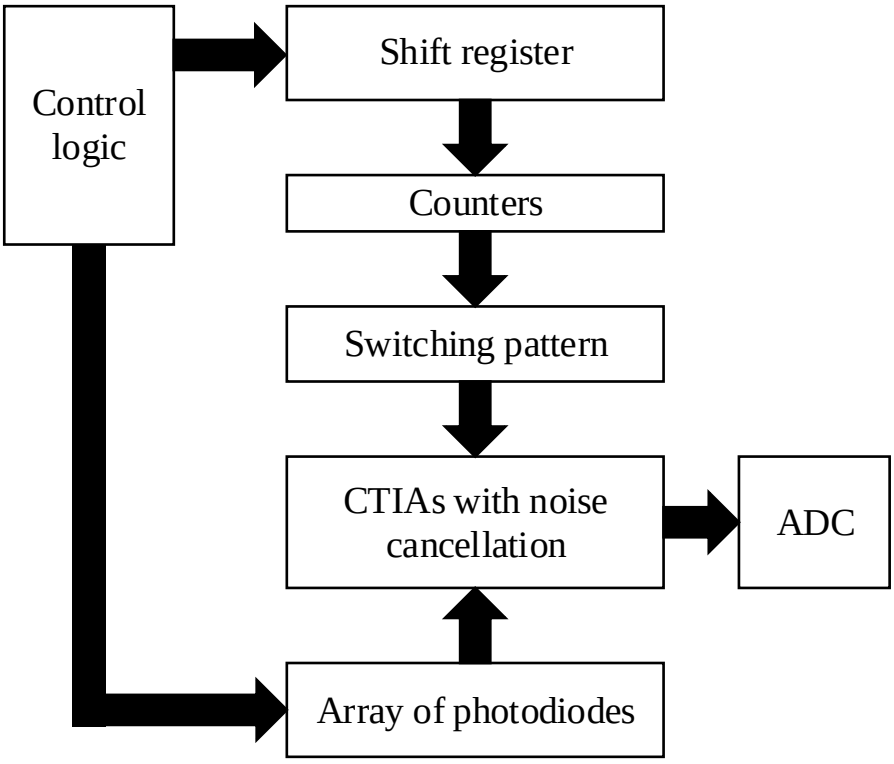

Figure 6.4 CIS architecture with on chip control logic and ADC.

Further miniaturization and power reduction of the system can be achieved with the use of μLEDs (microLEDs) on chip instead of conventional LEDs. However, the difficulty in realizing this system lies in the fabrication process. The μLEDs cannot be fabricated in a standard CMOS technology and extra processing techniques are needed [101], [102]. This can significantly increase the design complexity and the cost of the developed chip especially at the prototype level. However, in multi-production level the overall cost of the chip can be significantly reduced.

In addition, the proposed cascode current mirror (Figure 4.11) used for the generation of biasing voltages for the amplifier could be modified to consume less

space, especially if in future designs the amplifier needs to be part of the pixels architecture. A possible modification is to have one cascode current mirror outside the pixel copying the required voltages and connect with tracts these voltages to the amplifier as shown in Figure 6.5. However, advanced layout techniques need to be realised in this design to avoid mismatch errors.

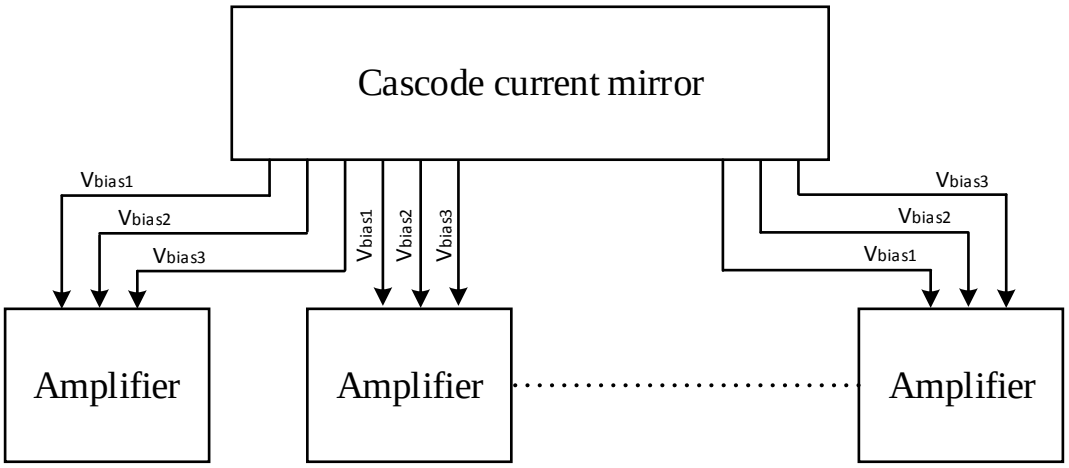

Figure 6.5 CIS architecture with on chip control logic and ADC.

A

FUNDAMENTAL EQUATIONS OF MOSFETS

CMOS technology is based on the metal-oxide-silicon field-effect transistors (MOSFETs) and is considered the most popular IC fabrication technology. The operation of MOSFETs is mainly defined from the overdrive voltage (V_{ov}), which is equal to gate source voltage minus the threshold voltage, $|V_{ov}| \equiv |V_{GS}| - |V_{th}|$. This is because while the gate voltage (V_G), increases a depletion layer is formed under the gate oxide. With sufficient enough V_G charges flow from source to drain and the transistor turns on [87].

When the drain-source voltage is less than the overdrive voltage ($V_{DS} < V_{GS} - V_{th}$), the MOS transistor operate in triode region/linear region, with a drain current equal to:

$$I_D = \beta \left[(V_{GS} - V_{th}) V_{DS} - \frac{1}{2} V_{DS}^2 \right] \tag{A.1}$$

Where $\beta = \mu C_{ox} \frac{W}{L}$ and μ is the mobility factor, C_{ox} is the gate oxide capacitor per unit area, *W* and *L* are the width and length of the MOS device.

For $V_{DS} \ll 2(V_{GS} - V_{th})$, the MOS transistor operates in deep triode region and the drain current in is approximately equal to:

$$I_D = \beta(V_{GS} - V_{th})V_{DS} \tag{A.2}$$

In this region, the I_D changes linearly with the V_{DS} and the MOS transistor can be represented as a resistor from source to drain with resistance equal to:

$$R_{on} = \frac{1}{\beta(V_{GS} - V_{th})} \tag{A.3}$$

For $V_{DS} > V_{GS} - V_{th}$, the I_D is almost constant and the MOS operates in saturation region, where the drain current is equal to:

$$I_D = \frac{1}{2}\beta(V_{GS} - V_{th})^2 \tag{A.4}$$

In this region the I_D is almost independent of the V_{DS} of the MOS transistor and the input voltage is converted to output current. The figure of merit indicating this conversion is called transconductance and is equal to:

$$g_m = \left[\frac{\partial I_D}{\partial V_{GS}}\right]_{V_{DS,const.}} = \beta(V_{GS} - V_{th}) \tag{A.5}$$

$$g_m = \sqrt{2\beta I_D} \tag{A.6}$$

Channel-length modulation is a second order effect in which the actual length between the source and gate depends on V_{DS}, therefore in saturation the drain current is Equal to:

$$I_D = \frac{1}{2}\beta(V_{GS} - V_{th})^2\,(1 + \lambda V_{DS}) \tag{A.7}$$

Where λ is the channel length modulation coefficient and characterise the changes in length for given changes in V_{DS}, For increased L the λ becomes smaller. The transconductance changes to:

$$g_m = \beta(V_{GS} - V_{th})(1 + \lambda V_{DS}) \tag{A.8}$$

The output resistance in saturation instead of infinite is equal to:

$$r_o = \frac{1}{\frac{\partial I_D}{\partial V_{DS}}} = \frac{1}{\frac{1}{2}\beta(V_{GS} - V_{th})^2\lambda} \approx \frac{1}{\lambda I_D} \tag{A.9}$$

When the gate-source voltage is less than the threshold voltages ($V_{GS} < V_{th} - 100mV$) [103] the MOSFET operates in weak inversion (subthreshold) with some current still flowing from drain to source. In the saturation region of weak inversion the drain current is exponentially dependent of the of the V_{GS} [87] as shown in Equation A.10 and Figure A.1. Figure A.2 shown the triode and saturation region of a transistor operating in weak inversion.

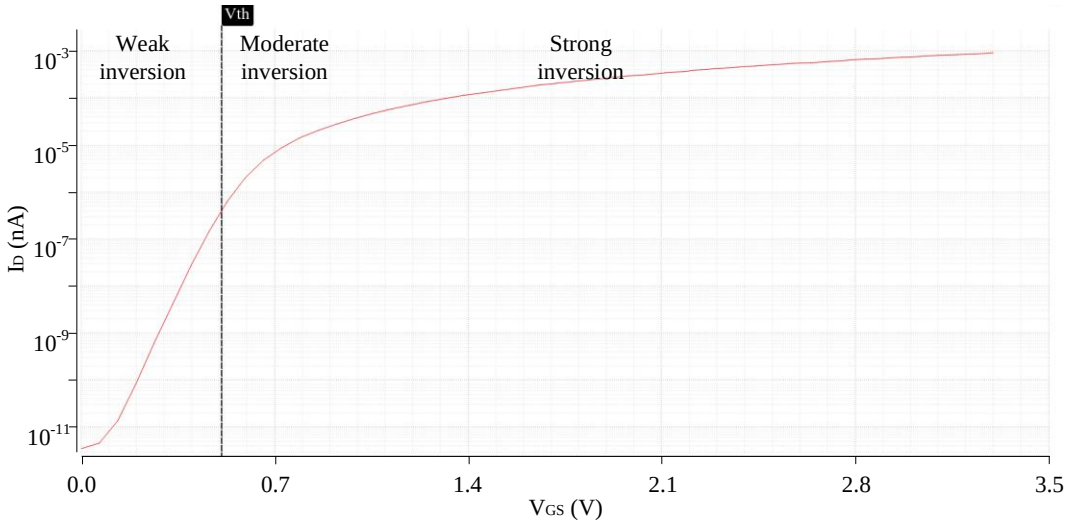

Figure A.1 I_D versus V_{GS} of a MOS transistor.

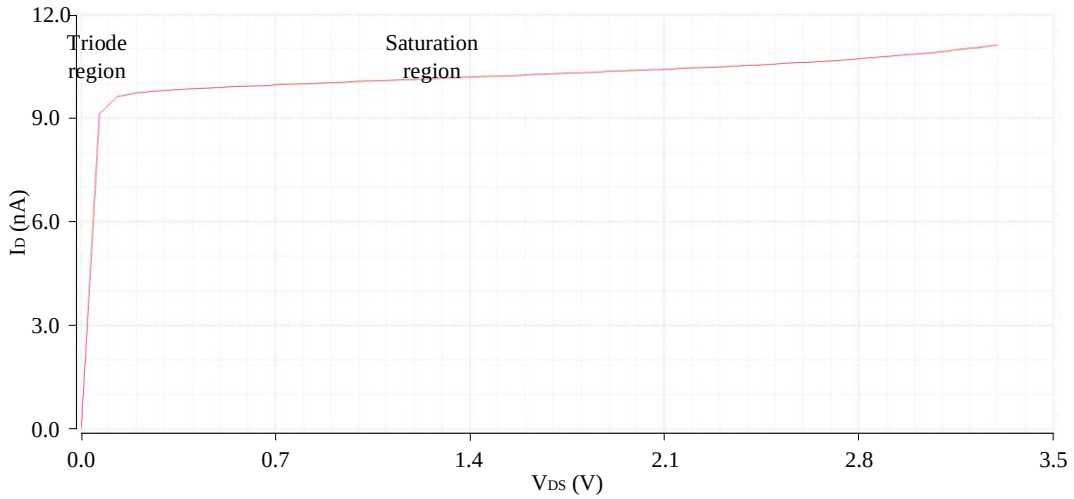

Figure A.2 I_D versus V_{DS} of a MOS transistor.

$$I_D = I_{D0} \cdot exp\left(\frac{V_G - V_s}{nU_T}\right) \tag{A.10}$$

Where $U_T = \frac{kT}{q} \cong 26mV$, is the thermal voltage at room temperature, n is a slope factor dependent on the process parameter and is calculated as $n = \frac{C_{ox}+C_{depl}}{C_{ox}} \cong 1.2 - 1.6$, where C_{ox} is the gate oxide capacitor and C_{depl} is the depletion region capacitor. I_{D0} is the leakage current and is (drain current that flows in saturation when gate voltage is set to zero) [104] and is defined as:

$$I_{D0} = I_{spec} \cdot exp\left(-\frac{V_{th}}{nU_T}\right), for\ V_{DS} > 100mV \tag{A.11}$$

Where I_{spec} is the specific current and is equal to $I_{spec} = 2n\beta U_T^2$.

The inversion coefficient IC can be used to define the different regions of operation in saturation of the transistor as:

$$IC < 0.1: weak\ inversion$$

$$0.1 < IC < 10: moderate\ inversion$$

$$10 < IC: strong\ inversion$$

Where $IC = \frac{I_D}{I_{spec}}$

The transconductance in weak inversion is:

$$g_m = \frac{I_D}{n \cdot U_T} \tag{A.12}$$

BIBLIOGRAPHY

[1] "World Health Organization / Infectious diseases." [Online]. Available: http://www.who.int/topics/infectious_diseases/en/. [Accessed: 09-Dec-2017].

[2] M. L. Sin, K. E. Mach, P. K. Wong, and J. C. Liao, "Advances and challenges in biosensor-based diagnosis of infectious diseases," *Expert Rev. Mol. Diagn.*, vol. 14, no. 2, pp. 225–244, Mar. 2014.

[3] PKIDs, "Introduction to infectious diseases," 2008. [Online]. Available: http://www.pkids.org/files/pdf/idw/text1.pdf. [Accessed: 14-Jun-2018].

[4] R. Detels, "Epidemiology Course notes." [Online]. Available: http://www.ph.ucla.edu/epi/faculty/detels/Epi220/Detels_Agents.pdf. [Accessed: 09-Jun-2018].

[5] D. L. Kasper and A. S. Fauci, *Harrison's Infectious Diseases*. The McGraw-Hill Companies, 2010.

[6] K. E. Nelson and C. F. Williams, *Early History of Infectious Disease*. Jones and Bartlett Publishers, 2007.

[7] K. C. Hazen, "Diagnosis of Infectious Disease." [Online]. Available: https://www.msdmanuals.com/en-gb/home/infections/diagnosis-of-infectious-disease/diagnosis-of-infectious-disease. [Accessed: 14-Jun-2018].

[8] A. M. Caliendo, D. N. Gilbert, C. C. Ginocchio, K. E. Hanson, L. May, T. C. Quinn, F. C. Tenover, D. Alland, A. J. Blaschke, R. A. Bonomo, K. C. Carroll, M. J. Ferraro, L. R. Hirschhorn, W. P. Joseph, T. Karchmer, A. T. MacIntyre, L. B. Reller, and A. F. Jackson, "Better Tests, Better Care: Improved Diagnostics for Infectious Diseases," *Clin. Infect. Dis.*, vol. 57, no. suppl 3, pp. S139–S170, Dec. 2013.

[9] M. Tonolla, C. Benagli, and S. De, "Mass spectrometry in the diagnostic laboratory," *Pipette*, no. 3, pp. 20–25, 2009.

[10] C. Dye, "After 2015: infectious diseases in a new era of health and development," *Philos. Trans. R. Soc. B Biol. Sci.*, vol. 369, no. 1645, pp.

20130426–20130426, May 2014.

[11] P. Howitt, A. Darzi, G.-Z. Yang, H. Ashrafian, R. Atun, J. Barlow, A. Blakemore, A. M. Bull, J. Car, L. Conteh, G. S. Cooke, N. Ford, S. A. Gregson, K. Kerr, D. King, M. Kulendran, R. a Malkin, A. Majeed, S. Matlin, R. Merrifield, H. a Penfold, S. D. Reid, P. C. Smith, M. M. Stevens, M. R. Templeton, C. Vincent, and E. Wilson, "Technologies for global health," *Lancet*, vol. 380, no. 9840, pp. 507–535, Aug. 2012.

[12] "Global Health Observatory data," *World Health Organization*. [Online]. Available: http://www.who.int/gho/mortality_burden_disease/causes_death/top_10/en/. [Accessed: 15-Jun-2016].

[13] C. P. Chan, Y. Cheung, R. Renneberg, and M. Seydack, *Biosensing for the 21st Century*, vol. 109. Berlin, Heidelberg: Springer Berlin Heidelberg, 2008.

[14] N. J. Ronkainen, H. B. Halsall, and W. R. Heineman, "Electrochemical biosensors," *Chem. Soc. Rev.*, vol. 39, no. 5, p. 1747, 2010.

[15] K. Shavanova, Y. Bakakina, I. Burkova, I. Shtepliuk, R. Viter, A. Ubelis, V. Beni, N. Starodub, R. Yakimova, and V. Khranovskyy, "Application of 2D Non-Graphene Materials and 2D Oxide Nanostructures for Biosensing Technology," *Sensors*, vol. 16, no. 2, p. 223, Feb. 2016.

[16] M. L. Sin, K. E. Mach, P. K. Wong, and J. C. Liao, "Advances and challenges in biosensor-based diagnosis of infectious diseases," *Expert Rev. Mol. Diagn.*, vol. 14, no. 2, pp. 225–244, Mar. 2014.

[17] J. K. Taubenberger and D. M. Morens, "The Pathology of Influenza Virus Infections," *Annu. Rev. Pathol. Mech. Dis.*, vol. 3, no. 1, pp. 499–522, Feb. 2008.

[18] A. Blut, "Influenza Virus," *Transfus. Med. Hemotherapy*, vol. 36, no. 1, pp. 32–39, 2009.

[19] S. Vemula, J. Zhao, J. Liu, X. Wang, S. Biswas, and I. Hewlett, "Current Approaches for Diagnosis of Influenza Virus Infections in Humans," *Viruses*, vol. 8, no. 4, p. 96, Apr. 2016.

[20] R. G. Webster, A. S. Monto, T. J. Braciale, and R. A. Lamb, Eds., *Textbook of*

Influenza, Second. John Wiley & Sons, Ltd, 2013.

[21] V. Racaniello, "Structure of influenza virus," 2009. [Online]. Available: http://www.virology.ws/2009/04/30/structure-of-influenza-virus/. [Accessed: 26-Jun-2018].

[22] J. H. C. M. Kreijtz, R. A. M. Fouchier, and G. F. Rimmelzwaan, "Immune responses to influenza virus infection," *Virus Res.*, vol. 162, no. 1–2, pp. 19–30, Dec. 2011.

[23] Z. Staneková and E. Varečková, "Conserved epitopes of influenza A virus inducing protective immunity and their prospects for universal vaccine development," *Virol. J.*, vol. 7, no. 1, p. 351, 2010.

[24] D. R. Peaper and M. L. Landry, "Rapid Diagnosis of Influenza," *Clin. Lab. Med.*, vol. 34, no. 2, pp. 365–385, Jun. 2014.

[25] T. Acharya, "Hemagglutination Inhibition Test (HAI): Principle, procedure, result and interpretations," *Microbe Online*, 2014. [Online]. Available: https://microbeonline.com/hemagglutination-inhibition-test-hai-principle-procedure-result-interpretations/.

[26] E. W. Nery and L. T. Kubota, "Sensing approaches on paper-based devices: a review," *Anal. Bioanal. Chem.*, vol. 405, no. 24, pp. 7573–7595, Sep. 2013.

[27] C. Parolo, M. Medina-Sánchez, A. de la Escosura-Muñiz, and A. Merkoçi, "Simple paper architecture modifications lead to enhanced sensitivity in nanoparticle based lateral flow immunoassays," *Lab Chip*, vol. 13, no. 3, pp. 386–390, Feb. 2013.

[28] P. O. Gubbins, M. E. Klepser, A. M. Dering-Anderson, K. A. Bauer, K. M. Darin, S. Klepser, K. R. Matthias, and K. Scarsi, "Point-of-care testing for infectious diseases: Opportunities, barriers, and considerations in community pharmacy," *J. Am. Pharm. Assoc.*, vol. 54, no. 2, pp. 163–171, Mar. 2014.

[29] L. Bissonnette and M. G. Bergeron, "Diagnosing infections—current and anticipated technologies for point-of-care diagnostics and home-based testing," *Clin. Microbiol. Infect.*, vol. 16, no. 8, pp. 1044–1053, Aug. 2010.

[30] E. Pilavaki, C. Parolo, R. McKendry, and A. Demosthenous, "Wireless paper-

based biosensor reader for the detection of infectious diseases at the point of care," in *2016 IEEE SENSORS*, 2016, vol. 13, no. 12, pp. 1–3.

[31] C. Parolo and A. Merkoçi, "Paper-based nanobiosensors for diagnostics," *Chem. Soc. Rev.*, vol. 42, no. 2, pp. 450–457, Jan. 2013.

[32] E. Pilavaki and A. Demosthenous, "Optimized Lateral Flow Immunoassay Reader for the Detection of Infectious Diseases in Developing Countries," *Sensors*, vol. 17, no. 11, p. 2673, Nov. 2017.

[33] A. de la Escosura-Muñiz, C. Parolo, and A. Merkoçi, "Immunosensing using nanoparticles," *Mater. Today*, vol. 13, no. 7–8, pp. 24–34, Jul. 2010.

[34] K. M. Koczula and A. Gallotta, "Lateral flow assays," *Essays Biochem.*, vol. 60, no. 1, pp. 111–120, Jun. 2016.

[35] M. E. Koivunen and R. L. Krogsrud, "Principles of Immunochemical Techniques Used in Clinical Laboratories," *Lab. Med.*, vol. 37, no. 8, pp. 490–497, Aug. 2006.

[36] R. Wong and H. Tse, *Lateral Flow Immunoassay*. Totowa, NJ: Humana Press, 2009.

[37] E. Pilavaki, V. Valente, W. Serdijn, and A. Demosthenous, "Compact pixel architecture for CMOS lateral flow immunoassay readout systems," in *2017 13th Conference on Ph.D. Research in Microelectronics and Electronics (PRIME)*, 2017, pp. 313–316.

[38] D. D. Liana, B. Raguse, J. J. Gooding, and E. Chow, "Recent Advances in Paper-Based Sensors," *Sensors*, vol. 12, no. 9, pp. 11505–11526, Aug. 2012.

[39] E. B. Bahadır and M. K. Sezgintürk, "Lateral flow assays: Principles, designs and labels," *TrAC Trends Anal. Chem.*, vol. 82, pp. 286–306, Sep. 2016.

[40] T. R. Kozel and A. R. Burnham-Marusich, "Point-of-Care Testing for Infectious Diseases: Past, Present, and Future," *J. Clin. Microbiol.*, vol. 55, no. 8, pp. 2313–2320, Aug. 2017.

[41] D. Quesada-González and A. Merkoçi, "Nanoparticle-based lateral flow biosensors," *Biosens. Bioelectron.*, vol. 73, pp. 47–63, Nov. 2015.

[42] Merck, “Gold Nanoparticles: Properties and Applications.” [Online]. Available: https://www.sigmaaldrich.com/technical-documents/articles/materials-science/nanomaterials/gold-nanoparticles.html.

[43] Cytodiagnostics, “Introduction to gold nanoparticle characterization.” [Online]. Available: http://www.cytodiagnostics.com/store/pc/Introduction-to-Gold-Nanoparticle-Characterization-d3.htm. [Accessed: 25-Jul-2016].

[44] S. Eustis and M. A. El-Sayed, “Why gold nanoparticles are more precious than pretty gold: Noble metal surface plasmon resonance and its enhancement of the radiative and nonradiative properties of nanocrystals of different shapes,” *Chem. Soc. Rev.*, vol. 35, no. 3, pp. 209–217, 2006.

[45] M. Cordeiro, F. Ferreira Carlos, P. Pedrosa, A. Lopez, and P. Baptista, “Gold Nanoparticles for Diagnostics: Advances towards Points of Care,” *Diagnostics*, vol. 6, no. 4, p. 43, Nov. 2016.

[46] Y. Li, H. J. Schluesener, and S. Xu, “Gold nanoparticle-based biosensors,” *Gold Bull.*, vol. 43, no. 1, pp. 29–41, 2010.

[47] A. K. Yetisen, M. S. Akram, and C. R. Lowe, “Paper-based microfluidic point-of-care diagnostic devices,” *Lab Chip*, vol. 13, no. 12, p. 2210, Jun. 2013.

[48] J. C. Contreras-Naranjo, Q. Wei, and A. Ozcan, “Mobile Phone-Based Microscopy, Sensing, and Diagnostics,” *IEEE J. Sel. Top. Quantum Electron.*, vol. 22, no. 3, pp. 1–14, May 2016.

[49] D.-S. Lee, B. G. Jeon, C. Ihm, J.-K. Park, and M. Y. Jung, “A simple and smart telemedicine device for developing regions: a pocket-sized colorimetric reader,” *Lab Chip*, vol. 11, no. 1, pp. 120–126, Jan. 2011.

[50] L. Huang, L. Zhou, Y. Zhang, C. Xie, J. Qu, A. Zeng, H. Huang, R. Yang, and X. Wang, “A Simple Optical Reader for Upconverting Phosphor Particles Captured on Lateral Flow Strip,” *IEEE Sens. J.*, vol. 9, no. 10, pp. 1185–1191, Oct. 2009.

[51] A. Carrio, C. Sampedro, J. Sanchez-Lopez, M. Pimienta, and P. Campoy, “Automated Low-Cost Smartphone-Based Lateral Flow Saliva Test Reader for Drugs-of-Abuse Detection,” *Sensors*, vol. 15, no. 11, pp. 29569–29593, Nov.

2015.

[52] O. Mudanyali, S. Dimitrov, U. Sikora, S. Padmanabhan, I. Navruz, and A. Ozcan, “Integrated rapid-diagnostic-test reader platform on a cellphone,” *Lab Chip*, vol. 12, no. 15, p. 2678, 2012.

[53] C. Li, K. Vandenberg, S. Prabhulkar, X. Zhu, L. Schneper, K. Methee, C. J. Rosser, and E. Almeide, “Paper based point-of-care testing disc for multiplex whole cell bacteria analysis,” *Biosens. Bioelectron.*, vol. 26, no. 11, pp. 4342–4348, Jul. 2011.

[54] A. K. Ellerbee, S. T. Phillips, A. C. Siegel, K. A. Mirica, A. W. Martinez, P. Striehl, N. Jain, M. Prentiss, and G. M. Whitesides, “Quantifying Colorimetric Assays in Paper-Based Microfluidic Devices by Measuring the Transmission of Light through Paper,” *Anal. Chem.*, vol. 81, no. 20, pp. 8447–8452, Oct. 2009.

[55] Abbott, “Alere Reader.” [Online]. Available: https://www.alere.com/en/home/product-details/alere-reader.html. [Accessed: 17-Jul-2018].

[56] BioAssay Works, “Multiple line reader.” [Online]. Available: https://bioassayworks.com/?product=multiple-line-reader. [Accessed: 17-Jul-2018].

[57] C. A. Holstein, M. Griffin, J. Hong, and P. D. Sampson, “Statistical Method for Determining and Comparing Limits of Detection of Bioassays,” *Anal. Chem.*, vol. 87, no. 19, pp. 9795–9801, Oct. 2015.

[58] G. Jones, M. Wortberg, S. B. Kreissig, D. S. Bunch, S. J. Gee, B. D. Hammock, and D. M. Rocke, “Extension of the four-parameter logistic model for ELISA to multianalyte analysis,” *J. Immunol. Methods*, vol. 177, no. 1–2, pp. 1–7, Dec. 1994.

[59] The Pennsylvania State University, “The coefficient of determination, r-squared.” [Online]. Available: https://onlinecourses.science.psu.edu/stat501/node/255/. [Accessed: 04-Aug-2018].

[60] “Application of Imaging Sphere for BSDF Measurements of Arbitrary

Materials." [Online]. Available: http://www.radiantvisionsystems.com/sites/default/files/library-documents/Learn.WP_.RVS Application of Imaging Sphere for BSDF WP20141219.pdf. [Accessed: 10-Oct-2017].

[61] C. Asmail, "Bidirectional scattering distribution function (BSDF): A systematized bibliography," *J. Res. Natl. Inst. Stand. Technol.*, vol. 96, no. 2, p. 215, Mar. 1991.

[62] Y.-W. Yu, Y.-L. Chen, W.-H. Chen, H.-X. Chen, X.-H. Lee, C.-C. Lin, and C.-C. Sun, "Bidirectional scattering distribution function by screen imaging synthesis," *Opt. Express*, vol. 20, no. 2, p. 1268, Jan. 2012.

[63] S. Marschner, "CS667 Lecture Notes: Scattering," *Cornell University*, no. February. pp. 1–8, 2012.

[64] H. Wang, W. Zhang, and A. Dong, "Measurement and modeling of Bidirectional Reflectance Distribution Function (BRDF) on material surface," *Measurement*, vol. 46, no. 9, pp. 3654–3661, Nov. 2013.

[65] R. Yeo, R. Rykowski, D. Kreysar, and K. Chittim, "The imaging sphere - the first appearance meter?," *Proc. 5th Oxford Conf. Spectrosc.*, no. June, pp. 87–103, 2006.

[66] Zemax, "BSDF data interchange file format specification." [Online]. Available: http://customers.zemax.com/os/resources/learn/knowledgebase/bsdf-data-interchange-file-format-specification. [Accessed: 25-Jul-2018].

[67] O. Büttel, "Background Correction In AAS – Can You Really Trust It As Much As You Do ?," *Labmate-online*, 2014. [Online]. Available: https://www.chromatographytoday.com/article/mass-spectrometry-and-spectroscopy/41/oliver_bttel/background_correction_in_aas_can_you_really_trust_it_as_much_as_you_do/1610.

[68] J. A. Kirk, O. Banerji, and R. P. Fagan, "Characteristics of the Clostridium difficile cell envelope and its importance in therapeutics," *Microb. Biotechnol.*, vol. 10, no. 1, pp. 76–90, Jan. 2017.

[69] C. Nordqvist, "What is Clostridium difficile (C. difficile)?," *Medical News*

Today, Dec-2017. [Online]. Available: https://www.medicalnewstoday.com/articles/172329.php.

[70] W. J. Bradshaw, A. K. Roberts, C. C. Shone, and K. R. Acharya, "The structure of the S-layer of Clostridium difficile," *J. Cell Commun. Signal.*, vol. 12, no. 1, pp. 319–331, Mar. 2018.

[71] M. M. Merrigan, A. Venugopal, J. L. Roxas, F. Anwar, M. J. Mallozzi, B. A. P. Roxas, D. N. Gerding, V. K. Viswanathan, and G. Vedantam, "Surface-Layer Protein A (SlpA) Is a Major Contributor to Host-Cell Adherence of Clostridium difficile," *PLoS One*, vol. 8, no. 11, p. e78404, Nov. 2013.

[72] O. Yadid-Pecht and R. Etienne-Cummings, Eds., *CMOS Imagers: From phototraduction to image processing*, 1st ed. Boston: Kluwer Academic Publishers, 2004.

[73] M. Lesser, "Charge coupled device (CCD) image sensors," in *High Performance Silicon Imaging*, no. Ccd, Elsevier, 2014, pp. 78–97.

[74] M. Bigas, E. Cabruja, J. Forest, and J. Salvi, "Review of CMOS image sensors," *Microelectronics J.*, vol. 37, no. 5, pp. 433–451, May 2006.

[75] B. G. Streetman and S. K. Banerjee, *Solid State Electronic Devices*, 6th ed. Pearson Prentice Hall, 2005.

[76] A. H., M. C-K., and V. P., "CMOS Photodetectors," in *Photodiodes - World Activities in 2011*, InTech, 2011.

[77] S. Dimitrijev, *Principles of Semiconductor Devices*, 2nd ed. New York: Oxford University Press.

[78] K. Murari, R. Etienne-Cummings, N. Thakor, and G. Cauwenberghs, "Which Photodiode to Use: A Comparison of CMOS-Compatible Structures," *IEEE Sens. J.*, vol. 9, no. 7, pp. 752–760, Jul. 2009.

[79] G. Koklu, R. Etienne-Cummings, Y. Leblebici, G. De Micheli, and S. Carrara, "Characterization of standard CMOS compatible photodiodes and pixels for Lab-on-Chip devices," in *2013 IEEE International Symposium on Circuits and Systems (ISCAS2013)*, 2013, pp. 1075–1078.

[80] A. El Gamal and H. Eltoukhy, “CMOS image sensors,” *IEEE Circuits Devices Mag.*, vol. 21, no. 3, pp. 6–20, May 2005.

[81] J. Nakamura, *Image Sensors and Signal Processing for Digital Still Cameras*. Boca Raton, FL: CRC Press, Taylor & Francis Group, 2006.

[82] D. Durini and D. Arutinov, “Operational principles of silicon image sensors,” in *High Performance Silicon Imaging*, Elsevier, 2014, pp. 25–77.

[83] R. Xu, W. C. Ng, J. Yuan, S. Yin, and S. Wei, “A 1/2.5 inch VGA 400 fps CMOS Image Sensor With High Sensitivity for Machine Vision,” *IEEE J. Solid-State Circuits*, vol. 49, no. 10, pp. 2342–2351, Oct. 2014.

[84] R. Coath, J. Crooks, A. Godbeer, M. Wilson, and R. Turchetta, “Advanced Pixel Architectures for Scientific Image Sensors,” *Top. Work. Electron. Part. Phys.*, pp. 57–61, 2009.

[85] X. Zhang, M. S. Noor, C. B. McCracken, Z. H. T. Kiss, O. Yadid-Pecht, and K. Murari, “CMOS Image Sensor and System for Imaging Hemodynamic Changes in Response to Deep Brain Stimulation,” *IEEE Trans. Biomed. Circuits Syst.*, vol. 10, no. 3, pp. 632–642, Jun. 2016.

[86] Liu Chi, “A Double-mode Linear Imaging System for IC-compatible Microspectrometers in Visible Light,” Delft University of Technology, 2010.

[87] B. Razavi, *Design of Analog CMOS Integrated Circuits*. McGraw-Hill Companies, 2001.

[88] B. Choubey, W. Mughal, and L. Gouveia, “Circuits for high performance complementary metal-oxide-semiconductor (CMOS) image sensors,” in *High Performance Silicon Imaging*, Elsevier, 2014, pp. 124–164.

[89] K. Murari, R. Etienne-Cummings, N. V. Thakor, and G. Cauwenberghs, “A CMOS In-Pixel CTIA High-Sensitivity Fluorescence Imager,” *IEEE Trans. Biomed. Circuits Syst.*, vol. 5, no. 5, pp. 449–458, Oct. 2011.

[90] X. Qian, H. Yu, and S. Chen, “A Global-Shutter Centroiding Measurement CMOS Image Sensor With Star Region SNR Improvement for Star Trackers,” *IEEE Trans. Circuits Syst. Video Technol.*, vol. 26, no. 8, pp. 1555–1562, Aug. 2016.

[91] E. Pilavaki, V. Valente, and A. Demosthenous, “CMOS Image Sensor for Lateral Flow Immunoassay Readers,” *IEEE Trans. Circuits Syst. II Express Briefs*, vol. 65, no. 10, pp. 1405–1409, Oct. 2018.

[92] B. Linares-Barranco and T. Serrano-Gotarredona, “On the design and characterization of femtoampere current-mode circuits,” *IEEE J. Solid-State Circuits*, vol. 38, no. 8, pp. 1353–1363, Aug. 2003.

[93] M. M. Morris and D. M. Ciletti, *Digital desing with an introduction to the verilog HDL*, 5th ed. Pearson, Prentice Hall.

[94] A. El Gamal, “Introduction to Image Sensors and Digital Cameras - Lecture Notes,” *Stanford Engineering*. [Online]. Available: http://isl.stanford.edu/~abbas/aeglect392b.php.

[95] E. Kamrani, F. Lesage, and M. Sawan, “Low-Noise, High-Gain Transimpedance Amplifier Integrated With SiAPD for Low-Intensity Near-Infrared Light Detection,” *IEEE Sens. J.*, vol. 14, no. 1, pp. 258–269, Jan. 2014.

[96] Z. Xiao, “High-Performance CMOS Image Sensor and System for Imaging Tissue Hemodynamics,” University of Calgary, Alberta, 2014.

[97] R. R. Singh, D. Ho, A. Nilchi, G. Gulak, P. Yau, and R. Genov, “A CMOS/Thin-Film Fluorescence Contact Imaging Microsystem for DNA Analysis,” *IEEE Trans. Circuits Syst. I Regul. Pap.*, vol. 57, no. 5, pp. 1029–1038, May 2010.

[98] R. Xu, B. Liu, and J. Yuan, “A 1500 fps Highly Sensitive 256 x 256 CMOS Imaging Sensor With In-Pixel Calibration,” *IEEE J. Solid-State Circuits*, vol. 47, no. 6, pp. 1408–1418, Jun. 2012.

[99] H. Ji, D. Sander, A. Haas, and P. A. Abshire, “Contact Imaging: Simulation and Experiment,” *IEEE Trans. Circuits Syst. I Regul. Pap.*, vol. 54, no. 8, pp. 1698–1710, Aug. 2007.

[100] J. Guo and S. Sonkusale, “A 65 nm CMOS Digital Phase Imager for Time-Resolved Fluorescence Imaging,” *IEEE J. Solid-State Circuits*, vol. 47, no. 7, pp. 1731–1742, Jul. 2012.

[101] H. X. Jiang and J. Y. Lin, “Nitride micro-LEDs and beyond - a decade progress review,” *Opt. Express*, vol. 21, no. S3, p. A475, May 2013.

[102] P. Tian, J. J. D. McKendry, Z. Gong, S. Zhang, S. Watson, D. Zhu, I. M. Watson, E. Gu, A. E. Kelly, C. J. Humphreys, and M. D. Dawson, "Characteristics and applications of micro-pixelated GaN-based light emitting diodes on Si substrates," *J. Appl. Phys.*, vol. 115, no. 3, p. 33112, Jan. 2014.

[103] R. R. Harrison, "The MOS Transistor in Weak Inversion." [Online]. Available: http://www.ece.utah.edu/~harrison/ece5720/Subthreshold.pdf. [Accessed: 16-Dec-2015].

[104] C. Enz, "Low-Power Analog IC Design." Mead Education S.A., 2014.